



Trinity College Dublin
Coláiste na Tríonóide, Baile Átha Cliath
The University of Dublin

Battery Thermal Management for Batteries in Simulated Environment

Rohit Rajaram Kolekar

Supervisor: Asst. Prof. Dr. Séamus O'Shaughnessy

Department of Mechanical, Manufacturing & Biomedical
Engineering
School of Engineering
Trinity College Dublin, *the University of Dublin*
D02 PN40
Ireland

August 18, 2025

A dissertation submitted in partial fulfillment
of the requirements for the degree of
MSc in Mechanical Engineering

Declaration

I hereby declare that this dissertation is entirely my own work and that it has not been submitted as an exercise for a degree at this or any other university.

I have read and I understand the plagiarism provisions in the General Regulations of the University Calendar for the current year, found at <http://www.tcd.ie/calendar>.

I have completed the Online Tutorial on avoiding plagiarism 'Ready Steady Write', located at <http://tcd-ie.libguides.com/plagiarism/ready-steady-write>.

I consent / do not consent to the examiner retaining a copy of the thesis beyond the examining period, should they so wish (EU GDPR May 2018).

I agree that this thesis will not be publicly available, but will be available to TCD staff and students in the University's open access institutional repository on the Trinity domain only, subject to Irish Copyright Legislation and Trinity College Library conditions of use and acknowledgment. **(Please consult with your supervisor on this last item before agreeing, and delete if you do not consent)**

Signed: _____ Rohit Rajaram Kolekar _____

Date: _____ 01/01/2025 _____

Abstract

The increasing demands of electric vehicles (EVs) and renewable energy storage systems require improvements in lithium-ion battery performance, safety, and durability. This thesis experimentally and numerically compared three thermal management strategies—air cooling, indirect liquid cooling, and dielectric-fluid immersion cooling—using an LF105 LiFePO₄ prismatic cell. A MATLAB-based lumped thermal model, suitable for Model-in-the-Loop (MIL) and Hardware-in-the-Loop (HIL) applications, was developed by coupling a first-order equivalent-circuit electrical model with experimentally measured thermal parameters. Potentiometric tests provided open-circuit voltage–SOC–temperature correlations and entropic heat coefficients (EHCs) ranging from -0.29 to 0.24 mV/K, confirming strong SOC-dependent reversible heat effects. Simulations reproduced measured heat-generation profiles and showed that immersion cooling reduced peak cell temperatures and improved temperature uniformity relative to air and liquid cooling. These results highlight immersion cooling’s potential for enhanced thermal safety margins and provide a validated, real-time-capable modelling framework to support scalable EV and stationary storage design.

Lay Abstract

Electric cars and other alternative energy equipment use lithium-ion batteries that are safe, well-functioning, and long-lasting. Keeping the batteries at the right temperature is a critical factor. In this project, three cooling procedures were compared: blowing air across the battery, flowing liquid through a cooling plate, and fully immersing the battery in a proprietary non-conductive liquid. One commercial battery cell went through the lab test to determine how much heat it produces at different charge levels and temperatures. Those measurements were implemented on a computer model that can run in real time, so it is perfectly suited for hardware testing. The tests found that immersing the battery in a liquid kept it cooler and more evenly heated than the two other methods, which can prevent overheating and extend battery lifespan. The technique might be especially useful for producing safer and more resilient electric vehicles and energy storage systems.

Acknowledgements

I would like to express my gratitude to my supervisor, Assistant Professor Dr. Séamus O'Shaughnessy, for the guidance, patience, and time he has provided me. Thanks to him, I was able to pursue what I am interested in, as well as familiarize myself with CFD and battery technology with its thermal aspects. I would also like to thank Kantharuphan Annathurai for guiding me to set up the experiment perfectly, David Saltar for helping me with debugging annoying LabVIEW codes, Niall Williams and Ben Zelent for providing me their experimental data with which I could compare my results, and finally, I would like to thank Rajesh Nimmagadda and Prasad Kangude and my friends who supported me and guided me whenever I was stuck.

I would also like to thank my father, mother, and brother for their constant support despite the distance, adds warmth and shows the emotional backing that sustained the author.

Contents

Declaration	i
1 Introduction	1
2 Literature Review	4
2.1 Lithium-ion Battery	4
2.2 Battery Architecture	5
2.3 Thermal Challenges & Management Strategies	6
2.3.1 Battery Heat Generation	6
2.3.2 Thermal Runaway in Batteries	8
2.3.3 Battery Thermal Management System (BTMS)	10
2.4 Advance Testing Methodologies: MIL & HIL	12
2.4.1 Model-in-the-Loop Testing	13
2.4.2 Hardware-in-the-Loop Testing	13
2.4.3 Benefits of MIL and HIL Testing	14
2.5 Battery modelling Approaches	15
2.5.1 Classification of Battery Models	15
2.5.2 Mathematical Models	15
2.5.3 Electrical or Equivalent Circuit Models	16
2.5.4 Current Research with ECH models	20
2.5.5 Summary	20
2.6 Thermal Analysis in Battery	21
2.7 Model Parameter Estimation	23
2.7.1 Low Current OCV Test	23
2.7.2 Potentiometric Test	24
2.7.3 Calorimetric Test	24
2.7.4 Pulse-Relaxation Test	26
2.7.5 Hybrid Pulse Power Characterisation Test	27
2.8 Conclusion	29
3 Objectives	32
4 Experimental Setup	33
4.1 Experimental Rig Assembly	35
4.2 Uncertainty Analysis	36
4.2.1 Uncertainty during Temperature Measurement	36
4.2.2 Uncertainties during Voltage Measurement	39

4.2.3 Uncertainty during EHC Measurement	39
4.3 Experimental Procedure	41
5 Experimental Results & Discussion	42
5.1 Results	42
5.2 Discussion	47
6 Battery Model Setup in MATLAB	49
6.1 SOC Estimation and OCV Calculation	49
6.2 Terminal Voltage Calculation	50
6.3 Heat Generated By Battery	51
6.4 Heat Extracted by Lumped Model	51
7 Simulation Results & Discussion	53
7.1 Heat Generation Model Simulation	53
7.2 Temperature Simulation	55
8 Conclusion	56
8.1 Conclusion	56
8.2 Future Goals	57
8.3 Final remarks	58
Bibliography	67
A1 Experimental Results	69
A1.1 Complete Results	69
A2 Derivation for Terminal Voltage Equation	76
A3 Technical Drawings	77

List of Figures

1.1	Battery Cell, Module and Pack representation	3
2.1	Schematic representation of lithium-ion flow in a typical <i>LiFePO₄</i> electrochemical cell	5
2.2	Types of Electrochemical cells	6
2.3	The levels of the internal short circuit	9
2.4	Various Battery Thermal Management Systems	10
2.5	Indirect Liquid Cooling Configurations	12
2.6	Liquid Immersion Cooling Types	12
2.7	Basic Simulink Model	13
2.8	HIL simulator	14
2.9	Rint Model	17
2.10	First Order Thevenin Model	18
2.11	Second Order Thevenin Model	18
2.12	SOC-OCV Curve for NMC Battery	23
2.13	Entropic Behaviour of 42-Ah Prismatic Cell	24
2.14	Pulse Relaxation and EHC value for Sayno 18650 Cell	25
2.15	General Schematics for Calorimetric Test Setup	25
2.16	Principle Behind Calorimetric Method and EHC vs SOC	26
2.17	Pulse-Relaxation Test	26
2.18	Single Voltage Pulse Parameter Identification	27
2.19	Standard HPPC Test Cycle	28
2.20	Common HPPC Test Modifications for Estimating ECM Parameters	28
4.1	Schematic Diagram of Experimental Setup	34
4.2	Experimental Setup	36
4.3	Experimental Configuration for Potentiometric Testing	36
5.1	OCV Stabilisation for observed during experiment for 1 and 1/2 hrs of set point	43
5.2	OCV Stabilisation for observed during experiment for 1 and 1/2 hrs of set point along with dV/dt	44
5.3	Result for 50% SOC	45
5.4	EHC for 10% and 20% SOC	45
5.5	Comparison of EHC obtained with Prominent Studies	46
5.6	OCV representation in terms of SOC and Temperature	47
6.1	Logic to calculate OCV	50
6.2	Terminal Voltage Calculation	50

6.3	Power Heat Loss Calculation	51
6.4	Simple Lumped Thermal System	52
6.5	Thermal Schematics for BMS	52
7.1	Heat Generated by the Battery	54
7.2	Heat Generated by the Battery	54
7.3	Temperature Predicted by the Model	55
A1.1	Raw Experimental Plots along with dV/dt (Part 1)	69
A1.1	Raw Experimental Plots along with dV/dt (Part 2)	70
A1.1	Raw Experimental Plots along with dV/dt (Part 3)	71
A1.1	Raw Experimental Plots along with dV/dt (Final Part)	72
A1.2	Entropic Heat Coefficient Prediction with Uncertainties (Part 1)	73
A1.2	Entropic Heat Coefficient Prediction with Uncertainties (Final Part)	74
A1.3	Entropic Heat Coefficient Prediction with Uncertainties for Repeated Studies	75
A3.1	Drawing for LF105 (3.2 V 105 Ah) Prismatic LiFePO ₄ Cell	78
A3.2	Drawing for Front Cover Panel	79
A3.3	Drawing for Back Cover Panel	80
A3.4	Drawing for Side Cover Panel	81
A3.5	Drawing for Top Cover Panel	82
A3.6	Drawing for Bottom Cover Panel	83
A3.7	Drawing for Seal to be applied	84

List of Tables

2.1	Electrochemical reactions for <i>LiFePO₄</i> Electro chemical cell	5
2.2	Comparison of Electrochemical, Mathematical, and Equivalent Circuit Models.	19
2.3	Comparison of Equivalent Circuit Models.	19
2.4	Heat Flow Equations	22
2.5	Comparison of different testing methods for ECM parameter estimation.	29
4.1	Technical Parameters for LF105 (3.2 V 105 Ah) Battery by Manufacturer	33
4.2	Properties for Promosolv DR3	34
4.3	Standard Error of Estimate for Thermocouple	37
4.4	Overall Temperature Uncertainties	38
4.5	Weighted Sums for SOC at 50%	39
4.6	Residual Variance	40
5.1	Entropic Heat Coefficient with respective SOC range and Uncertainties.	45
5.2	Entropic Heat Coefficient with respective SOC range and Uncertainties for repeated test.	46
6.1	Model Settings used for Simulation	49

Nomenclature

Acronyms

<i>ARC</i>	Accelerating Rate Calorimeter	
<i>CFD</i>	Computational Fluid Dynamics	
<i>CPM</i>	Conventional Potentiometric Method	
<i>DRT</i>	Distribution of Relaxation Times	
<i>ECM</i>	Equivalent Circuit Model	
<i>EHC</i>	Entropic Heat Coefficient	
<i>ESC</i>	External Short Circuit	
<i>EVs</i>	Electric Vehicles	
<i>HIL</i>	Hardware-in-the-Loop	
<i>ISC</i>	Internal Short Circuit	
<i>LIB</i>	Lithium-ion Battery	
<i>MIL</i>	Model-in-the-Loop	
<i>NMC</i>	Nickel Manganese Cobalt	
<i>OCV</i>	Open Circuit Voltage	V
<i>PA</i>	Positive Adjustment	
<i>PDE</i>	Partial Differential Equations	
<i>RTD</i>	Resistance Temperature Detector	
<i>SOC</i>	State of Charge	%
<i>SOH</i>	State of Health	%

Roman Letters

\dot{Q}	Heat Generation Rate	W/s
$\frac{\partial V_{ocv}}{\partial T}$	Entropic Heat Coefficient	V/K
A, B	Empirical Constants	V, 1/Ah
C_h	Battery Capacity	Ah

NOMENCLATURE

C_p	Specific Heat Capacity	J/kgK
I	Current	A
K	Polarizing Resistance Coefficient	Ω
m	mass	kg
Q	Heat generated/extracted	W
R_0	Internal Resistance of Battery	Ω
T	Temperature	K
t	Time	s
T_∞	Ambient Temp	K
Ts	Time Step	s
V	Terminal Voltage	V
V_{OCV}	Open Circuit Voltage	V

Chapter 1

Introduction

Transition of combustion to electric drive in transportation is a function mainly of performance of an electric vehicle: basically its battery capacity, charging time, and life-time. Probably the most critical determinant for its adoption is the range an EV can continuously drive - a direct function of the capacity but also driving behaviour, weight of the vehicle, and average speed. But consumers have long been uncertain about how far a battery would run - what keeps them from widely accepting EVs.

Another significant barrier involves charging time, which significantly varies among the models of EVs, just from a few minutes up to several hours. One of the promising strategies concerning the effort for the reduction of charging times refers to the adoption of higher voltage levels in charging systems - a matter of improved efficiency and reduced duration of charging itself [1]. In turn, this sets extra loads on electrical grid infrastructure when this happens at a peak usage time: between 4 and 9 PM, or at the time when the commuters go home. The possibility of reducing such stress may also be given by smart charging technologies, such as the management of unidirectional power flow to shift the load to off-peak times, and bidirectional power flow, enabling the battery of an EV to discharge the stored energy back into the grid, hence making it distributed energy storage systems [2].

Beyond Charging and Range Issues: Another critical challenge of EVs is thermal management. LIBs, the preferred power source for EVs due to their high energy density and long life cycle, have a narrow temperature operating range of 20–40°C [3]. For this reason, any deviation from this narrow range can lead to performance deterioration, shortened lifespan, or even catastrophic results in the form of thermal runaway. Thermal runaway is a situation where high temperatures trigger exothermic reactions within the cell that cannot be controlled; this leads to uncontrollable heat generation, which may even lead to an electrical fire or explosion [4]. It would, in particular, be mandatory that sophisticated cooling systems and thermal management strategies guarantee safety, performance, and life for EV batteries.

Besides these, increasingly complicated automotive systems require development and testing methodologies that address the challenge. It is here that Model-in-the-Loop and Hardware-in-the-Loop testing have proved indispensable. These methods offer avenues for the engineers to design, validate, and optimize complex automotive systems with safety, reliability, and cost efficiency in view.

INTRODUCTION

MIL testing allows validation of control algorithms at an early stage in a virtual environment and therefore catches design flaws much earlier than in hardware implementations. This significantly reduces the number of development cycles and, consequently, the costs involved with iteration. For instance, control algorithms for gantry cranes and automotive architectures have been designed using MATLAB and Simulink to realize the efficacy of MIL testing in differentiating and simulating system behaviours under various conditions [5].

It also closes the gap between MIL and real-world validation. In a Hardware-in-the-loop, hardware components like sensors, actuators, and electronic control units are integrated into a closed-loop simulation of real-time testing under realistic operating conditions. This has been very helpful in automotive applications because it reduces risks in testing critical systems under extreme scenarios [6]. Some examples include dSPACE, National Instruments, and MATLAB Simulink Real-Time. These flexible platforms are designed to conduct the most accurate and effective HIL simulations necessary for cutting debugging costs and minimizing further risks to physical prototypes.

This synergy further increases with the help of MBD, as it incorporates modelling, simulation, and automatic code generation under a single platform. MBD was very crucial in developing many new advanced automotive systems, like energy management and other safety-critical applications. Use of MIL and HIL on AUTOSAR frameworks helps for seamlessly integrating hardware and software, reducing the development cycle and the developed products are qualitative too [7].

The HIL methodologies also redefine the traditional testing paradigms through the integration of advanced control strategies and multi-body dynamics in order to come up with more realistic simulation models, which, in turn, further improve system response and reduce errors in simulation, thus enabling modular and flexible testing platforms for EVs [8].

In the future, efficiency, reliability, and scalability of MIL and HIL test methodologies will be highly important during the development phase in the automotive industry. They will be one of the key sets of tools in dealing with the challenges brought about by electrification and autonomous systems, enabling the industry to meet the rising demands of modern automotive architecture while continuing its move toward a more sustainable future.

Before moving to the literature review, it is important to understand basic battery concepts and terminologies as it will be easy to follow along with the report. Basic battery definitions are as follows:

- **Cells, modules and packs:** Hybrid and electric vehicles use high-voltage battery packs made up of modules, each containing a number of cells that are connected in series or parallel. A cell is the smallest unit of a battery and typically ranges from 1–6 volts. Modules combine these cells, and battery packs are created by linking multiple modules in series or parallel configurations [9].

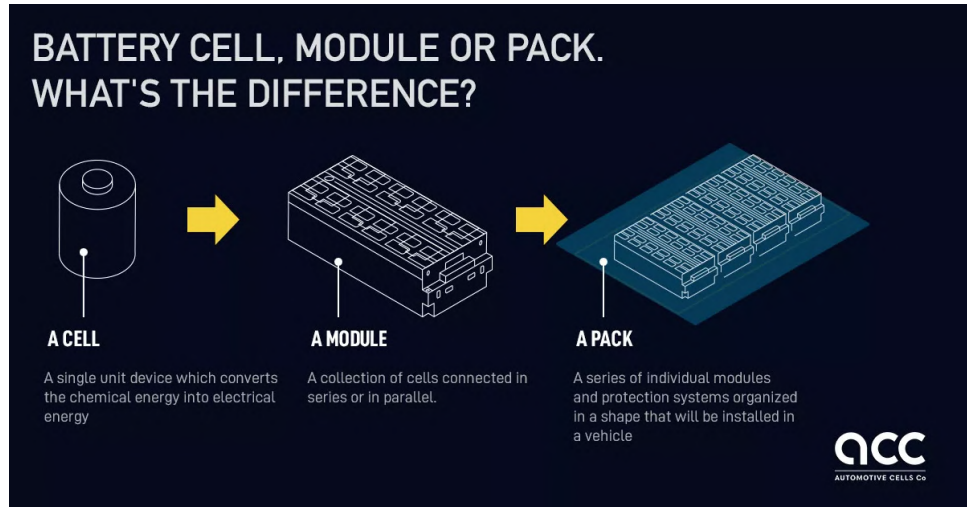


Figure 1.1: Battery Cell, Module and Pack representation [10]

- **C and E rates:** The C-rate defines the amount of time it will take for the battery to discharge, with its capacity taken into consideration. This rating thus provides an easy, standardized method to compare batteries. For example:
 - 1C: The battery will be fully discharged in 1 hour. In the case of a 100 Amp-hour battery, this would correspond to a discharge current of 100 Amps.
 - 5C means in 1/5th hour the battery for same one is discharging 500 Amps.
 - C/2 means it discharges in 2 hours. (50 Amps).
 One other way of defining discharge power is referred to as E rate. A 1E rate would be the power required to completely discharge the battery in 1 hour.
- **State of Charge, SOC (%) :** It is the percentage of the current battery level about its maximum capacity. This is obtained by observing the intake of charge that has entered or left the battery over some period.
- **Depth of Discharge, DOD (%) :** The percentage of used-up battery capacity with respect to its maximum. If 80% or more of the capacity has been used up, then a deep discharge is said to have occurred.
- **The Terminal Voltage (V):** The voltage measured at the battery terminals while it is in use. It changes based on the charge level (SOC) and the current being drawn or supplied.
- **Open circuit Voltage (V):** The voltage at the battery terminals when no device is connected. It increases as the battery's charge level rises.

Chapter 2

Literature Review

The demands for battery-powered applications have been calling for effective battery modelling, which this chapter presents an overview of with important efforts in that direction. In particular, this chapter highlights high-precision battery models in terms of performance evaluation, optimization of energy storage systems, and design strategies for effective battery management. Many different modelling approaches are discussed related to their applications in new emerging technology developments: electric vehicles and renewable energy systems. The chapter will further elaborate on the techniques of parameter identification and their role in simplifying such complex modelling processes. This review summarizes key advances and challenges in battery modelling and provides a proper overview of state-of-the-art developments and future directions in this important area of research.

2.1 Lithium-ion Battery

A general Li-ion battery comprises electrolyte, metal oxide anode, separator, and lithium cathode [11]. During discharge, the positively charged lithium ions move across the separator from cathode to anode using the electrolyte as their carrier. The flow of lithium ions results in free electrons at the anode, which further produces a charge at the positive current collector [11]. The current flows to the device connected before completing the circuit back to the negative current collector. The separator prevents electrons from leaving the battery [12] [13].

Fig. 2.1 shows the schematic representation of a normal 18650 *LiFePO₄* electrochemical cell. In the discharge cycle of LFP batteries, lithium molecules in the layered graphene at the negative electrode break loose into lithium ions and electrons. While electrons leave the battery, lithium ions, after crossing the separator to reach the positive electrode, combine with electrons that are already there and turn into iron phosphates. In the case of charging, lithium is pulled out of the iron phosphate to form lithium ions and electrons. During this process of movement of the lithium ions and electrons to the positive electrode, they intercalate into the graphene structure. This reaction proceeds from the right to the left. The respective electrochemical reactions are presented below table 2.1 [15].

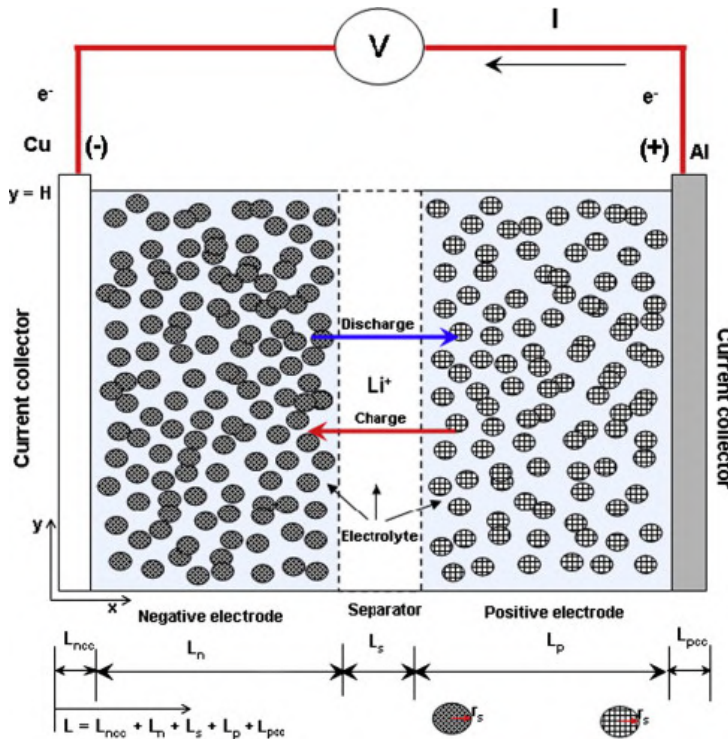


Figure 2.1: Schematic representation of lithium-ion flow in a typical $LiFePO_4$ electrochemical cell [14]

Electrode	Electrochemical Reactions
Anode	$Li_x C_6 \rightleftharpoons Li_{x-z} C_6 + zLi^+ + ze^-$
Cathode	$Li_{y-z} FePO_4 + zLi^+ + ze^- \rightleftharpoons Li_y FePO_4$
Overall	$Li_x C_6 + Li_{y-z} FePO_4 \rightleftharpoons Li_{x-z} C_6 + Li_y FePO_4$

Table 2.1: Electrochemical reactions for $LiFePO_4$ Electro chemical cell [15] [16].

In table 2.1, x refers to the number of moles in the graphite of the negative electrode, y refers to the amount of lithium in the iron phosphate of the positive electrode, and z represents the amount of lithium involved in the battery's electrochemical reaction [16].

2.2 Battery Architecture

There are three main forms of lithium-ion battery cells used in EVs. These are as follows,

- Cylindrical Battery Cells (fig. 2.2a)
- Prismatic Battery Cells (fig. 2.2b)
- Pouch-type Battery Cells (fig. 2.2c)

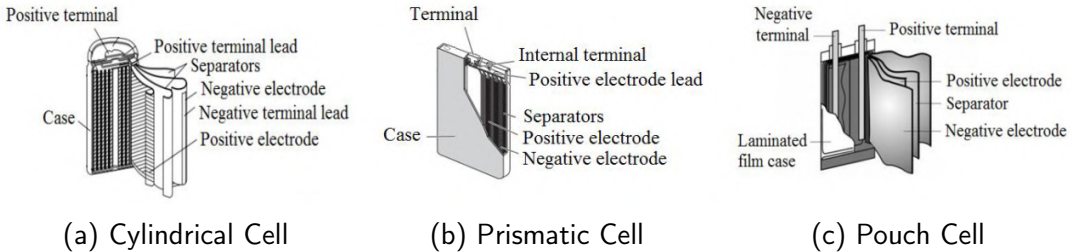


Figure 2.2: Types of Electrochemical cells [13]

For cylindrical cells, the positive and negative current collectors are at one or the other terminal of the cell, and these current collectors are subsequently connected to terminals [17]. This cylindrical shape includes thin layers of cathode and anode material that are immersed in an electrolyte and wound around a central mandrel [17] [18]. Comparing three types of cells, cylindrical cells have the highest cost of production. They also generally have a higher weight per energy storage compared with their prismatic or pouch cell counterparts [19].

The prismatic cell format is related, on the other hand, to the electrode sheets being wound within a rectangular arrangement and pressed into a hard case. In such a setting, the current collectors are at one terminal of the cell and, in particular, allow good electrical and mechanical contact. The pouch cell has a similar rectangular geometry concerning the prismatic cell but is differently configured [13]. Instead of winding, the pouch cell merely stacks the electrodes. This further simplifies production, but most importantly, very high packing density enables this type of battery to be of particular use in applications where space and weight restrictions are important, such as automotive applications [20].

2.3 Thermal Challenges & Management Strategies

2.3.1 Battery Heat Generation

Second Law of Thermodynamics states that there will be residual heat when the work is done [21]. Thus, the battery, during its use, will also produce heat. Primary sources of heat are discussed below.

2.3.1.1 Joule Heating

Joule heating or irreversible heating, also known as ohmic heating, is heat generated when the current flows through the battery, which is due to the resistivity of the electrodes, electrolyte, and current collectors [22]. It is a primary source of heat generation in the battery during its operation (charge or discharge) and is proportional to the square of the current and can be visualised in the equation 2.1 [23].

$$Q_{ohmic} = RI^2 \quad (2.1)$$

Where, I is the current, R_0 is the internal resistance of the battery, t is time. But the total irreversible heat generation is not just due to ohmic loss but also comprises its overpotential, which is defined as the difference between the operating voltage and open circuit voltage of the battery [23]. The Joule heating equation is expressed as follows;

$$Q_{joule} = I \cdot (V - V_{OCV}) \quad (2.2)$$

Where, V is the operating voltage, and V_{OCV} is the open-circuit voltage of the battery. This heat can be exothermic (releasing heat) or endothermic (absorbing heat) making it reversible, whose magnitude depends on the battery's chemistry and SOC of the battery [22]. This heat affects even during low currents as well, which influences the design of the thermal management system.

2.3.1.2 Entropic Heat Generation

Entropic heat generation, also known as reversible heat, occurs due to entropic changes associated with the electrochemical reactions due to the motion of ions within electrodes during charge and discharge [24] [25].

$$Q_{rev} = I \cdot T \cdot \frac{\partial V_{OCV}}{\partial T} \quad (2.3)$$

Where, T is the temperature of the battery and $\partial V_{OCV}/\partial T$ is the entropic heat coefficient of the battery, which can simply be referred to as the change in OCV w.r.t. temperature. Q_{rev} can be exothermic or endothermic depending on the SOC of the battery, making it reversible [26].

2.3.1.3 Heat Generation or Absorption from Side Reactions

Heat generated or absorbed due to the chemical reactions during battery operation, which specifically are related to the ageing of the cell [22] [26] [27]. These reactions are the composition of solid electrolyte interphase layers, lithium plating, electrolyte degradation, etc., which are at the chemical level [28].

$$Q_{sr} = \sum_i \Delta H_i^{\text{avg}} r_i \quad (2.4)$$

Where, ΔH_i denotes the enthalpy change associated with the i^{th} chemical reaction, occurring at a reaction rate r_i .

2.3.1.4 Enthalpy of Mixing Heat

Enthalpy of mixing heat arises from the relaxation of ionic concentration gradients within the cell during the mixing process [26]. In simple terms, the heat generated after the removal of the current is the heat of mixing [27]. This form of heat generation becomes particularly significant during dynamic charge/discharge conditions [22]. These ionic gradients, which can be described as follows [26];

- across the electrolyte due to mass transfer
- across the electrode due to non-uniform current distribution
- due to electrochemical reactions at electrodes due to lithium vacancies
- due to electrochemical reactions causing lithium ions to intercalate into the electrode

The equation for the mix heating is expressed as follows [22] [26]

$$Q_{mix} = \int \sum_j (\bar{H}_j - \bar{H}_j^{avg}) \frac{\partial c_j}{\partial t} dv \quad (2.5)$$

Where, \bar{H}_j is the partial molar enthalpy, c_j is the ion concentration of/in j^{th} piece of the battery at volume v .

With all these equations which are primarily based on work done by Bernardi *et al.* [29] and Thomas *et al.* [27], the complete heat generation rate can be written as:

$$\dot{Q}_{batt} = Q_{joule} + Q_{rev} + Q_{sr} + Q_{mix}$$

Which makes the final equation as:

$$\dot{Q}_{batt} = I(V - V_{OCV}) + IT \frac{\partial V_{OCV}}{\partial T} - \sum_i \Delta H_i^{avg} r_i - \int \sum_j (\bar{H}_j - \bar{H}_j^{avg}) \frac{\partial c_j}{\partial t} dv \quad (2.6)$$

The heat generated from Q_{sr} is closely associated with the battery ageing, while Q_{mix} becomes significant primarily in poorly manufactured batteries that exhibit high concentration overpotentials, as noted by Thomas *et al.* [27]. Therefore, both can be reasonably neglected in simplified computational or numerical models, assuming the battery is new and of good manufacturing quality. This allows the equation 2.6 to be reduced to:

$$\dot{Q}_{batt} = I(V - V_{OCV}) + IT \frac{\partial V_{OCV}}{\partial T} \quad (2.7)$$

2.3.2 Thermal Runaway in Batteries

As discussed in Section 2.3.1, heat generation in Li-ion batteries is a critical factor influencing their safety and performance. Thermal runaway is such a severe failure of a battery that it refers to an uncontrollable exothermic chain reaction producing tremendous heat and generally leads to smoke generation, electrical fires, and explosions [30]. The thermal runaway will happen when the temperature of the battery goes over its working level of 20°C to 40°C, where it generates a chain reaction exothermically, releases a huge amount of energy within a very short period of time, and an enormous temperature rise as high as about 400°C may take place inside the battery cell [31]. Generally speaking, the causative agents of thermal runaway in LIBs can be any abuses, including but not limited to mechanical, electrical, or thermal abuse [31].

2.3.2.1 Mechanical Abuse

This abuse indicates that due to forces and impacts, the exposure results in the battery deforming with the possibility of penetration and leading to a safety hazard. Looking into the LIB cells within the EV battery pack, their possible exposure to mechanical abuses due to a vehicle collision would be quite high. A tear in the cell might have caused a separator penetration and, hence, ISC, thus initiating the thermal runaway reaction. What this means

in terms of casing design is that such cell failures have to be prevented if battery packs in an electric vehicle are to be protected from very high mechanical loading [32].

2.3.2.2 Thermal Abuse

The temperatures can be a result of the self-heating of a battery in either a discharging or charging mode, and can also be subjected to heating externally because of conduction, convection, and radiation. It has to be noted then that temperature rises on a battery could arise from this. That would also mean the systems for cooling and temperature detection are not functional while the battery is in storage or in non-operating modes. Hence, LIBs are stored and transported under conditions with appropriate safety considerations [33].

2.3.2.3 Electrical Abuse

Overcharge forces the battery to charge to a voltage greater than what the manufacturing company recommends. It forces the cathode to lose its ions, and it is made chemically unstable to an extent that it can react with the electrolyte. The build-up of the depression of ions on the anode results in metallic lithium formation that can also react with the electrolyte. Metallic lithium build-up could also result in dendrite formation that may pierce the separator and cause an internal short circuit [33].

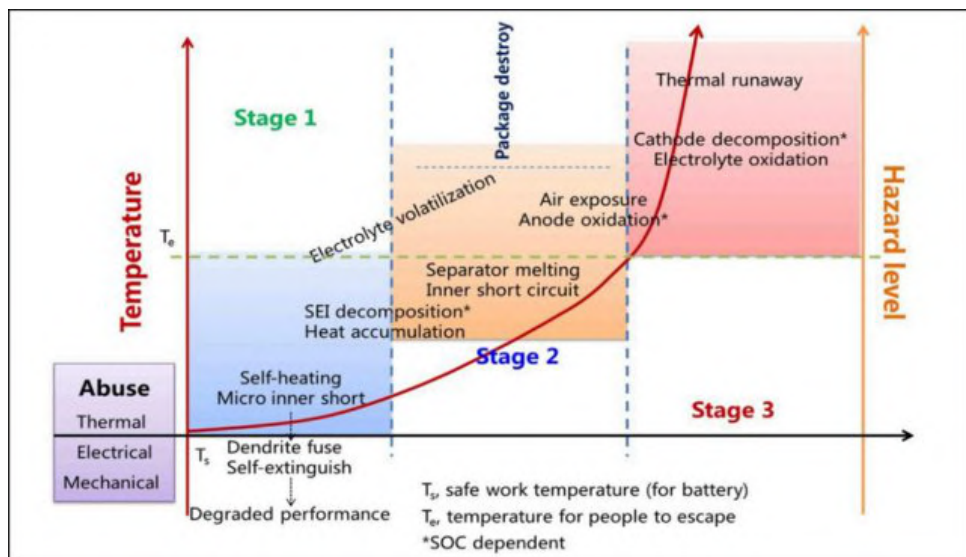


Figure 2.3: The levels of the internal short circuit [34]

Internal short circuiting (ISC) is a phenomenon wherein the anode and cathode of the battery come in contact with each other due to failure of the separator between them. Generally speaking, ISC can be triggered by a lot of factors: because of mechanical abuses, such as by crushing; electrical abuses, such as by the piercing of the separator by dendrites or by thermal abuse, for instance. Basically, when there is excessive shrinkage at high temperatures, there is also a type of ISC called self-induced ISC, which emanates from defects in the battery manufacturing process. It has been observed that this type of ISC can take days or even months to develop until it manifests as a spontaneous ISC, which results in thermal runaway. Current literature has proposed that there exist three phases of ISC as depicted in Fig. 2.3. First, the battery exhibits self-extinguish behaviour with a low level of self-discharge, but very slight heat generation. In the second, the self-discharge rate increases further, with a

noticeable rise in the rate of heat generation. The final stage gives rise to uncontrollable intensive heat generation because thermal runaway occurs. However, this process takes a very long time, and thus all these signs and marks can be observed and necessary action could be taken to prevent thermal runaway in the system [32].

The external short circuit (ESC) is caused due to the low impedance connection between the cathode and anode of the battery. There would have been many reasons for generating the electrical path between the anode and cathode, such as installation error or being immersed in a substance that allows an electric path to flow, such as water [33].

2.3.3 Battery Thermal Management System (BTMS)

Operating temperature is one of the most critical factors that influence lifespan, performance, and safety; thus, a BTMS is rather important. In fact, BTMS minimizes internal heat generation and rise in temperature that could have adverse effects on battery performance [35]. Higher temperatures increase the rates of chemical reactions and degradation mechanisms, while lower temperatures result in reduced capacity and energy density [36]. These are very serious in large-format lithium-ion batteries for EVs [37]. Thus, BTMS needs to be comprehensively understood to realize high performance and safety.

Its major task is maintaining the batteries within the desired operating temperature, which is between 20°C and 40°C with good temperature uniformity less than 5°C temperature difference across the pack. BTMS may be divided into active and passive systems. Active systems: These are the systems that use power from some other source. The main applications of active systems involve liquid and air cooling systems and hence they make use of pumps and fans respectively. The active systems can be further divided into liquid cooling systems, immersion cooling, and indirect liquid cooling systems [36]. Passive systems: These are those systems that make use of phase change materials to enhance thermal uniformity or deploy heat pumps of high thermal conductivity for dissipating heat [36]. Such examples can be seen in fig. 2.4.

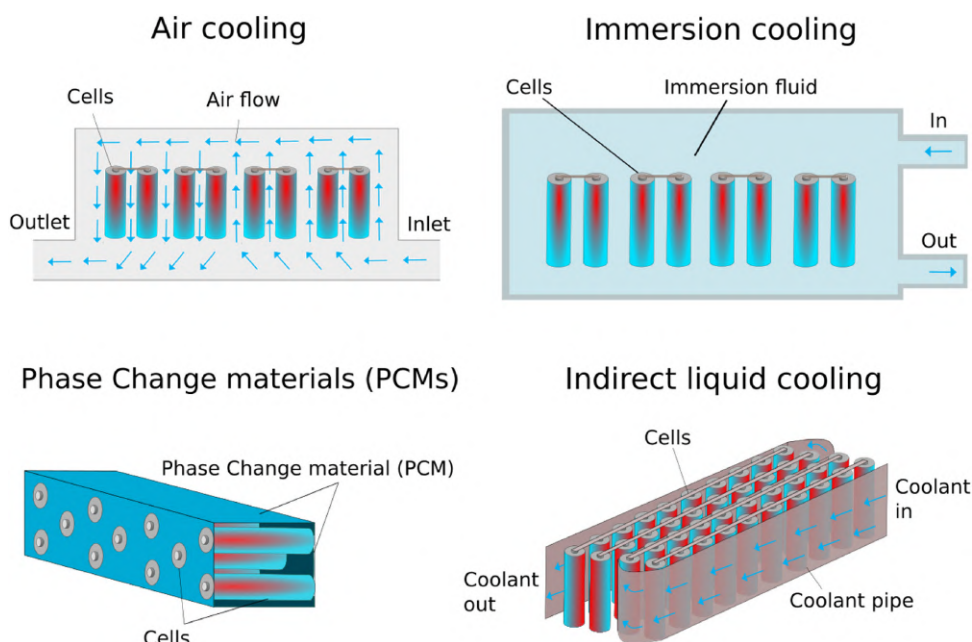


Figure 2.4: Various Battery Thermal Management Systems [38]

2.3.3.1 Air Cooling Method

There are two different air heat-dissipation modes for the air-cooled battery thermal management systems of electric vehicles: active and passive convection mechanisms. As compared to the other BTMS techniques, an air-cooled technique is comparatively safe, low in cost, and simple. Applications of natural convection are greatly limited since the utilization of natural convection mainly depends on good ambient environment conditions and it does not tolerate high-temperature operating conditions [39].

Limitations in the matter of enhancement goals of forced or mixed convection, on the other hand, allow for the application of forced convection. The implementation techniques in this approach include: fans [40], fin heat sinks [41], and modified airways [42]. Contrasted with feeble warm limits with low warmth conductivity, air cooling has been utilized in a couple of business EVs [43].

2.3.3.2 Liquid Cooling Method

Liquid cooling is quite an effective BTMS, compared to air cooling, as the liquid possesses a huge specific heat capacity and high thermal conductivity, due to which it can perform indirect or direct immersion cooling. Indirect cooling systems consist of coolant that needs to be pumped along pipe channels or cooling plates carrying heat away from the battery pack. The cooling channel may be either at the side or at the bottom of the battery cells. Immersion cooling involves the coolant in direct contact with the battery cells by using a non-conductive fluid called dielectric fluid.

2.3.3.2.1 Indirect Liquid Cooling Method

Liquid-cooling methods of indirect cooling are easier to realize with much lower power consumption in contrast to direct cooling. However, the heat transfer performance is comparably bad, given that channel materials are used in them. In respect to indirect cooling methods, the main ones are a cold plate and a heat pipe [44].

The cold plates may also be flat metal designs with internal channels for the HTF circulation and are usually located inside the battery monomer between adjacent cells, or on the sides of modules [39]. These kinds of channels may be parallel; for example, the studies of Rau *et al.* [45] or serpentine patterns, studied by Sheng *et al.* [46].

Heat pipes, another indirect cooling technique, use pressure gradients and capillarity to propel fluid motion passively [47]. They consist of a vacuum-sealed tube with a wick system and functional fluid, including an evaporator, an adiabatic section, and a condenser [48]. One of the disadvantages of this cooling method is that it involves an elaborate network of pipes with greater chances of failures aside from the fact that thermal resistances due to the existing tubes between coolant and battery cell exist. themselves.

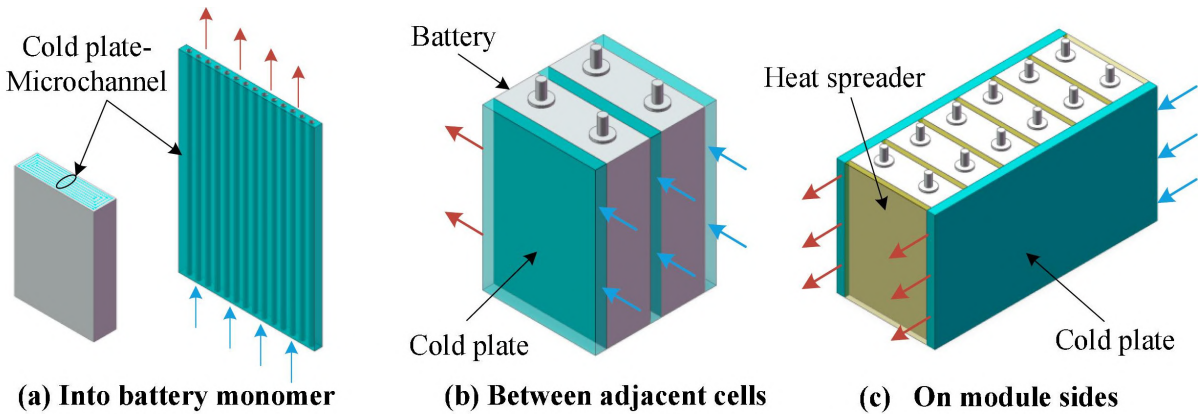


Figure 2.5: Indirect Liquid Cooling Configurations [39]

2.3.3.2.2 Liquid Immersion Cooling Method

Liquid immersion cooling, or direct liquid cooling, involves the full immersion of the battery in a dielectric fluid without electrical conduction, at actual contact with the cell. It happens to be one promising technology that has hence gained huge interest within portable electronics and electric vehicle industries. The methods of immersion cooling vary according to the degree of submerging, type of flow, and regime of fluid operation. Immersion cooling typically involves single and two-phase immersion systems. In single-phase immersion, the dielectric fluid is continuously in a single state, while in two-phase it alters from liquid to a phase of vapor [38].

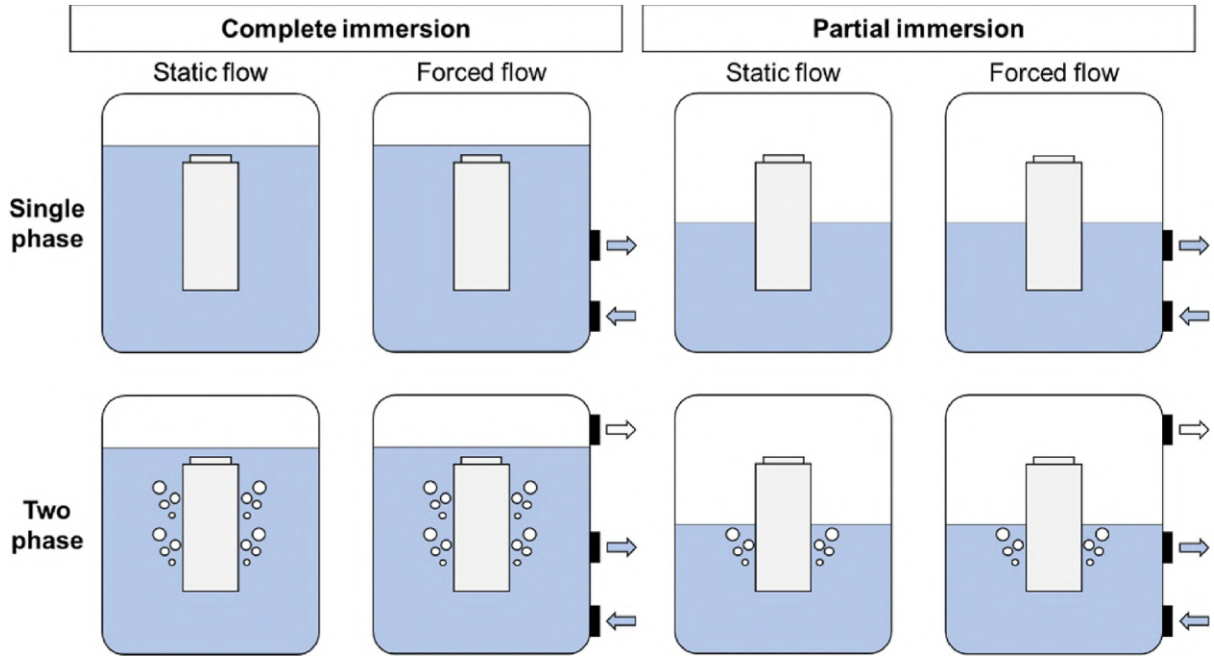


Figure 2.6: Liquid Immersion Cooling Types [38]

2.4 Advance Testing Methodologies: MIL & HIL

Integration of Model-in-the-Loop (MIL) and Hardware-in-the-Loop (HIL) testing turned the creation of modern vehicles into a much quicker, more cost-effective, and reliable process of

development. Such methods solve part of the most critical challenges during the validation process of such complicated automotive systems using iterative testing, which guarantees seamless hardware-software integration. These methods allow users to execute real-time simulation in an environment where physical experimentation has limits.

2.4.1 Model-in-the-Loop Testing

Model-in-the-Loop (MIL) testing methodology involves the validation of control algorithms within a virtual environment, well before the introduction of hardware into a system. Testing at this level involves how well the model or control logic performs under different conditions within a virtual or simulated setup [5]. Developers then create simulations with systems' behaviour in tools such as MATLAB Simulink and verify that the algorithms are working as expected before iterative improvements; they do this without any kind of hardware [5].

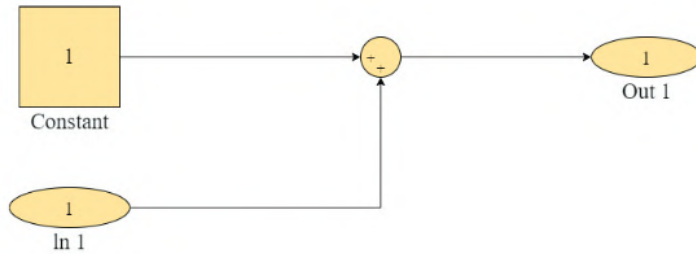


Figure 2.7: Basic Simulink Model [5]

When designing control algorithms or creating a simple simulation environment for physical components, MIL testing plays a great role by virtual simulation of system behaviour. This removes the necessity to have any physical hardware during the initial design and hence helps developers perfect their control logic in isolation. In this regard, they have been able to demonstrate, for instance, the iterative refinement of gantry crane system control algorithms in order to determine functionality prior to hardware integration [5].

In Automotive applications, MIL permits the testing of subsystems, for example, high voltage electrical systems, braking systems, electronic control units, etc. Early prototyping of control logic allows the developer to find and correct mistakes before costly investments in hardware are made [7].

2.4.2 Hardware-in-the-Loop Testing

Hardware-in-the-Loop (HIL) testing integrates real hardware into a simulation loop to take the development process one step further than MIL. HIL provides a closed-loop testing environment where physical components such as sensors, actuators, and control units are interfaced with a virtual simulation of the system [6]. The simulation provides the inputs to the hardware, while the hardware outputs are fed back into the simulation to validate the real-world performance of the components under various operating conditions [8].

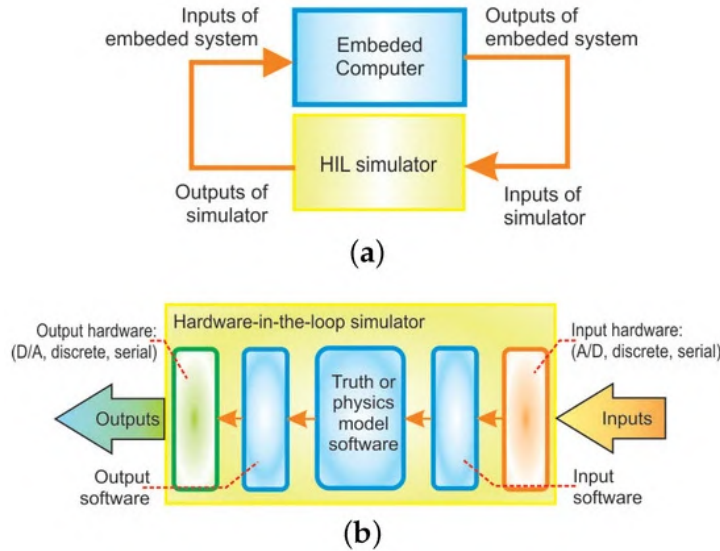


Figure 2.8: HIL simulator: (a) Block diagram of embedded system connected to a HIL simulator; (b) components of a simple HIL simulator [6]

Fig. 2.8 illustrates the general block scheme of an embedded system where a HIL-simulator is applied for testing and the components which at least a simple HIL-simulator must comprise. Thus, HIL testing fills the gap between virtual simulation and real-world implementation by introducing physical hardware into the testing environment [8]. HIL testing provides a controlled environment for the testing of hardware components, such as ECUs, under realistic conditions. Their research emphasizes its application in the validation of EV power-train and energy systems optimization [8].

Also, similar is the HIL in testing safety-critical systems, say, regenerative braking algorithms. HIL conducts tests on hazardous conditions, for instance, abrupt braking or steep decline without actually causing any kind of risk either to equipment or any loss of life [8].

2.4.3 Benefits of MIL and HIL Testing

2.4.3.1 Benefits of MIL Testing

MIL is utilized for the gantry crane system to test the control logic. In simulation, isolation of the control systems is done; hence, it allows developers to find the design flaws and refine their algorithms without using physical prototypes [5]. For automotive, MIL will have developers test subsystems with virtual models, such as high voltage battery systems, electronic control units, braking systems, and power management. The use of this approach takes out expensive hardware from early testing phases as in [7].

2.4.3.2 Benefits of HIL Testing

HIL testing is invaluable for validating hardware components such as ECUs and sensors in real-time scenarios. For example, HIL was used to evaluate the performance of electric vehicle (EV) power-train and energy management systems, ensuring their robustness under various dynamic conditions [8]. HIL also enables the simulation of extreme and hazardous driving conditions, such as emergency braking or icy roads, without endangering lives or physical

equipment. This is particularly beneficial for testing safety-critical systems like regenerative braking in hybrid vehicles [8].

Mudhivarthy *et al.* highlighted that HIL reduces the reliance on fully assembled prototypes by allowing modular testing of individual components. This approach streamlines development workflows, shortens validation times, and lowers overall costs [7].

2.5 Battery modelling Approaches

Growth in electric vehicles requires a quick model of an appropriate and efficient battery that will guarantee maximum performance, life, and safety for the Battery Management System (BMS) which is controlled by the Battery Pack Control Module (BPCM). A model of the battery, therefore, is its representation in the mathematical models under the various conditions it operates. These mathematical models facilitate the designing and optimization of energy systems. The accurate models allow engineers and researchers to assess performance, make degradation analysis, and simulate system responses of transient and steady-state conditions [49].

2.5.1 Classification of Battery Models

In general, these models of batteries have been divided into categories such as an electrochemical model, mathematical model, and electrical model [49]. Each model has to balance the need for accuracy, complexity, and computation that is needed for an application.

2.5.1.1 Electrochemical Model

Electrochemical models provide highly accurate representations by simulating internal chemical reactions, ion diffusion, and thermal effects within the battery. These models are based on partial differential equations (PDEs) that describe spatial and temporal dynamics, such as those developed by Newman's porous electrode theory [49].

This model can analyze thermodynamics and kinetics of a very detailed battery. Thus, makes it ideal for the understanding of degradation mechanisms and designing new chemistries. But a high computational cost has to be borne because of the numerical solution of complex PDEs, and high dependency on the relevant accurate knowledge of the battery chemistry and geometry is required to successfully implement this model. Computation Fluid Dynamics (CFD) Analysis falls under this category as well.

For example, reduced-order electrochemical models reduce computational cost by simplifying the PDEs and attaining the necessary accuracy. The Galerkin projection method was applied on the lithium-ion batteries while RMSE errors for LFP and NMC cells were reported to be 15.5 mV [49].

2.5.2 Mathematical Models

These models are simplifications of how a battery would behave either through an empirical or stochastic approach. These models do provide a framework for understanding battery behaviour, but they often rely on parameters that need to be calibrated and validated using experimental data [50].

2.5.2.1 Empirical Models

The most well-known empirical approaches are those using the Shepherd model describing voltage behaviour under constant-current discharge by the following equation [49]:

$$V = V_{OCV} - K \left(\frac{C_h}{C_h - It} \right) I - R_0 \cdot I + A \cdot e^{-B \cdot It} \quad (2.8)$$

And constant-current charge by the following equation [49]:

$$V = V_{OCV} - K \left(\frac{C_h}{It - 0.1 \cdot C_h} \right) I - K \left(\frac{C_h}{C_h - It} \right) It - R_0 \cdot I + A \cdot e^{-B \cdot It} \quad (2.9)$$

where $It = \int I dt$, which is the extracted or added charge (Ah).

The major advantage of the Shepherd model is that it requires a small quantity of experimental data, principally extracted from the discharge curves which can be easily retrieved on manufacturers' data sheets. More recently, polarization voltage and time-variant current were integrated too in recent enhancements [49].

2.5.2.2 Stochastic Models

In contrast, the stochastic models use the probability for predicting the battery behaviour. The Kalman-filter-based methods are tracking real-time state transitions; therefore, they are suitable for dynamic SOC estimation in applications [49].

2.5.3 Electrical or Equivalent Circuit Models

The electrical components, such as resistors, capacitors, and voltage sources, model the dynamics of a battery in the ECMS. These models realize a very good trade-off between accuracy and computational efficiency and hence, are very suitable for real-time applications like HIL simulations [6].

2.5.3.1 Internal Resistance (Rint) Model

The simplest of the ECMS is the Rint model with a voltage source and only one resistor. Terminal voltage is calculated using SOC, current, and internal resistance [51].

$$V(t) = V_{OCV}(SOC(t)) - I(t) \cdot R_0 \quad (2.10)$$

If we assume that the +ve value of I indicates discharge, then the function of SOC over time will be,

$$\frac{d(SOC)}{dt} = -\frac{I}{C_h} \quad (2.11)$$

Thus,

$$SOC(t) = SOC(t_0) - \frac{1}{C_h} \int_{t_0}^t I(T) dT \quad (2.12)$$

It gives computational efficiency whereas its parameters are fixed, and also transient effects are independent. This model is highly dependent on the relation between SOC and OCV.

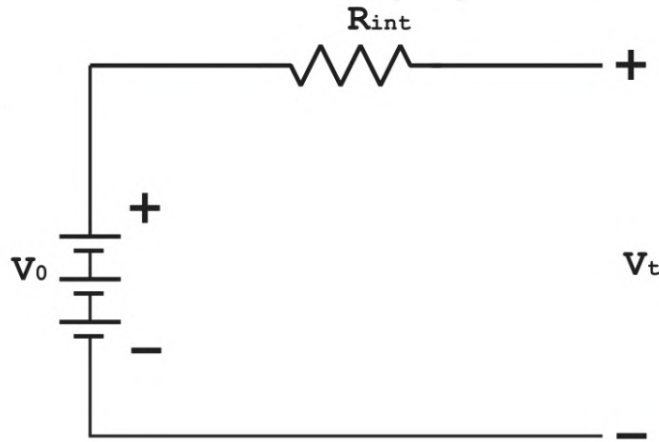


Figure 2.9: Rint Model [51]

2.5.3.2 Thevenin Model

RC network added to R_{int} is modelling transient polarization effects by adding another resistance (denoted as R_1) and capacitance (denoted as C_1) in parallel to the newly added resistance [51]:

$$V(t) = V_{OCV}(SOC(t)) - I(t) \cdot R_0 - V_{C1}(t) \quad (2.13)$$

Where, $V_{C1}(t)$ is a voltage component which can describe how the voltage changes due to slower electrochemical or thermal processes. Their parameters, as for example, (polarization resistance) and (polarization capacitance) are SOC-dependent functions whose identification needs experimental data such as pulse discharge tests [49].

But $V_{C1}(t)$ can be written as follows in terms of current,

$$V(t) = V_{OCV}(SOC(t)) - I(t) \cdot R_0 - I_{R1}(t) \cdot R_1 \quad (2.14)$$

As the current will pass through R_1 and C_1 , then [52],

$$\begin{aligned} I(t) &= I_{R1}(t) + I_{C1}(t) \\ I_{C1} &= C_1 \frac{dV_{C1}}{dt} \end{aligned} \quad (2.15)$$

And since $V_{C1} = R_1 \cdot I_{R1}$ [52],

$$\frac{d(I_{R1}(t))}{dt} = -\frac{1}{R_1 C_1} (I_{R1}(t) - I(t)) \quad (2.16)$$

Thevenin models are able to work for transient simulation and SOC estimation [51]. This combination of R_0 , R_1 , and C_1 is mostly referred to as the First-Order Thevenin Model.

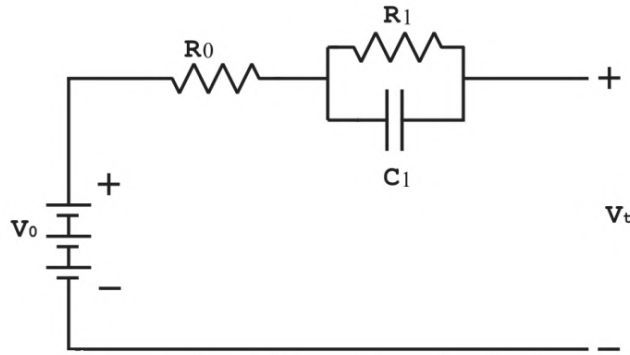


Figure 2.10: First Order Thevenin Model [51]

If we add another R-C model in series after the above shown fig. 2.10, we get the Second Order Thevenin Model, making it more complex and accurate [51]. Therefore, it finds applications in areas requiring transient behaviour, such as regenerative braking in EVs [49].

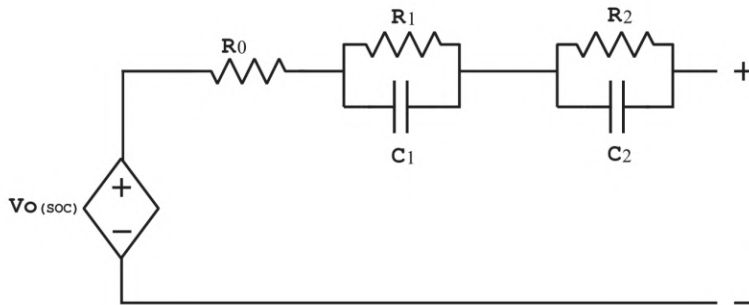


Figure 2.11: Second Order Thevenin Model [51]

But as we increase the number of blocks in the Thevenin Model, it becomes more accurate, but at the same time, the computational cost increases, and thus it needs more optimization as it is more data-dependent.

	Electrochemical Model	Mathematical Model	Equivalent Circuit Model
Accuracy	High, detailed thermodynamic and kinetic analysis	Moderate, depends on equations used	Moderate to High, depends on circuit complexity
Complexity	Very high, involves partial differential equations	Low to Moderate, involves algebraic or empirical equations	Moderate, uses electrical components to simulate behaviour
Computational Cost	High, requires significant resources	Low, efficient real-time implementation	Moderate, can be optimized for real-time applications
Parametrization	Requires detailed knowledge of battery chemistry	Simple, based on data sheet or empirical curves	Moderate, may involve experimental tests for certain parameters
Applications	Cell design, detailed battery behaviour study	Basic BMS design, SOC estimation	BMS, transient behaviour simulation, and hardware-in-the-loop (HIL) applications
Examples	Newman model, porous electrode theory, CFD	Shepherd model, stochastic models	Rint, Thevenin, Double Polarization models

Table 2.2: Comparison of Electrochemical, Mathematical, and Equivalent Circuit Models.

	Rint Model	Thevenin 1st Order Model	Thevenin 2nd Order Model
Structure	Single resistor and voltage source	Adds one RC network for transient behaviour	Adds multiple RC networks for enhanced accuracy
Accuracy	Low, ignores transient effects	Moderate, captures short-term dynamics	High, captures detailed transient and steady-state behaviour
Complexity	Very low	Moderate	High
Computational Cost	Minimal	Moderate, suitable for real-time applications	High, requires careful optimization
Parametrization	Simple, based on data sheet	Requires experimental data (e.g., Pulse Discharge Test)	Requires extensive experimental testing
Applications	Basic BMS design	SOC estimation, real-time simulations	Transient behaviour study

Table 2.3: Comparison of Equivalent Circuit Models.

2.5.4 Current Research with ECH models

2.5.4.1 Comparative Studies of Battery modelling Approaches

Campagna *et al.* [49] presents three different approaches for modelling batteries, whose most important point is the identification procedure of their parameters. Among these, two require only data from manufacturers' data sheets without any heavy experimental activity in a laboratory, while the third approach has an experimental validation. The identified models are then tested on both steady-state discharge curves and transient experimental results.

2.5.4.2 Advanced State Estimation Techniques

Xu *et al.* [53] proposes a multi-time-scale SOC and SOE (State of Energy) estimator using dual H infinity filters. The model will be able to consider parameters of different time-scale variations, ensuring dynamic robustness.

2.5.4.3 Dynamic and Non-linear Battery Models

Gao *et al.* [54] dynamic lithium-ion battery model embeds non-linear equilibrium potentials, temperature dependencies, and transient behaviours. The model, which is based on First Order Thevenin ECM model. Though it was developed in the VTB system simulation software, it can be integrated quite well into MATLAB's modelling using the Simulink environment.

2.5.4.4 Multi-Factor Resistance Estimation

Chen *et al.* [55] came up with the Multi-Factor Dynamic Internal Resistance Model, MF-DIRM, including an error compensation strategy. The resistance estimate provided by their model is highly accurate, factoring in temperature, SOC, and discharge rate. The focus was more on the estimation of OCV, R_0 , R_1 , and C_1 parameters to predict the accuracy of the algorithm developed to represent the battery.

2.5.4.5 Thermal Management in the MATLAB Simulation

Kim *et al.* [56] performed a simulation of cooling performance using the MATLAB Simulink-Simscape environment for lithium-ion battery packs. There were two different cold plates that were tested in terms of thermal resistance and their cooling efficiencies: Type I and Type II. The thermal characteristics simulated with MATLAB demonstrated that heaters had operated at temperatures 10% higher compared to Li-ion cells under the same conditions. Their results conclude that Type II cold plates perform better in cooling, and these are validated both by simulation and experiment.

2.5.5 Summary

The ECM is able to model battery performance in simulation by encapsulating the electro-chemical nature of the battery. This is highly useful in view of the fact that running detailed CFD for such nature in simulations is computationally expensive. Thermal nature, however, which is highly essential when assessing different thermal management systems, has not been explored as well. When such studies are carried out, they are normally done in the Simscape environment.

Simscape is part of the suite of MATLAB Simulink, and through it, the modelling of physical components is realized with physical connections; this makes it more amenable for HIL testing. [57]. However, it has better application at component-based systems and not large-scale system-level modelling. At a system level of modelling, the physical signals have to be converted to electrical signals, increasing computational overhead over time. On the other hand, Simulink offers model-based design in a virtual environment [58], making it more suitable for HIL environments. Simulink's capabilities allow for real-time readiness, seamless deployment, and efficient handling of complex models.

Finally, simulation of various thermal management systems is quite necessary; physically, the experiments cannot be performed by pushing batteries to such extreme limits, which are risky. Simulations also enable the creation of test cases that model scenarios which, for one reason or the other, might involve risk or, just difficulty, cannot be witnessed in real-time with CFD simulations. In light of the application of the model within the automotive industry, MATLAB Simulink becomes a better option for use within complex models, especially those designed for HIL testing.

2.6 Thermal Analysis in Battery

From section 2.3.1, 2.3.2, and 2.3.3, it is observed that lithium-ion cells have to be modelled with good accuracy in order to make certain that the battery is safe and efficient for electric vehicles under dynamic cycling profiles. Because of this fact, CFD studies are usually carried out since they give high accuracy in model behaviour prediction. However, these simulations incur a high cost of computation and time; hence, real-time analysis in dynamic scenarios is not possible by applying them.

On the other side of the extreme are thermal-lumped models as their simpler yet effective representations. In fact, the thermal behaviours captured by such kinds of modelling retain a lot from high-fidelity or distributed models but at way lower computational costs [59] [60]. Since they approximate the spatial temperature gradients with any system of ordinary differential equations, thermal-lumped models allow real-time implementations and therefore are well-fitted for MIL and HIL testing. These models enable studying not only dynamic behaviour but also the assessment of physical control modules for BTMS.

Another important feature of this model is that all the ECM parameters are functions of SOC and battery temperature. As the basic application is going to be a lumped model, we can assume that for a particular material, temperature is going to be uniform and there is one skin temperature characterizing the whole battery [61]. Thus we have a simple energy balance equation:

$$\dot{Q} = mC_p \frac{dT}{dt} \quad (2.17)$$

As for various modes of heat transfer, we have the following generalized equations for heat fluxes [62] from which we can extract the heat flow equations:

$$\begin{aligned} \text{Conduction Heat Flux } (q_x^n) &= \frac{k}{L} (T_s - T_d) \\ Q_{cond} &= \frac{k}{L} A (T_s - T_d) \end{aligned} \quad (2.18)$$

Where Q_{cond} gives conduction heat flow from source temperature T_s to destination temperature T_d . As k and L are constants, they can be denoted as h_{cond} thus equation 2.18 becomes:

$$Q_{cond} = h_{cond}A (T_s - T_d) \quad (2.19)$$

$$\begin{aligned} \text{Convection Heat Flux } (q^n) &= h_{conv} (T_s - T_d) \\ Q_{conv} &= h_{conv}A (T_s - T_d) \end{aligned} \quad (2.20)$$

In equation 2.20, Q_{conv} is convection heat flow h is the convective heat transfer coefficient. Convection heat flow can be either natural or forced or may be even both depending on the scenario, thus $h_{conv} = h_{natural} + h_{forced}$ and h_{forced} are the coefficients dependent on the flow of fluid [62]. Thus, equation 2.20 becomes,

$$Q_{conv} = (h_{natural}A + h_{forced}A) (T_s - T_d) \quad (2.21)$$

$$\begin{aligned} \text{Radiation Heat Flux } (q_{rad}^n) &= \epsilon\sigma (T_s^4 - T_d^4) \\ Q_{rad} &= \epsilon\sigma A (T_s^4 - T_d^4) \end{aligned} \quad (2.22)$$

As we are designing a complete closed-loop system, the heat exchange between the working fluid and ambient will also be taking place via a heat exchanger, and this can be resolved with bulk flow heat flux [62]:

$$Q_{bulk} = \dot{m}C_p (T_s - T_d) \quad (2.23)$$

Heat Flow	Equation
Conduction	$Q_{cond} = h_{cond}A (T_s - T_d)$
Convection	$Q_{conv} = (h_{natural}A + h_{forced}A) (T_s - T_d)$
Radiation	$Q_{rad} = \epsilon\sigma A (T_s^4 - T_d^4)$
Bulkflow	$Q_{bulk} = \dot{m}C_p (T_s - T_d)$

Table 2.4: Heat Flow Equations

Using these equations, thermal equation in terms of the battery can be modified to suit equation 2.17 which was used by Giammichele *et al.* [25]:

$$\dot{Q}_{batt} = Q_{conv} + Q_{rad} - mC_p \frac{dT}{dt} \quad (2.24)$$

2.7 Model Parameter Estimation

As seen in the section 2.5.2, mathematical models need experimental data for calibration and validation to develop the battery model. As discussed previously, for estimating battery behaviour, the following parameters are needed.

- Open Circuit Voltage (OCV)
- Battery Internal Resistance (R_0)
- Polarisation Resistance and Polarisation Capacitance (RC)
- Entropic Heat Coefficient ($\partial V_{ocv} / \partial T$)

To estimate these parameters, following experiments provide essential data for calibrating and validating accurate battery models.

2.7.1 Low Current OCV Test

Low Current OCV test, also known as Static OCV test, is used to obtain the OCV-SOC curve, which shows the open circuit voltage for each SOC level. This test is foundational for establishing the OCV-SOC relationship [63]. In this test, a DC voltmeter is used to measure battery cells' OCV under no-load conditions and at constant temperatures for various SOC values. The battery is first fully charged and then discharged at a very low C rate to keep the battery temperature stable. Once SOC is lowered to the required point of measurement, the battery is disconnected and allowed to rest until the $\partial V_{ocv} / \partial t$ is less than 1 mV/h . This test is repeated until the battery is fully discharged. This step is replicated for various temperature ranges to get OCV values for different SOC and temperature ranges [64] [65]. Fig 2.12 shows how OCV changes based on temperature and SOC.

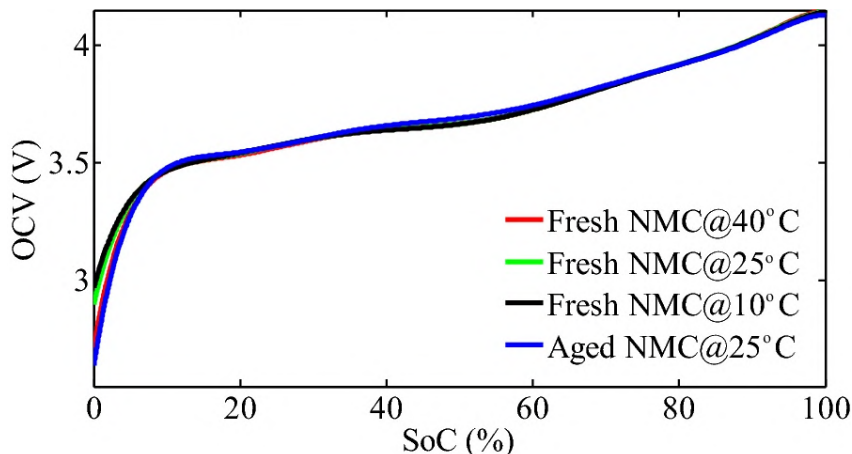


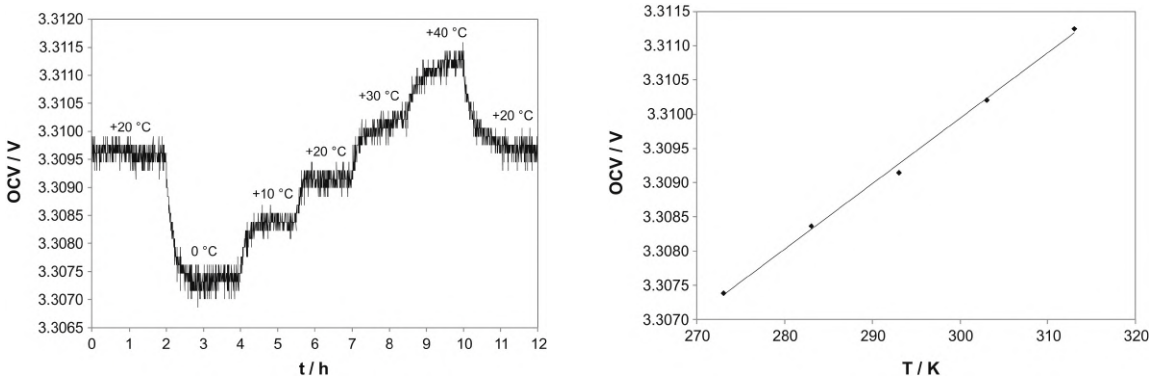
Figure 2.12: SOC-OCV Curve for NMC Battery [64]

Though the process gives accurate behaviour of the battery's OCV, the test takes a long time as the rest period of the battery is high and the battery needs to be held at constant temperature as the smallest fluctuation can vary the behaviour of the OCV [66]. But this test is necessary as it helps to identify any defects in the battery which can result in abnormal discharge rates. Also, this test only helps to identify OCV of the battery and not other

dynamic behaviour. Thus, additional experiments need to be performed for the analysis of the accurate battery behaviour.

2.7.2 Potentiometric Test

Potentiometric test is used to measure the EHC value of the battery. This is adjacent to Low Current OCV test, as once the OCV is estimated for various temperatures and SOC ranges, the slope of the linear relationship between OCV and temperature gives the appropriate EHC for the battery. The only difference is that once the desirable SOC is reached, the temperature is cycled through desired ranges and the battery is left to rest until OCV stabilizes for each temperature range [67] [25].



(a) OCV measured for 42-Ah Prismatic Cell during thermal cycle at SOC = 70% (b) OCV as a function of temp for 42-Ah Prismatic Cell at SOC = 70%

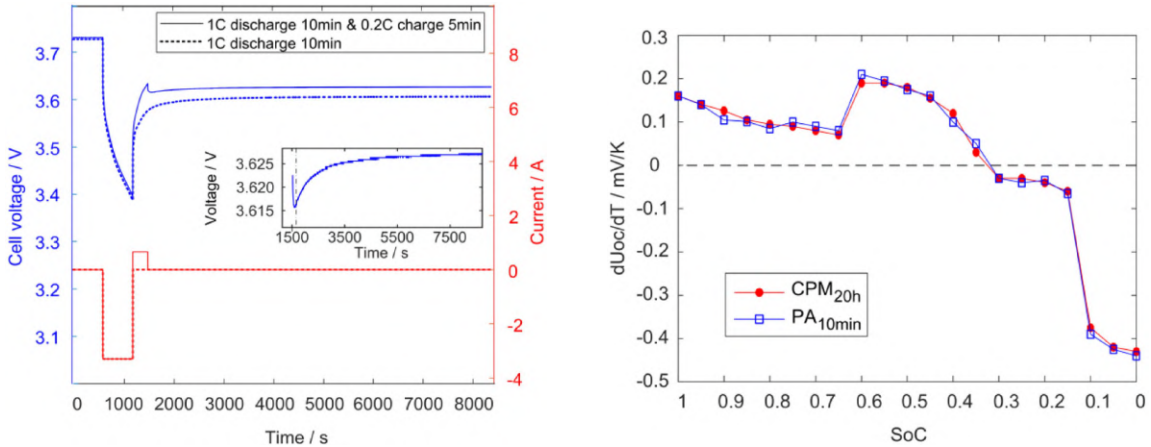
Figure 2.13: Entropic Behaviour of 42-Ah Prismatic Cell [67]

Fig 2.13 shows how OCV is measured by cycling the temperature of the battery, fig 2.13b shows how the EHC can be estimated with the help of OCV and its variation with respect to temperature. As the process is similar to the Low Current OCV test, the main drawback of this test is that it is time-consuming. To bypass this time, Lin *et al.* decided to apply a small reverse current, named the Positive Adjustment (PA) method, to reduce relaxation time to 10 minutes with good accuracy compared with the Conventional Potentiometric Method (CPM) which can be seen in fig 2.14 [68]. Lin *et al.* observed that CPM can take from 241 to 451 hours (11.5 to 21.5 hours per SOC measurement), whereas PA only took 32.3 hours (1.38 hours per SOC measurement) respectively, which includes 1 to 3 hour relaxation time when SOC was at 100% and 0% respectively [68].

To ensure accurate results, it is important to achieve and maintain thermal equilibrium. Williams *et al.* achieved this by using the Immersion Cooling Method, where the battery was submerged in a dielectric fluid for better thermal uniformity across the battery [69].

2.7.3 Calorimetric Test

As the potentiometric test can be time-consuming, an alternative test can be performed for EHC estimation. From equation 2.7, it can be seen that the heat produced by the battery is composed of reversible and irreversible heat-producing factors. Thus, the change in heat produced by the battery during its charge and discharge cycle can be used to estimate the



(a) OCV measured for Sanyo 18650 Cell at 50% SOC with PA Method (b) EHC Value for Sanyo 18650 Cell for CPM and PA Methods

Figure 2.14: Pulse Relaxation and EHC value for Sanyo 18650 Cell [68]

EHC value as the reversible heat term will remain identical in both scenarios, so rearranging the equation 2.7 will give:

$$\frac{\partial V_{OCV}}{\partial T} = \frac{Q_{discharge} - Q_{charge}}{IT(t_{discharge} - t_{charge})} \quad (2.25)$$

Where, Q_{charge} , and $Q_{discharge}$, refers to the heat generated and t_{charge} and $t_{discharge}$ indicate the time required for charge and discharge, respectively. This method of estimating EHC by heat generated during the charge and discharge cycle is known as the Calorimetric Method. For this test, specialised calorimetric equipment is needed, such as an Accelerating Rate Calorimeter (ARC) or Isothermal Heat Conduction Calorimeter, needed to create and maintain temperature uniformity across the battery, in turn increasing the experimental cost [66].

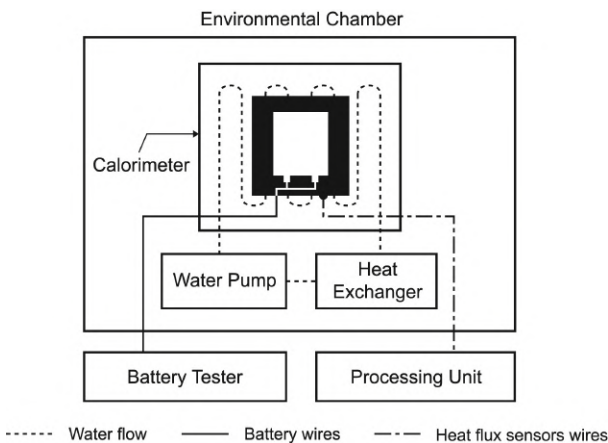
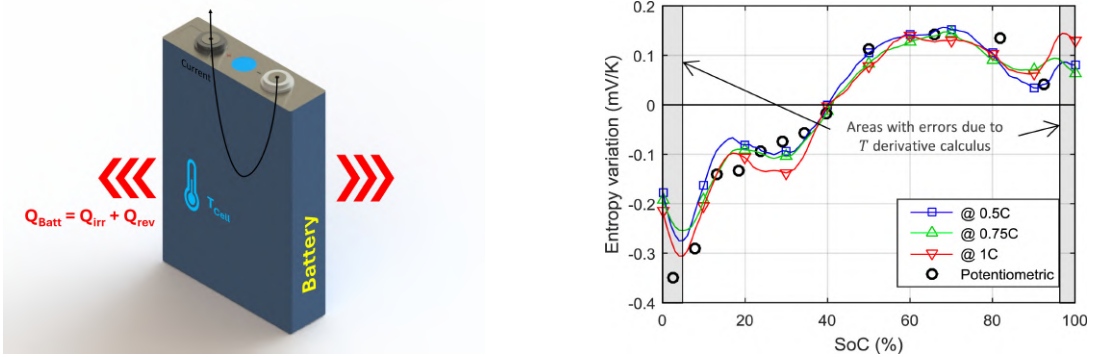


Figure 2.15: General Schematics for Calorimetric Test Setup [70]

Fig 2.16b shows the calorimetric method is good and can be used at different C rates, except below 5% and above 95% SOC. Damay *et al.* says the reason behind this observation is "*T derivative calculus smooths their quick variations*" making them biased in those SOC ranges [71]. Also, calorimetric data can be less accurate when the system contains a significant

quantity of non-participating thermal mass, as is commonly encountered with lithium-ion cells as a result of items like packaging and current collector tabs that don't participate in electrochemical reactions [67]. The test can be completed in less time compared to the potentiometric test; only EHC can be identified with this method.

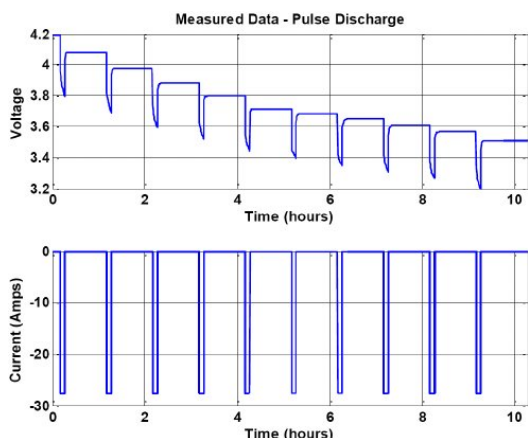


(a) Principle behind Calorimetric Method (b) EHC vs SOC at different C rates using Potentiometric Test data as Baseline [71]

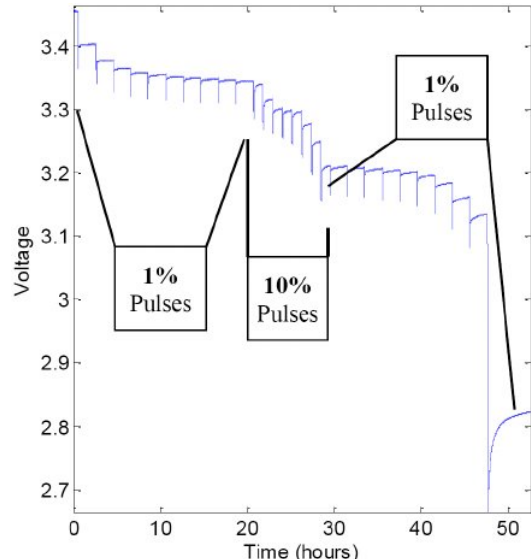
Figure 2.16: Principle Behind Calorimetric Method and EHC vs SOC

2.7.4 Pulse-Relaxation Test

Previously discussed tests only discuss the OCV and EHC estimation, thus we need tests which can estimate R_0 and RC parameters. The Pulse-Relaxation Test sends pulses of current interspersed with relaxation times and uses these to estimate R_0 and RC parameters based on voltage response, usually using the constant current pulses for both charge and discharge with a specific time interval [72].



(a) Pulse-relaxation test at 10% SOC interval



(b) Pulse-relaxation test at uneven SOC breakpoints with 1% capacity pulses at high and low SOC regions and 10% capacity pulses in the mid-SOC range

Figure 2.17: Pulse-Relaxation Test [73]

ECM parameters, such as OCV , R_0 , and RC values, can be estimated by using a layer approach, where the entire data can be broken into small profiles (fig. 2.18) to derive the parameters. Jackey *et al.* [73] used two approaches, one with constant pulse discharge at 10% SOC interval (fig. 2.17a), which is the most common approach confirmed by Perez *et al.* [72], along with a dynamic approach where the pulses were 1% capacity of the battery at minimum and maximum regions of SOC, whereas 10% capacity pulses were used in mid regions of SOC where the voltage is usually stable (fig. 2.17b).

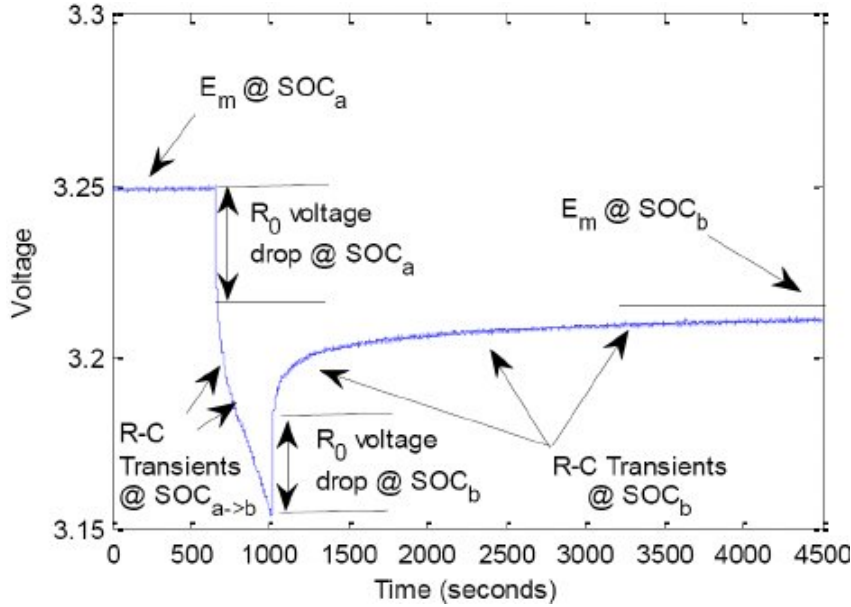


Figure 2.18: Single Voltage Pulse Parameter Identification [73]

Fig. 2.18 shows how the voltage pulse is divided into various parameters. Jackey *et al.* [73] referred to OCV as E_m . When current is drawn from the battery, SOC changes from a to b. The sharp drop in the voltage is due to the internal resistance of the battery, and the transient curve which is seen when current is constant is due to RC parameters. As soon as the current is cut off, the sharp rise in voltage is again due to internal resistance and then the transient relaxation is seen due to RC parameters till the OCV is stabilized. Repeating the test at different temperatures allows estimation of R_0 and RC parameters across the SOC along with OCV .

2.7.5 Hybrid Pulse Power Characterisation Test

Hybrid Pulse Power Characterisation (HPPC) Test, also known as High Power Pulse Characterisation Test, is a standardised test procedure for evaluating battery performance in the field of EVs and energy storage applications [74]. It can be said that this test is built upon the Pulse-Relaxation test, which falls under ISO: 12405. The battery is rested at constant temperature and provided with a discharge pulse along with the charge pulse, where the discharge pulse is the maximum C-rate specified by the manufacturer for 18 sec, which is followed by a charge pulse 75% of the maximum C-rate with a 40 sec pause between the two [75], which can be referred to in the fig. 2.19. The process will be repeated for each SOC level except for the maximum and minimum value of SOC, where the chances of overshooting the voltage from the recommended threshold are high; in such cases, the current level can be adjusted for the lower SOC range [75].

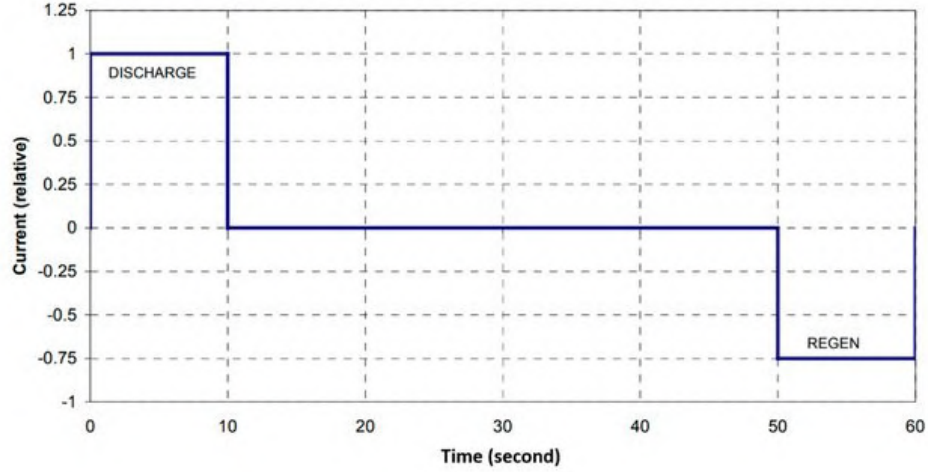
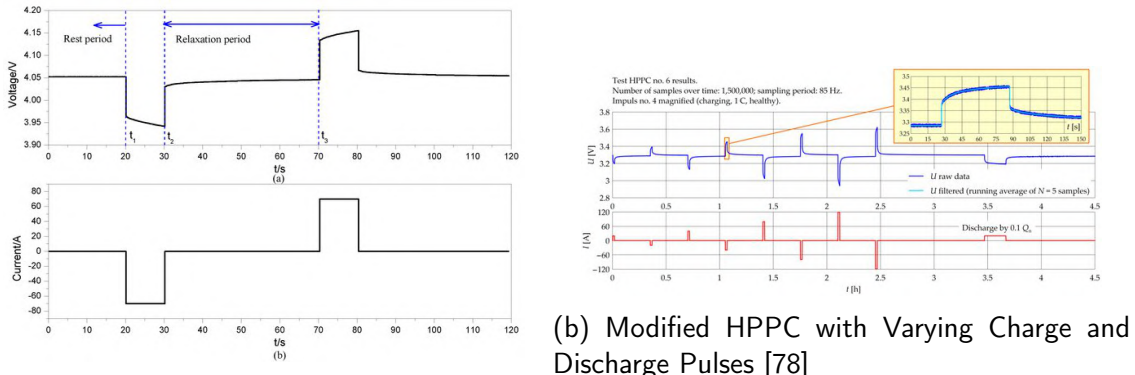


Figure 2.19: Standard HPPC Test Cycle [76]

Though this standard test process is developed for EVs and energy storage applications where the battery is exposed to dynamic loading [74], researchers used the simplified HPPC test where the charge and discharge pulse is of the same intensity or modified HPPC test where the charge and discharge pulses' intensity is the same for one cycle [77], but the C-rate increases until the maximum recommended C-rate pulse is reached for a single SOC percentage [78]. Depending on the SOC level, the pulses can be adjusted accordingly. Again, repeating the test at different temperatures allows estimation of R_0 and RC parameters across the SOC along with OCV.



(a) Simplified HPPC with Equal Charge and Discharge Pulse [77]

(b) Modified HPPC with Varying Charge and Discharge Pulses [78]

Figure 2.20: Common HPPC Test Modifications for Estimating ECM Parameters

HPPC test is more dynamic as it allows the tester to observe the behavioural changes during the charge and discharge. This is more important for batteries with high power and which face dynamic loading, such as EVs where the vehicle constantly accelerates and decelerates. The parameter estimation can be complex but is accurate to the Pulse-Relaxation test.

In these experimental approaches, it can be observed that the core testing method is common in all the testing. The discharge pulse is applied, and the battery is allowed to rest at a particular temperature. The experiment changes based on the current applied, the time for

which the battery is allowed to relax, and the section chosen for the measurement (before or after the pulse).

Test Name	Parameters Estimated	Advantages	Disadvantages
Low-Current OCV	OCV	<ul style="list-style-type: none"> Highly accurate OCV–SOC curve Detects cell defects 	<ul style="list-style-type: none"> Very long test duration Only yields OCV behaviour
Potentiometric	$OCV, \frac{\partial V_{ocv}}{\partial T}$	<ul style="list-style-type: none"> Direct measurement of EHC PA method drastically reduces total test time 	<ul style="list-style-type: none"> Still time-consuming without PA Requires tight thermal control
Calorimetric	$OCV, \frac{\partial V_{ocv}}{\partial T}$	<ul style="list-style-type: none"> Faster than potentiometric Works over various C-rates 	<ul style="list-style-type: none"> High equipment cost Biased at extreme SOCs ($<5\%$, $>95\%$) Affected by non-reactive thermal mass
Pulse-Relaxation	OCV, R_0, RC	<ul style="list-style-type: none"> Estimates both resistive and dynamic parameters Flexible SOC spacing 	<ul style="list-style-type: none"> Requires careful segmentation and fitting Rest periods still needed
HPPC	OCV, R_0, RC	<ul style="list-style-type: none"> Industry-standard for EVs/ESS Captures dynamic loading behaviour 	<ul style="list-style-type: none"> Complex setup and data processing Risk of overshoot at SOC extremes—may need adjusted currents

Table 2.5: Comparison of different testing methods for ECM parameter estimation.

After careful analysis, Calorimetric testing can be excluded due to high equipment cost and error sensitivity at extreme ends of SOC. The Potentiometric test can be coupled with the Low-Current OCV test, where the battery can be discharged at a very slow C rate (0.1 to 0.05 C) to avoid long waits in large batteries. Moreover, techniques such as positive adjustment suggested by Lin *et al.* [68] in the potentiometric test for quick relaxation, if deployed by requesting a counter current pulse to the previous pulse in Pulse-relaxation, transforming it into a HPPC test. This explains why the HPPC test has a shorter relaxation period compared to the Pulse-relaxation test. This not only will make the HPPC test useful for estimation of ECM parameters but also OCV and EHC parameters as well, which is not well explored.

2.8 Conclusion

The core development in the field of sustainable energy systems is continuous evolution in battery technology, particularly for application fields like EVs and renewable energy storage. The sections below review the advances in performance and safety of the critical components of lithium-ion battery systems: architecture, thermal management, and modelling. It therefore follows from insights into these studies that thermal studies and modelling are indispensable ingredients for such a wide-ranging set of problems in contemporary battery systems.

In the present day, modelling of batteries has always been the heart of battery research since it will make the forecast of system behaviour possible under a wide range of conditions and provides a chance to optimize energy systems. Such types of approaches have been categorized

mainly into three groups: electrochemical, mathematical, and equivalent circuit models. These models represent the internal chemical reaction, ion diffusion, and thermal interaction in great detail; thus, they are most important when mechanisms of degradation have to be understood and new chemistries are under design. However, most of the applications involving real-time models are computationally too heavy.

The exact opposite of it is a mathematical model with simplification approximation regarding battery performance in stationary and transient conditions, with reduced computing load. Equivalent circuit models offer a proper balance between precision and computation time and thus are very well suited for real-time applications, such as Hardware-in-the-Loop simulations. Each of the above models has very specific uses, and there are thermal aspects in all three where integration, research, and development need to be done.

While lithium-ion batteries maintain prime importance from the reliability and safety point of view, operating within narrow windows of temperature in normal conditions, this review has discussed abusive thermal runaway conditions of a mechanical, electrical, or thermal origin that may trigger the same; therefore, such disastrous consequences urgently need to be addressed by introducing the correct Battery Thermal Management System right at the very design stage in a battery itself.

Among them, three BTMS approaches have been explored: air cooling, liquid cooling, and immersion cooling. Each of them represents one critical step with regard to thermal risk mitigation. On the contrary, air cooling is simple and low in cost, while the relatively poor thermal conductivity limits its use to high-energy-density batteries. Liquid cooling encompasses both direct immersion and indirect cooling techniques for good heat dissipation but needs to be carefully designed with system reliability and efficiency in mind. Among those, immersion cooling has emerged as one of the promising solutions, allowing battery cells to come into direct contact with each other, hence assuring better thermal regulation.

Inclusions of thermal considerations at the development stage of modelling frameworks are leaping into the future. These will inherently embed thermal dynamics with electrochemical and equivalent circuit models for the more realistic pre-determination of battery behaviour, especially under dynamic cycling profiles typical for EVs and renewable energy applications. All simulation models are integrated in a robust environment in MATLAB, where MIL and HIL testing methodologies can also be applied. All these techniques effectively simulate real-time operating conditions that help optimize control algorithms, discover possible thermal problems much sooner than previously envisaged, and reduce development times by lowering overall developmental costs.

With this in perspective, future research work should target developing multi-physics models that will combine electrochemical, thermal, and mechanical dynamics in harmony. Such models have to be well-balanced with high fidelity and computational efficiency so that their applications can be realized in real time. Further improvements in computation techniques such as machine learning and reduced-order modelling may allow improvements in predictive capabilities within these frameworks. With correct sets of experiments, these models will be more realistic and will help in analysing a few complex scenarios with less computational power.

Material innovations, too, are going to form a very critical ingredient in the thermal management of all these advances. Development of lightweight, high thermal conductivity materials, and advanced technologies for cooling including phase-change materials and hybrid systems

holds great promise. Further, this shall be supplemented by standardization in testing methodologies at BTMS levels and thermal modelling to ensure standardization and reliability in the industry.

The mutual interactions among the subjects of modelling, thermal management, and safety represent the driving feature of the next generation of battery systems. Above all, the possibility of avoiding thermal runaway and having only fine thermal regulation using state-of-the-art modelling and management will surely provide the way to drastic improvements in performance, safety, and cycle life. Thermal considerations within the MATLAB modelling and simulation environment raise certain possibilities regarding how these bridge the gap between theory and practice.

It shall be presented in a holistic manner in approach: model accuracy with thermal ingenuity. It would also signal the transformation that has taken place in battery technologies as further advances press onward toward a secure, efficient, and enduring energetic dream.

Chapter 3

Objectives

The main objective of this research is to design and evaluate an efficient Battery Thermal Management System (BTMS) by incorporating multi-physics modelling approaches that integrate electrochemical, thermal, and mechanical dynamics in real-time. This study will focus on gathering OCV-SOC-Temperature curves and Entropic Heat Coefficient ($\partial V_{OCV}/dT$) data from potentiometric tests. The outcome of the experimental study will be used to facilitate parametrisation of the equivalent circuit and heat generation model for electric vehicles and energy storage applications. Specific objectives of this study are as follows:

1. Implementing a coupled electro-thermal model for a single LF105 lithium-ion (Prismatic) cell to simulate voltage response, heat generation, and heat dissipation under natural and forced convection scenarios.
2. Perform a temperature-stepped potentiometric test at fixed SOC levels to experimentally extract OCV and EHC parameters by observing voltage response under thermal equilibrium
3. Analyse the voltage relaxation and change in voltage w.r.t. time to identify stabilized OCV points and apply correction or smoothing techniques to reduce the impact of thermal relaxation delays for precise EHC estimation.
4. Identify the reversible heat generated using derived EHC and temperature trends and integrate EHC parameters into the heat generation model.
5. Run simulation scenarios using available OCV and temperature data to qualitatively assess thermal trends. Document limitations due to unavailable ECM data.
6. Outline a path for future model development, calibration, parameter identification and complete validation of the model.

Chapter 4

Experimental Setup

As discussed in chapter 3, the aim of this study is to model the battery behaviour for various cooling methods in a simulated environment for LF105 (3.2 V 105 Ah), a LiFePO₄ Prismatic Battery Cell. Thus, to create an accurate ECM model of this battery, the experimental data are required, which will be derived from the Potentiometric test for OCV and EHC and HPPC test (not part of current thesis) for R_0 and RC parameters, as discussed in section 2.7. This study will use immersion cooling to control the battery temperature in a thermal chamber specifically designed for this study, which was inspired by Williams *et al.*'s [69] work. Nominal Technical Parameters can be seen in table 4.1.

Parameter	Sub-Parameter	Value	Units	Remark
Nominal Capacity	–	105	Ah	(25 ± 2)°C, Standard Charge/Discharge
Nominal Voltage	–	3.2	V	–
Standard Charge/Discharge	Current (Charge/Discharge)	0.5 / 0.5	A	(25 ± 2)°C
	Cut-off Voltage (Charge/Discharge)	3.65 / 2.5	V	–
Max Current Charge/Discharge	Constant Charge/Discharge	1 / 1	C-rate	–
	Pulse Charge/Discharge (s)	1 / 3	C-rate	–
Charge Temperature Discharge	–	0 55	°C	–
Temperature	–	-20 55	°C	–
Dimensions	Width	130.3 ± 0.3	mm	–
	Height (Total)	200.5 ± 0.5	mm	–
	Thickness (30%-40% SOC)	36.7 ± 0.5	mm	–
	Tabs Distance	67 ± 0.1	mm	–
Weight	–	1980 ± 100	g	–

Table 4.1: Technical Parameters for LF105 (3.2 V 105 Ah) Battery by Manufacturer

For the Potentiometric test, it was decided to test for 10°C - 50°C. This is to incorporate the optimum temperature range of 20°C - 40°C and external outliers, which will help to estimate

EXPERIMENTAL SETUP

the trend of battery behaviour outside of the optimal range. As for the immersion fluid, it has to be dielectric and thermodynamically stable between the experimental temperature range. After careful consideration, Promosolv DR3 was selected and its properties can be seen in table 4.2.

Specification	Values	Units
Boiling Point	61	°C
Freezing Point	-135	°C
Density	1520	kg/m ³
Dynamic Viscosity	0.00075	Pa · s
Specific Heat	1170	J/kgK
Thermal Conductivity	0.069	W/mK
Dielectric Strength	25	kV

Table 4.2: Properties for Promosolv DR3 [79] [80]

The chiller used was Thermo Scientific Accel 500 LC with a temperature range of -10°C to 80°C, which was a good fit for the series of tests to be performed. The complete schematic diagram of the experimental setup can be seen in fig. 4.1. This chiller can also be automated, which will help in controlling set temperature precisely as the wait time is high in this test [81].

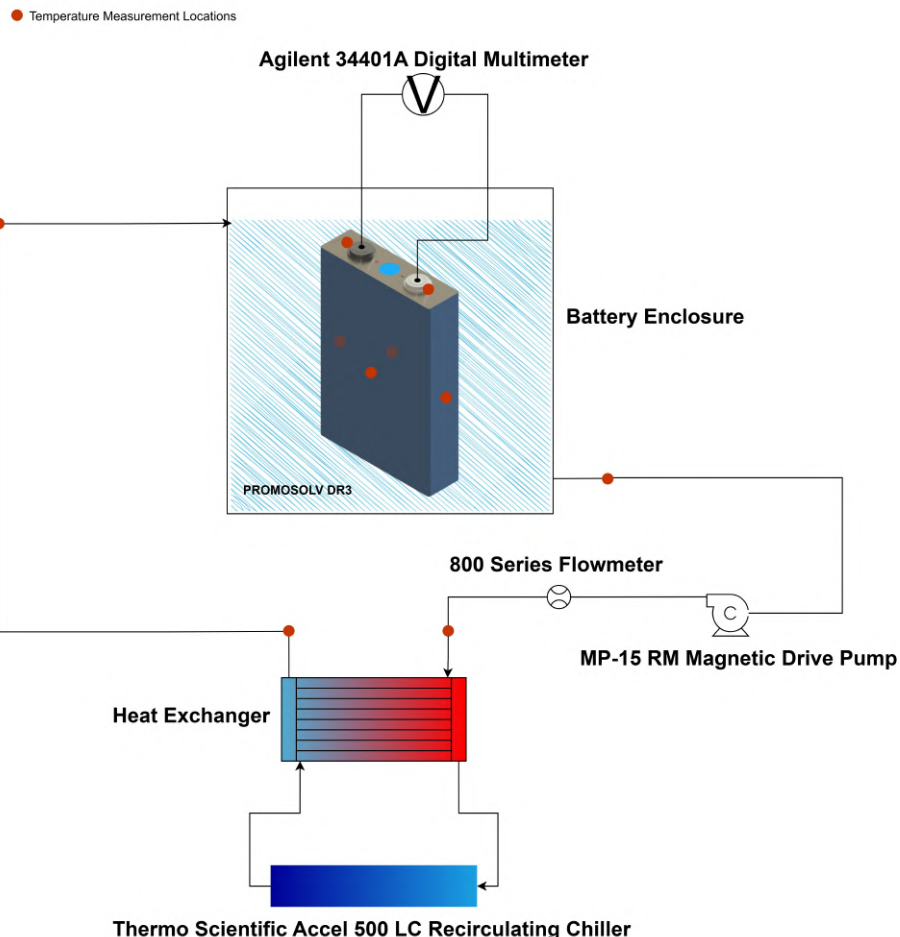


Figure 4.1: Schematic Diagram of Experimental Setup

MP-15 RM, a magnetic drive pump (max flow rate of 6 LPM), was used to pump PROMOSOLV DR3 around the loop. This specific pump was selected as PROMOSOLV DR3 has low viscosity which might cause leaks between the seals at connection points, so the pump with decoupled motor and pump drive is a good fit [82]. It can also be observed that the pump is placed downstream of the battery enclosure to ensure active removal of heat while coolant returns from the heat exchanger and no addition of heat takes place during this return. This setup is not suggested for an active cooling setup, but as the battery was set only at a constant temperature (max to be at 50°C), the pump's life will not be affected noticeably.

To measure the voltage, Agilent (currently known as Keysight) 34401A Digital Multimeter was used, which has a precision of 6^{1/2} digits. This allows the measurement in macro-volts, confirming that the voltage is stabilized enough. As for temperature measurement, 11 Class 1 T-type thermocouples were used, where 2 were for battery tabs, 4 were on each face of the battery, 4 at the inlet and outlet of the chamber and heat exchanger, and the last one for ambient temperature. For measurement, National Instruments NI 9213, a thermocouple input module, was used to connect thermocouples to LabVIEW. To measure the flow, NSF Approved 800-Series Turbine Flow Meter (Model - 865) was used. The flow meter has a range from 0.25 to 6.5 LPM which is sufficient for the selected pump. The output is in the form of pulses which are read via NI 9205, a C Series voltage input module, that is used to read and measure. Both temperature and voltage measurement modules were connected with cDAQ-9174 Compact DAQ Chassis which will connect the modules to LabVIEW.

As for battery charge and discharge, EA Elektro-Automatik EA-PSB 10000 Series Bidirectional Bench Power Supply was used with a maximum voltage and current limit of 1000 volts and amps, respectively. It is a 3000 W power supply that is capable of charging and discharging multiple LF105 cells [83]. This power supply was selected as this will be most feasible for HPPC tests to be conducted in the future where we need consecutive bidirectional pulses after a specific time interval.

4.1 Experimental Rig Assembly

Polycarbonate enclosure was designed to hold the battery fully submerged. Thus, cuboid of 220×220× was designed with one inlet and one outlet port. As for the fluid path, 10 mm nylon tubing was used as the fluid is said to work with most of the polymers [84]. This big enclosure (around 7-8 liters of volume) will ensure the battery is maintained at a stable temperature. Though it is not an issue at lower temperatures due to room temperature being lower than 23 deg, there was a chance of losing heat to ambient at higher coolant temperatures. To avoid this, Expanded Polyurethane Foam was used as insulation with an easy to assemble/dismantle design. CAD design and experimental setup can be seen in fig. 4.2a and fig. 4.2b

To ensure the enclosure is leak-proof, all the panels (except the top) were glued together with chloroform. The screws on the sides were placed to hold the panels together so chloroform can be applied. As for the top panel, a gasket made out of a rubber sheet was used to create an air-tight seal. Festo QS Series Straight Threaded Adaptor was used at the inlet and outlet ports, which are threaded-to-tube style connectors for 10 mm pipes. These fittings were screwed in place with an O-ring to avoid leaks, and the rest of the pipe fittings were push-fit fittings. Only the metal T-joints were used to screw in T-type thermocouple probes to measure the temperature of the coolant during its motion. As for the connection to T-joints in the fluid loop, the same threaded-to-tube style connectors were used.

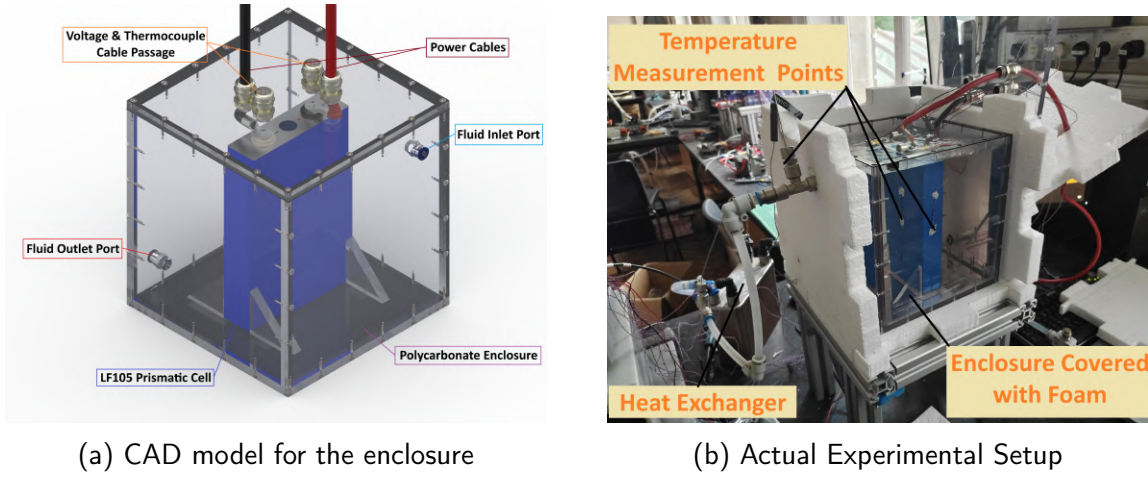


Figure 4.2: Experimental Setup

Battery had its 4 faces and 2 tabs connected to thermocouples (as shown in fig.4.1), along with the connections to the multimeter and power supply, and was placed inside the enclosure. The power cables are seen to be removed in fig. 4.2b to create a complete open circuit environment. Many researchers like Giannicchele *et al.* [25], Jalkanen *et al.* [67], Lin *et al.* [68], and Williams *et al.* [69] etc. observed that there was self-discharge and relaxation behaviour during the rest period of the battery (this will be explained in chapter 5 in detail). So, to remove the effect of self-discharge, the battery was completely disconnected from the load. Fig. 4.3a and fig. 4.3b show the closer view of the battery submerged under PROMOSOLV DR3 and completely enclosed in-operation setup respectively.

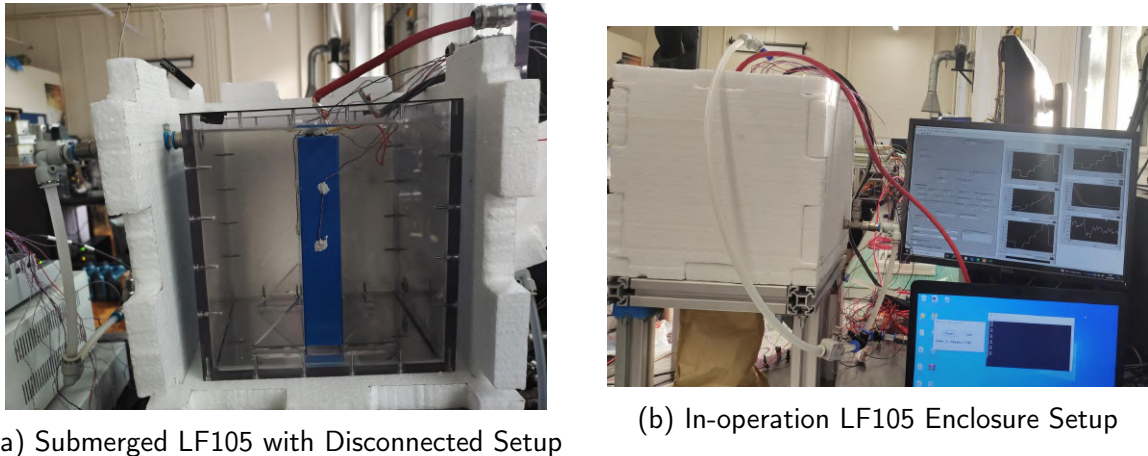


Figure 4.3: Experimental Configuration for Potentiometric Testing

4.2 Uncertainty Analysis

4.2.1 Uncertainty during Temperature Measurement

Any experiment performed has a bit of uncertainty involved in expected results and obtained results, which can be due to a variety of sources. For instance, temperature is measured with Class 1 T-type thermocouples which have a measurement accuracy of $\pm 0.5^\circ\text{C}$ [85] and the NI-9213 thermocouple input module has a measurement sensitivity of $\pm 0.02^\circ\text{C}$ [86]. So it can

be said that the $U_{thermocouple}$ and U_{DAQ} are $\pm 0.5^\circ\text{C}$ and $\pm 0.02^\circ\text{C}$ respectively. But even during the calibration of the thermocouples, uncertainty is introduced. The calibration is performed with a Resistance Temperature Detector (RTD) as a baseline where the calibration curve uses a line of best fit by using the least squares method of line of regression. The slope (m) and y-intercept (c) of the regressed line are given as follows [87];

$$y_i = mx_i + c \quad (4.1)$$

Where slope and y-intercept can be written as,

$$m = \frac{n \sum x_i y_i - \sum x_i \sum y_i}{n \sum x_i^2 - (\sum x_i)^2} \quad (4.2)$$

$$c = \frac{\sum x_i^2 \sum y_i - \sum x_i \sum x_i y_i}{n \sum x_i^2 - (\sum x_i)^2} \quad (4.3)$$

Here, n is the number of data points and x_i and y_i are i^{th} terms of x and y , respectively. The standard error of estimate for the selected samples can be estimated via the following [88];

$$\sigma_{est} = \sqrt{\frac{\sum(Y - Y')^2}{N - 2}} \quad (4.4)$$

Where Y will be the measured temperature by RTD and Y' is the estimated temperature via the calibration curve for N number of samples. For example, the equation for the thermocouple selected for the positive tab of the battery was given as,

$$Y' = 0.997 * Uncalibrated\ Temp + 0.101$$

Using this formula table 4.3 shows the $\sum(Y - Y')^2$ for the thermocouple at the positive tab of the battery. This process was repeated for all the thermocouples.

Actual Temp	Set Temp	Pos-Tab	m	c	Y'	$Y - Y'$	$(Y - Y')^2$
15.5	15	15.54			15.61	-0.11	0.01
20.3	20	20.39			20.45	-0.15	0.02
25.2	25	25.28			25.33	-0.13	0.02
30.2	30	30.19			30.23	-0.03	0.00
35.2	35	35.18	0.997912	0.100907	35.20	0.00	0.00
40.2	40	40.28			40.30	-0.10	0.01
45.2	45	45.21			45.22	-0.02	0.00
50.2	50	50.19			50.18	0.02	0.00
55.1	55	55.08			55.06	0.04	0.00
$\sum (Y - Y')^2$							0.06

Table 4.3: Standard Error of Estimate for Thermocouple

This can be used in equation 4.4 to obtain the calibration uncertainty.

$$\sigma_{est} = U_{calibration} = \sqrt{\frac{0.06}{9-2}} = \pm 0.1^\circ C$$

Additionally, there will be an error present due to noise, which can affect thermal stability during the measurement. The uncertainty due to noise can be estimated from the following equation [89];

$$U_{noise} = \frac{\sigma_d}{\sqrt{N}} \quad (4.5)$$

Where, σ_d is the standard deviation for the noise sample of N . The sample of 30 mins ($N = 3601$) with a standard deviation of $0.047^\circ C$ was taken for data of SOC = 50%. By solving equation 4.5 we get,

$$U_{noise} = \frac{0.047}{\sqrt{3601}} = \pm 0.00079^\circ C$$

As per the International Organization for Standards' (ISO) Guide to the Expression of Uncertainty in Measurement (GUM) [90], the total uncertainty can be estimated via,

$$U_{temp_{tot}} = \sqrt{U_{thermocouple}^2 + U_{DAQ}^2 + U_{calibration}^2 + U_{noise}^2} \quad (4.6)$$

$$\therefore U_{temp_{tot}} = \sqrt{0.5^2 + 0.02^2 + 0.10^2 + 0.00079^2} = \pm 0.51^\circ C$$

The uncertainties for other thermocouples can be seen in table 4.4.

Sensors	$U_{calibration}$	σ_d	U_{noise}	U_{total}
Pos - Tab	0.10	0.047	0.00079	0.51
Neg - Tab	0.06	0.039	0.00065	0.50
Face 1	0.06	0.032	0.00054	0.50
Face 2	0.06	0.029	0.00049	0.51
Face 3	0.08	0.025	0.00041	0.51
Face 4	0.11	0.021	0.00035	0.51
Chamber In	0.09	0.013	0.00021	0.51
Chamber Out	0.12	0.017	0.00028	0.53
HEX In	0.17	0.019	0.00032	0.57
HEX Out	0.28	0.021	0.00035	0.54
Ambient Temp	0.19	0.27	0.00451	0.56

Table 4.4: Overall Temperature Uncertainties

4.2.2 Uncertainties during Voltage Measurement

As for the voltage measurement, Agilent 34401A multimeter, the reading error and range error are $\pm 0.002\%$ and $\pm 0.0005\%$ for the range of 10 V. If the voltage measurement at 50% SOC is taken as 3.29058 V, the total error can be considered as,

$$U_{multimeter} = OCV \times \%error_{reading} + 10V \times \%error_{range}$$

$$\therefore U_{multimeter} = 3.29058 \times 0.002\% + 10 \times 0.0005\% = \pm 0.000115V$$

Unlike thermocouples, multimeters are not susceptible to noise error. But to verify the impact of noise on total uncertainty, equations 4.5 and 4.6 can be used. Once again, the sample of 30 mins ($N = 3601$) was taken with a standard deviation of 1.33736E-05 V, for data of SOC = 50. Thus, the noise and total uncertainty become,

$$U_{noise} = \frac{1.33736E - 05}{\sqrt{3601}} = \pm 2.22863E - 07V$$

$$U_{tot} = \sqrt{0.000115^2 + 2.22863E - 07^2} = \pm 0.000115V = \pm 0.12mV$$

Thus, the voltage measurement devices are less susceptible to noise.

4.2.3 Uncertainty during EHC Measurement

As the EHC is a relationship between the voltage and temperature, the uncertainties from both ends will propagate to the final output. To estimate such dependencies, ISO/TS 28037:2010 [91] suggests to use weighted linear regression approach. Let (x_i, y_i) be the measured pairs, with standard uncertainty $u_i = \sigma_i$ on y_i . Define weights $w_i = 1/u_i$ and $W_i = w_i^2 = 1/u_i^2$ [91, Clause 6].

4.2.3.0.1 Weighted sums.

$$\begin{aligned} S_W &= \sum_i W_i, & S_{WX} &= \sum_i W_i x_i, & S_{WY} &= \sum_i W_i y_i, \\ S_{WX^2} &= \sum_i W_i x_i^2, & S_{WXY} &= \sum_i W_i x_i y_i. \end{aligned}$$

Table 4.5 shows how the

SOC (%)	x_i	y_i	σ_i	W_i	S_W	S_{WX}	S_{WY}	S_{WX^2}	S_{WXY}
50	283.47	3.29568	0.000116	7.4427E+07					
	293.23	3.29707	0.000116	7.4391E+07					
	303.05	3.29862	0.000116	7.4352E+07	3.7174E+08	1.1265E+11	1.22628E+09	3.42086E+13	3.71619E+11
	312.84	3.30031	0.000116	7.4308E+07					
	322.64	3.30207	0.000116	7.4263E+07					

Table 4.5: Weighted Sums for SOC at 50%

4.2.3.0.2 Fit (normal equations).

Let $\Delta = S_W S_{WX^2} - (S_{WX})^2$. The ISO/TS 28037 weighted least-squares estimates of slope b and intercept a are [91, Clause 6]:

$$m = \frac{S_W S_{WXY} - S_{WX} S_{WY}}{\Delta}, \quad c = \frac{S_{WY} - b S_{WX}}{S_W}.$$

for 50% SOC data,

$$m = \frac{3.7174E + 08 \times 3.71619E + 11 - 1.1265E + 11 \times 1.122628E + 09}{3.4174E + 08 \times 3.42086E + 13 - (1.1265E + 11)^2} = 0.000164$$

$$c = \frac{1.22628E + 09 - m \times 1.1265E + 11}{3.7174E + 11} = 3.2491$$

4.2.3.0.3 Residuals and residual variance.

Define the fitted values $\hat{y}_i = mx_i + c$ and the weighted residuals.

$$r_i = w_i (y_i - \hat{y}_i).$$

The chi-squared and residual variance (a posteriori variance factor) are

$$\chi^2 = \sum_i r_i^2, \quad \nu = \frac{\chi^2}{m - 2},$$

with $\nu = m - 2$ degrees of freedom for a straight line [91, Clause 6.3]. For 50% SOC, variance can be seen in table 4.6

r_i	r^2	ν
0.000130	1.261326	
-0.000075	0.417930	
-0.000127	1.191831	1.325355
-0.000043	0.136219	
0.000114	0.968759	

Table 4.6: Residual Variance

4.2.3.0.4 Parameter uncertainties and covariance.

With $\mathbf{X} = [x_i \ 1]$ and $\mathbf{W} = \text{diag}(W_i)$, the covariance matrix is

$$\text{cov}(a, b) = \nu (\mathbf{X}^\top \mathbf{W} \mathbf{X})^{-1} = \frac{\nu}{\Delta} \begin{bmatrix} S_W & -S_{WX} \\ -S_{WX} & S_{WX^2} \end{bmatrix}.$$

Thus the (standard) uncertainties are

$$u(m) = \sqrt{\frac{\nu S_W}{\Delta}}, \quad u(c) = \sqrt{\frac{\nu S_{WX^2}}{\Delta}},$$

and the covariance is $\text{cov}(a, b) = -\nu S_{WX}/\Delta$ [91, Clause 6.3]. And as we are interested in the uncertainty at the slope, we can estimate the uncertainty at 50% SOC.

$$u(m) = u_{OCV} = \sqrt{\frac{1.325355 \times 3.7174E + 08}{3.4174E + 08 \times 3.42086E + 13 - (1.1265E + 11)^2}} = \pm 0.000004V/K = \pm 0.004mV/K$$

A useful reporting metric is the relative uncertainty of the slope,

$$u_{\text{rel}}(b) = 100 \frac{u_{OCV}}{|m|} = 2.63 \text{ \%}.$$

4.2.3.0.5 Goodness of fit.

ISO/TS 28037 recommends checking χ^2 (or ν) against expectations for $\nu = m - 2$ to judge fit quality and the consistency of stated u_i [91, Clause 6.4]. The only drawback is that this method does not account for the uncertainties in the x-axis, but by implementing thermal uncertainties in the matrix, it can solve the equation. However, complexity will increase significantly; also, there is no agreed-upon method which works best.

4.3 Experimental Procedure

LF105 (3.2V 105Ah) LiFePO₄ was put through a charge and discharge cycle to evaluate its capacity. Once the capacity was determined, the battery was fully charged and left to rest overnight (about 10-11 hours). During this time, the battery was completely disconnected from the power supply so that self-discharge would be avoided. The experiment followed the procedure used by Jaljanen *et al.* [67], where the chiller was turned on and set to 20 °C and left for 2 hours for the rest. Once 2 hours were finished, the temperature was changed to 10 °C, and was left for another 2 hours. Once these 2 hours were completed, the battery was cycled through remaining temperatures *i.e.* 20-50 °C at 10 °C interval respectively and was left for 1 and 1/2 hours each. And once the time for 50 °C was over, battery was brought back to 20 degC and was allowed to relax for 2 hours again. The data was continuously logged during the completion of the entire cycle. In short, the temperature cycle was 20-10-20-30-40-50-20 °C respectively and total time taken was 12 hours.

Once the battery was completely relaxed after 12 hours, it was discharged at 0.1C rate till SOC dropped by 10%. The discharge rate of 0.1C was selected so that battery relaxation time could be reduced for the next day's start. Once the battery was discharged, it was left to relax overnight for around 10-11 hours. As testing for a particular SOC took one full day, it took 11 days or around 143 hours, which includes additional time of 1 hour to discharge by 10% SOC.

Chapter 5

Experimental Results & Discussion

5.1 Results

Experiment was carried out as mentioned in the section 4.3. When the battery was in the relaxation phase after switching the temperature, it was observed that the voltage curve was not flat as it was expected. This phenomenon was referred to as battery equalisation and self-discharge and was observed in many prominent studies such as Williams *et al.* [69] and Bazinski *et al.* [92] etc. . Also, during the charge phase, it was observed that the voltage was at 3.65 V during the CV phase of the charge process; after the relaxation, the voltage was observed at 3.38 V. As per Aurbach *et al.* [93], lithium ions migrate onto the surface of electrodes through solid electrolyte interphase. At 100% SOC, the electrolyte interphase cannot slow down this migration from highly concentrated electrodes, causing the OCV drop. This effect gets amplified when the load with low impedance is connected to the battery, causing a notable self-discharge effect. To avoid this, the power cables were disconnected every time the SOC level was reached to the required SOC level for measurement.

When the temperature was changed, OCV jumps and then it tries to stabilise. This effect is exponential in nature, which is why the test duration of the potentiometric test is long. This exponential stabilisation time can vary based on the SOC percentage, as ionic diffusion is more on extreme SOC ranges. This effect can be seen in fig. 5.1 where the stabilisation curve looks steeper at extreme SOCs compared to 50% SOC. In this study, as there were 7 set points through which the battery was supposed to be cycled (12 hrs test duration), there might not be enough time to reach a perfectly stable OCV value. Which is why many previous researchers used multiple days of readings for a single SOC set point, used correction factors, or used a threshold of 1 mV/h ($0.23 \mu\text{V/s}$) variation in OCV to deem if the voltage is stabilised or not.

For this reason, the derivation of voltage with respect to time was taken into account and was scaled at microvolt level. If the dV/dt was lower than $0.2 \mu\text{V/s}$, the voltage would be considered stable. Fig. 5.2 shows that even if the voltage curves are steep, the change in voltage with respect to time is very small.

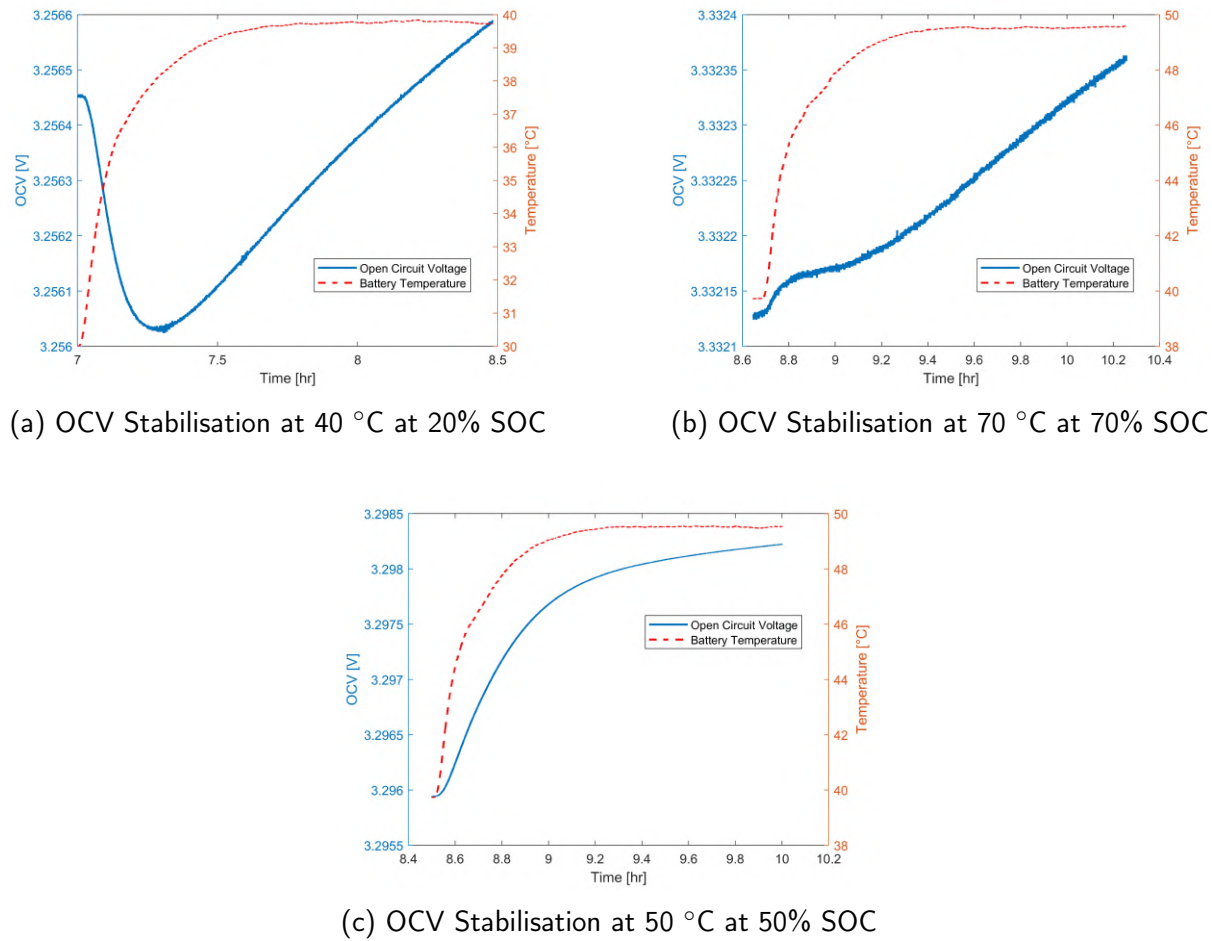


Figure 5.1: OCV Stabilisation for observed during experiment for 1 and $\frac{1}{2}$ hrs of set point

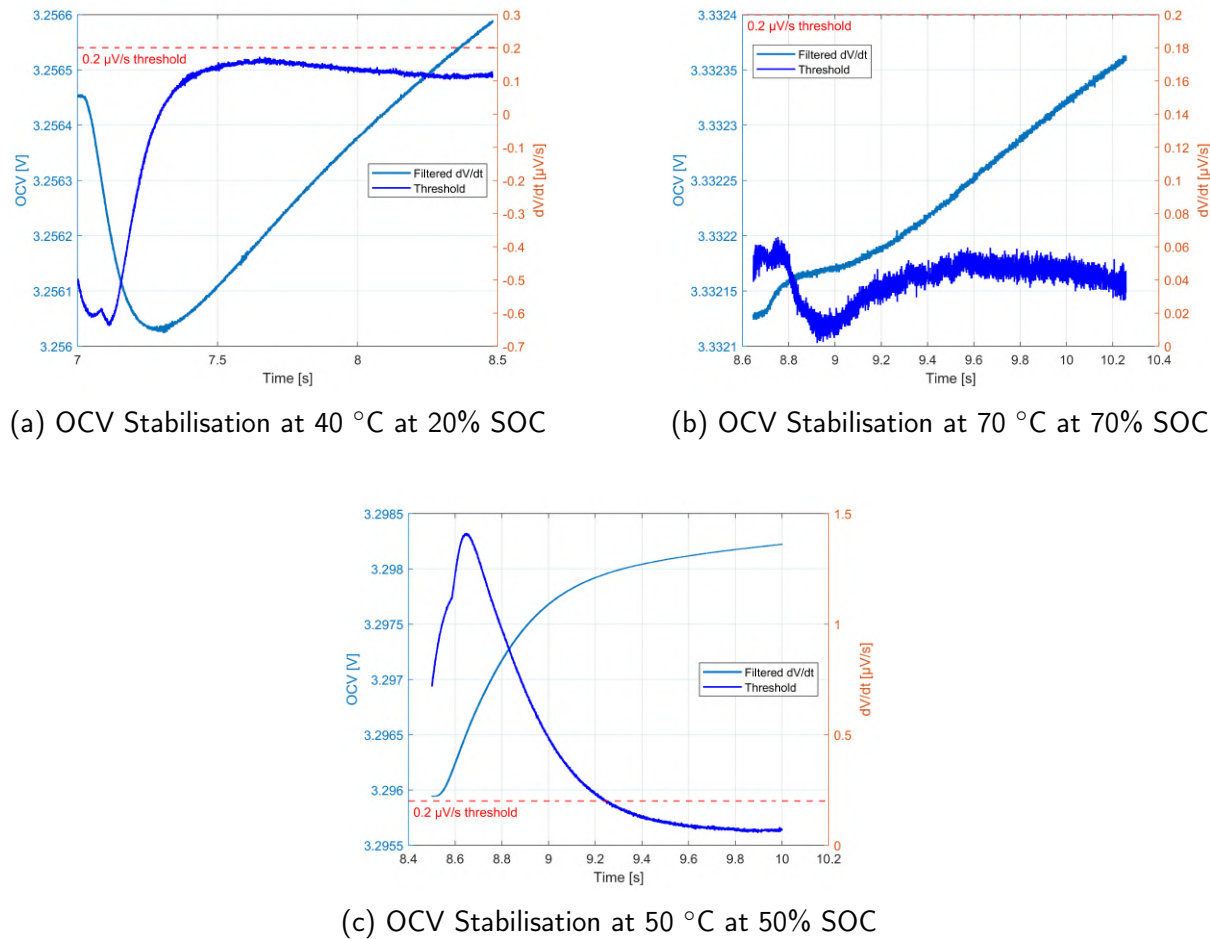


Figure 5.2: OCV Stabilisation for observed during experiment for 1 and $\frac{1}{2}$ hrs of set point along with dV/dt

Once the data was recorded, the OCV can be divided into temperature ranges. The average of the last 30 min of data for each temperature segment (between 10-50 °C) was taken as the corresponding OCV value for that particular OCV and temperature. And the Weighted Linear Least Squares method was used to estimate the slope of the voltage-temperature curve, which gives the EHC of the cell at that particular SOC level. EHC values for all the SOC points along with uncertainties can be seen in table 5.1.

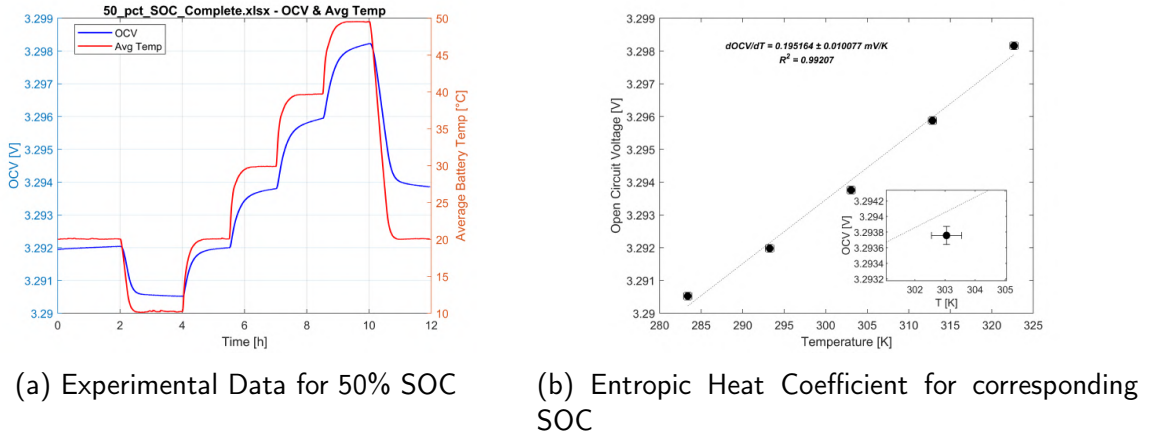


Figure 5.3: Result for 50% SOC

SOC (%)	0	10	20	30	40	50	60	70	80	90	100
EHC (mV/K)	-0.29	-0.04	0.00	-0.03	0.24	0.20	0.16	0.01	0.05	0.03	0.13
Uncertainty (\pm mV/k)	0.0219	0.0108	0.0075	0.0022	0.0168	0.0101	0.0034	0.0013	0.0052	0.0025	0.0036
Relative Uncertainty (%)	7.53	26.60	404.53	6.72	7.01	5.16	2.13	9.77	9.71	7.31	2.77

Table 5.1: Entropic Heat Coefficient with respective SOC range and Uncertainties.

It can be seen that the uncertainty percentage is higher at 20 °C and 10 °C. This is because the change in the voltage with respect to time is very low, which is why at 20 °C, the EHC is 0. Closer the value to 0, more will be the uncertainty in EHC measurement as the variation is not seen. Fig.5.4 it can be observed that the maximum deviation observed was hardly 1.8 mV and 0.5 mV for 10% and 20% SOC respectively, whereas for 50% SOC (fig 5.3b), was 8.5 mV.

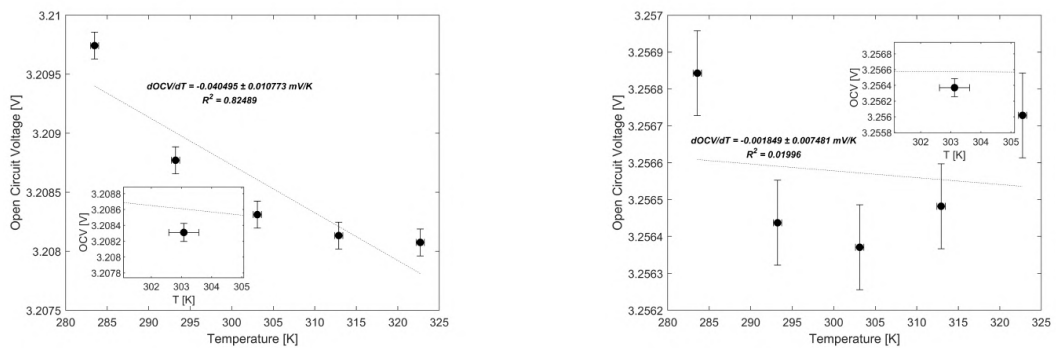


Figure 5.4: EHC for 10% and 20% SOC

To ensure the results are accurate enough, some SOC levels were tested again. The test was repeated for 70%, 50%, and 20% SOC, respectively, and the current discharge rate was set to a 0.5 C rate. This affected the test slightly as the higher C-rates' usable capacity drops due to an increase in voltage sag. Though it was only done once and the C-rate was different for a quick sanity check, it is not perfect repeatability proof. The repeatable data can be seen in table 5.2. It shows the similar EHC values; though the C rate was high, the corresponding SOC level might be slightly off, though it is good enough for a sanity check as there is no publication on the LF105 cell which provides OCV-SOC or EHC data that can be compared.

SOC (%)	20	50	70
EHC (mV/K)	-0.02	0.16	0.01
Uncertainty	0.010	0.004	0.002
Relative Uncertainty (%)	57.01	2.64	20.08

Table 5.2: Entropic Heat Coefficient with respective SOC range and Uncertainties for repeated test.

Even if the data was not available for validation of results, the results can be checked with different cells such as 26650 or 18650 cells with similar composition. It was observed in the fig. 5.5 that the EHC followed a similar trend as the other cells, validating the data with the help of Williams *et al.* dataset [69]. The obtained OCV values and EHC values will be used in modelling the real-time equivalent circuit model simulation. Fig 5.6 shows OCV as a function of SOC for various temperatures.

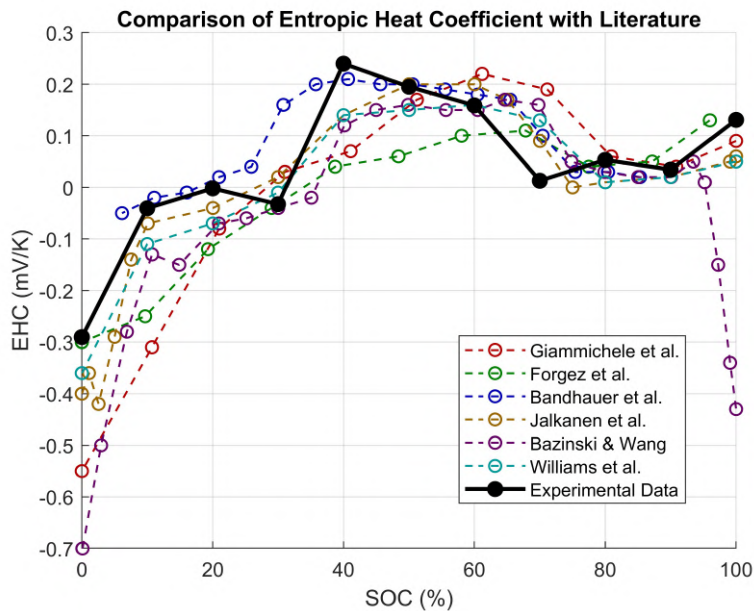
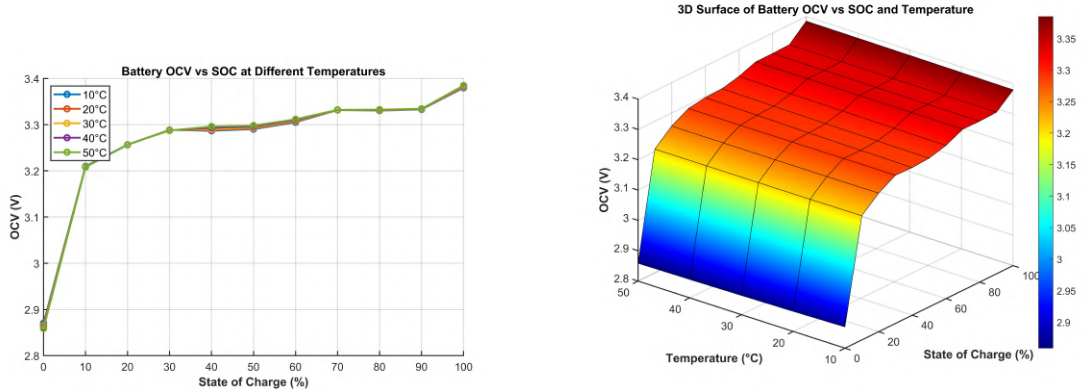


Figure 5.5: Comparison of EHC obtained with Prominent Studies



(a) OCV-SOC curve for different temperatures (b) OCV as the function of SOC and Temperature

Figure 5.6: OCV representation in terms of SOC and Temperature

5.2 Discussion

The experimental results are revealing of the entropic heat coefficient (EHC) reaction of the LF105 lithium-iron-phosphate (LFP) cell across states of charge (SOC) and temperature. The EHC values obtained by measurement, ranging from -0.29 mV/K at 0% SOC to 0.24 mV/K at 40% SOC, exhibit a characteristic trend with SOC in agreement with the principles of thermodynamics governing lithium-ion intercalation reactions. Positive EHC values are observed for an endothermic change in entropy upon discharge that serves to cool the cell, while negative values of the EHC suggest exothermic behavior, warming the cell. Such SOC-sensitive polarity is consistent with the structural phase changes and lithium ordering/disordering in the LFP cathode, where entropy effects are most pronounced at intermediate SOC since disorder is higher.

The EHC trend, with the maximum at 40-50% SOC and sloping towards zero or a mild negativity on both sides, is in agreement with the outcomes of comparable studies of LFP-based cells, e.g., 26650 or 18650 types in Figure 5.5. For instance, the EHC transition from negative towards positive near low SOC and a gradual decline towards higher SOC agree with entropy-controlled processes as described by Bazinski et al. [92] and others. This verification confirms the reproducibility of the potentiometric method used since no direct literature values are available for the LF105 cell. The OCV stabilization activation dynamics seen and the self-discharge phenomena also supplement models like those formulated by Aurbach et al. [93], in which solid electrolyte interphase (SEI) layer influences ion migration and voltage degradation, particularly under high SOC. Measurement uncertainties in EHC are much higher for SOC values where the coefficient is close to zero (e.g., 404.53% at 20% SOC) as a result of very slight voltage sensitivity to temperature (as low as 0.5 mV across the range). This sensitivity highlights a limitation of weighted linear least squares fitting when signal-to-noise is poor augmented by the short 12-hour test duration per SOC setpoint. Use of a 0.2 μ V/s dV/dt criterion reduced partial stabilization but might allow small biases against multi-day protocols used in earlier studies. Replicated tests at 20%, 50%, and 70% SOC, albeit at a higher 0.5 C-rate, yielded EHC values with satisfactory agreement (e.g., 0.16 mV/K vs. 0.20 mV/K at 50% SOC), including method reproducibility in the face of small capacity offsets due to voltage sag. These findings translate to real-world use to electric vehicle and battery energy storage thermal management systems (BTMS) for electric vehicles. Accurate EHC data enable

improved modeling of reversible heat generation, up to 20-30% of total heat in an LFP cell at modest load. Including SOC-dependent EHC in simulation can optimize cooling strategy with maximum efficiency, particularly at mid-SOC where entropic cooling occurs, increasing cycle life by reducing thermal gradients. Nevertheless, there are still restrictions: single-cell targeting precludes generalizability to pack-level behavior, where inter-cell heterogeneity and ageing can exacerbate differences. Disconnection of power cables to avoid self-discharge, even if successful, is not a typical continuous operating condition. Long-term studies would have to be pursued with aged cells, to get more robust model which can handle multi-cycle repetitions under constant C-rates would also quantify variability, with possible standardized EHC databases for future LFP variants.

Chapter 6

Battery Model Setup in MATLAB

Currently, the single-cell battery model, along with a natural convection thermal system, is completed. After careful analysis from Chapter 2 it was decided to go with the first-order Thevenin model.

As the model was planned to be developed such that it is compatible with the HIL system, the following model settings were used:

Parameters	Selected Settings
Solver Type	Fixed
Solver	discrete (no continuous states)
Time Step	0.001 (s)

Table 6.1: Model Settings used for Simulation

Time step of 1 ms was used as the vehicle's Electronic Control Unit (ECU) HIL needs to provide ECU a realistic environment for simulation which has to be discrete and cyclic [94]. Simulation end time can be decided based on the C rate of the battery; for initial simulation, it was assumed to be 1C thus the current drawn (I) was 105 A for 1 hr for the current battery. On HIL, the physical controllers are connected to verify them before connecting to the real systems, which can help in understanding if the control strategy works or the controller works as expected [95].

6.1 SOC Estimation and OCV Calculation

As the Thevenin model is being used, model needs to calculate OCV, R_0 , R_1 , and C_1 to calculate terminal voltage. We know that OCV is related to the temperature of the cell and the SOC of the cell at any given time [96], thus we can say,

$$f(OCV) = f(SOC, T) \quad (6.1)$$

Thus, to calculate the OCV we need the relation between the SOC and temperature of the cell. In the model, 2-D lookup table was used with experimental data to identify the OCV at any given SOC or temperature. Logic can be seen in fig. 6.1.

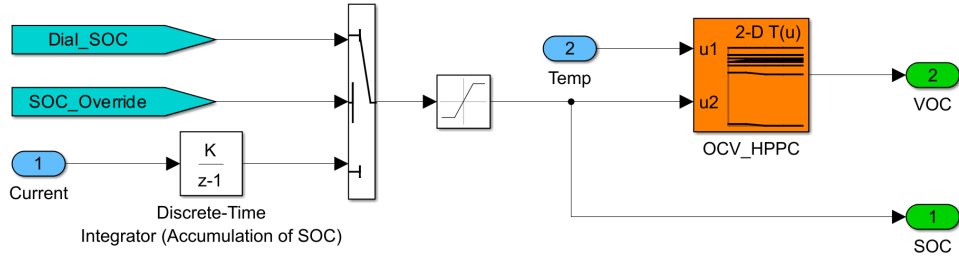


Figure 6.1: Logic to calculate OCV

Logic for SOC calculation was developed based on equation 2.12, and as the equation was generalized, it had to be discretized to calculate SOC dynamically based on Time Step. So the equation 2.12 was modified as follows,

$$SOC_{new} = SOC_{prev} - \int_{T_0}^T \frac{I \cdot Ts}{C_h \cdot 36} \quad (6.2)$$

SOC is achieved in percentage and Ts indicates time step and integral limit T indicates total simulation time, and a -ve sign indicates discharging of the battery.

6.2 Terminal Voltage Calculation

Even if the HPPC test was not performed, the model for voltage estimation was developed using equation 2.16. Though the data to fill in the model were not available, model was given provision to utilize lookup tables for R_0 , R_1 , and C_1 (fig. 6.2); thus, equation 2.16 was modified to get equation 6.3. Derivation for equation 6.3 can be referred to in Appendix A2. The modification was necessary as the simulation will be running in discrete time, so signals had to be discretised.

$$V = V_{OCV} - IR_0 - \left(V_{c,old} \left(1 - \frac{Ts}{R_1 C_1} \right) + \frac{Ts}{C_1} \cdot \frac{I_{new} + I_{old}}{2} \right) \quad (6.3)$$

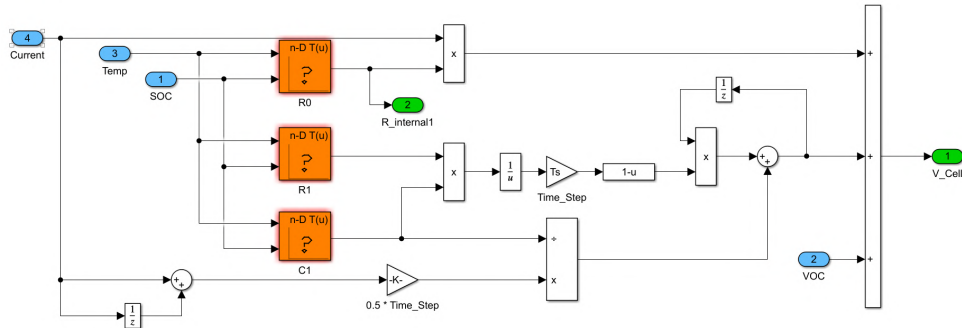


Figure 6.2: Terminal Voltage Calculation

In fig. 6.2, it can be seen that the Add block with the +ve symbol compensates for the -ve discharge current.

6.3 Heat Generated By Battery

Equation 2.7 says that the total heat generated by the battery is caused due to the internal resistance of the battery and partially due to reversible entropy heat generation. But when the model is connected to HIL, there will be inputs to the model (in this case Current) from the sensors via controller [95]. The current controller has too much noise which will need to be filtered before use. Though noise can be reduced, it will still persist and will transfer that noise into the heat estimation model. But the voltage sensors and resistance sensors have low noise which was seen in section 4.2.2. Equation 2.7 can be modified in the voltage and resistance dependent equation by using Ohm's law, making $I = V/R$. Modified heat generation equation can be seen below.

$$Q_{batt} = \frac{(V - V_{OCV})^2}{R_0} + T \frac{\partial V_{OCV}}{\partial T} \left(\frac{V - V_{OCV}}{R} \right) \quad (6.4)$$

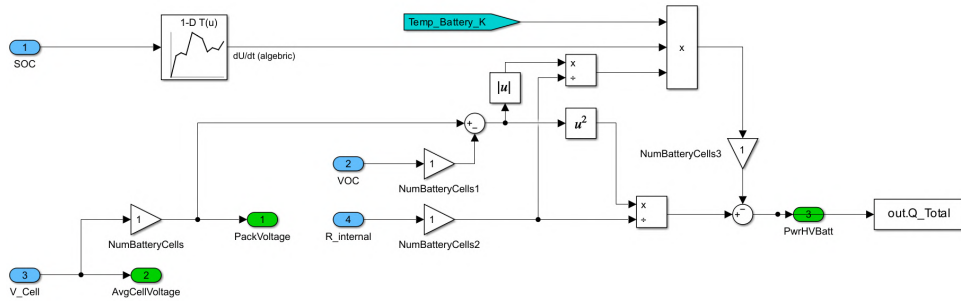


Figure 6.3: Power Heat Loss Calculation

In fig. 6.3, it can be seen that currently the number of cells is kept as 1, and as the model is expanded, the number of cells will be set accordingly.

6.4 Heat Extracted by Lumped Model

For a simple scenario test case, a natural convection model was generated. Equation 2.18 was directly used as h_{forced} term will not be used. As for the equation 2.17, if discretized, becomes,

$$Q_{generated} - Q_{extracted} = mC_p \frac{T_{new} - T_{old}}{T_s} \quad (6.5)$$

Rearranging and utilizing equation 2.18 and equation, we get

$$T_{new} = T_{old} + T_s \left(\frac{Q_{generated} - (h_{convection} A (T_{new} - T_{old}))}{mC_p} \right) \quad (6.6)$$

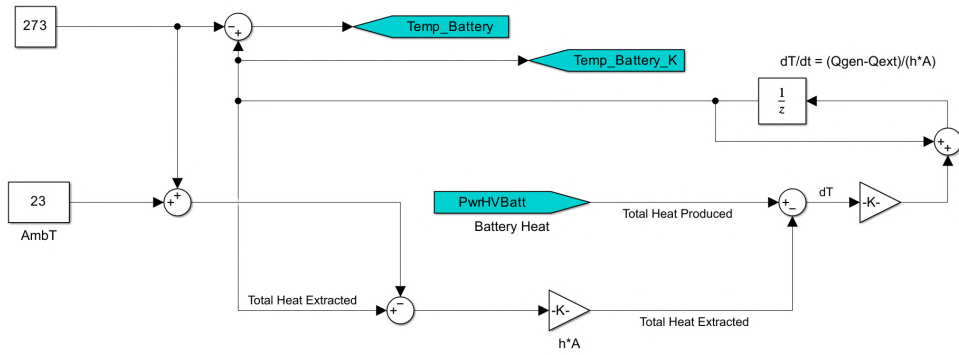


Figure 6.4: Simple Lumped Thermal System

Future version with liquid cooling would have a closed-loop system, thus would consist of a heat exchanger and pump to incorporate dynamic behavior, which is difficult to produce in a CFD environment. Schematics for such a model can be seen in fig.6.5.

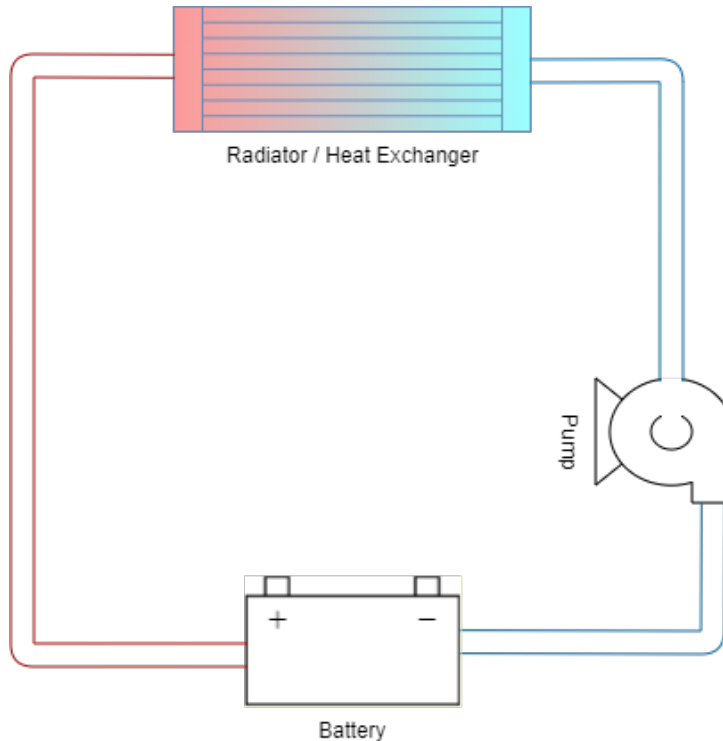


Figure 6.5: Thermal Schematics for BMS

Chapter 7

Simulation Results & Discussion

7.1 Heat Generation Model Simulation

Even if the voltage estimation model is not available, the heat generated by the battery can be simulated with data recorded during charge and discharge tests. With the same rig setup, (the pump was placed after the heat exchanger for the dynamic test), the immersed battery was charged and discharged at a 0.5 C-rate with the chiller set at 20 °C.

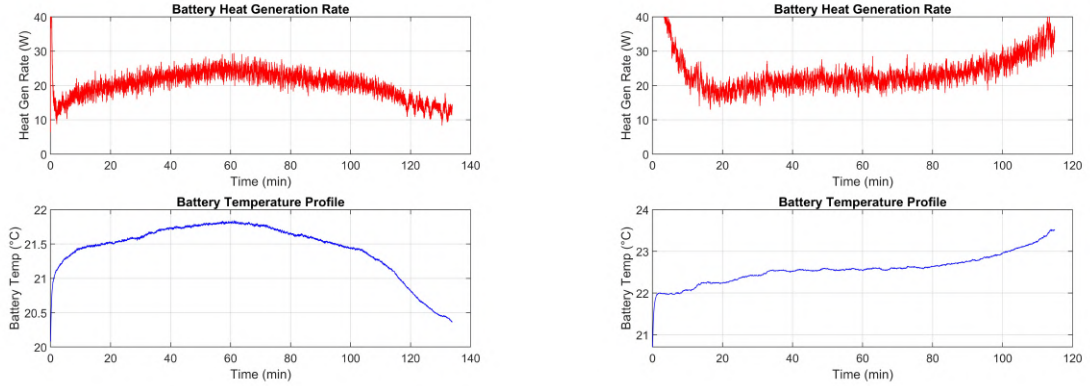
The heat generated can be estimated by determining $Q_{carried}$, which is the heat carried by the moving fluid. But this will not provide an accurate heat generation rate as battery temperature will vary slightly. Thus Q_{stored} will be represented as the heat which the coolant failed to carry. Therefore the total heat carried will be given as,

$$Q_{battery} = Q_{stored} + Q_{carried}$$

Both terms can be represented as,

$$Q_{stored} = m_{batt} C_{p,batt} \frac{dT_{batt}}{dt}$$
$$Q_{carried} = \dot{m}_{fluid} C_{p,fluid} \Delta T_{fluid}$$

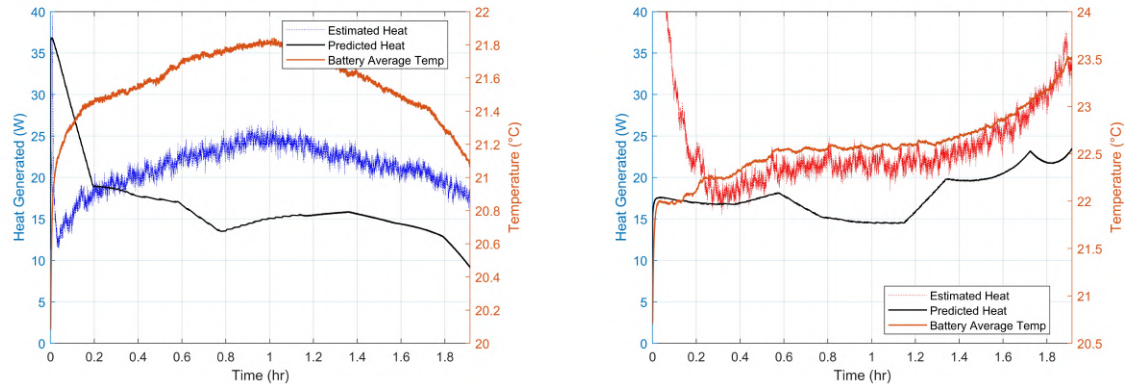
The mass and heat carrying capacity of the battery and coolant are used as provided by the manufacturer, and the mass flow rate was taken from experimental data. Heat generation of the battery can be seen in 7.1 which shows heat generated by the battery and average temperature change in the battery.



(a) Heat Generated by the Battery during Charge Phase (b) Heat Generated by the Battery during Discharge Phase

Figure 7.1: Heat Generated by the Battery

The experimentally obtained Current, Voltage, and Temperature were fed into the model, and the heat generation was estimated via equation 6.4 from the model. With these sets of inputs and using OCV and EHC parameters derived previously, the model was set to predict the heat generation of the battery. A comparison can be seen in the fig. 7.2



(a) Heat Predicted by the Battery during Charge Phase (b) Heat Predicted by the Battery during Discharge Phase

Figure 7.2: Heat Generated by the Battery

The predicted heat for discharge (fig. 7.2b) gives a good approximation of the heat produced by the battery. Whereas the heat predicted during charging is slightly under. This is because in the battery, resistance is not simply just a product of voltage and current value (which was done here as battery resistance data is not available), but it also has to do with its behaviour of ions during the change in SOC values. Thus, the lack of equivalent circuit parameters makes the model less dynamic. Also, as it is just an electrothermal model, it will never be as accurate as the high-cost CFD simulations, but even with this drawback, the heat predicted is very close to experimentally predicted heat, making it a reliable model for real-world testing and experimental archives.

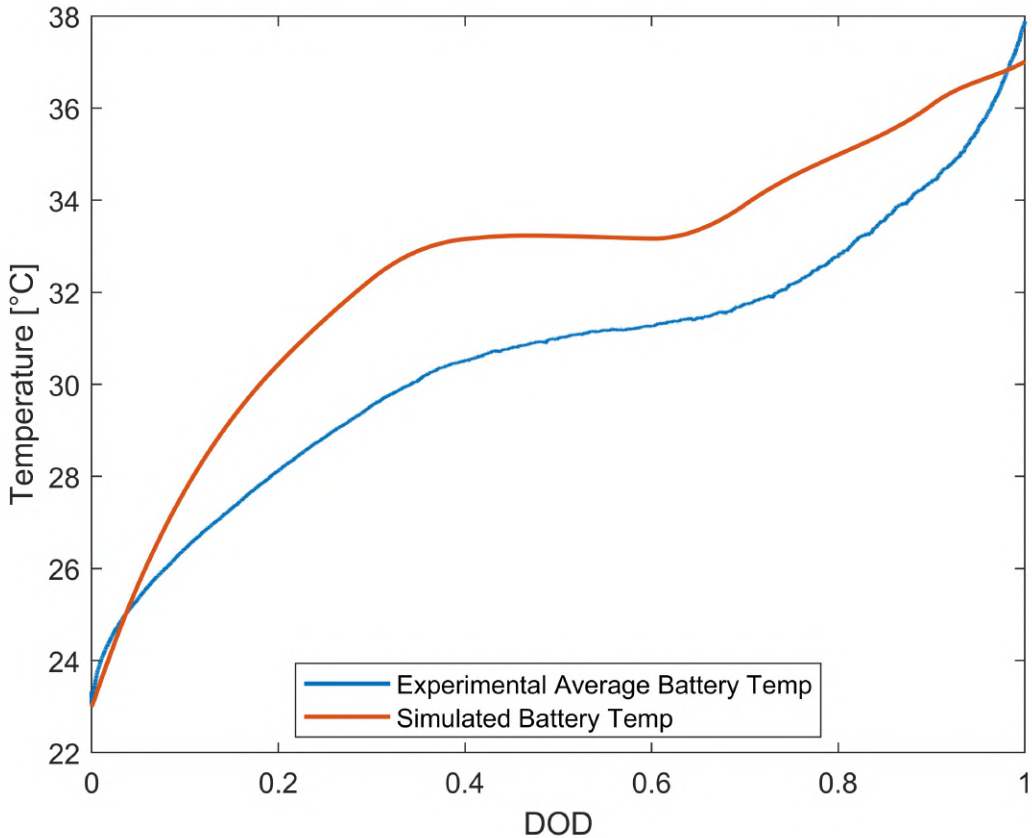


Figure 7.3: Temperature Predicted by the Model

7.2 Temperature Simulation

The battery was also discharged initially in open air to estimate the actual capacity of the battery so that the discharge time can be estimated for the Potentiometric Test. This allowed capturing the temperature data in natural convection conditions. The maximum temperature of the battery jumped to 38 °C. Fig.7.3 shows the estimated temperature. As all the parameters were available, heat transfer coefficient was assumed to be $20 \text{ W/m}^2\text{K}$ as for natural convection of air, h lies between $5-25 \text{ W/m}^2\text{K}$ [97]. The assumption was made as in actual HIL testing, not all the data is readily available, so such parameters are treated as tuning parameters.

The variation in the temperature was because the entire battery was assumed to be at constant temperature, but it is not always the case. In prismatic cells, the tabs heat more compared to the surface of the battery. The drawback is significant, but the main intention of such simulations is not to get accurate values but to see if with realistic input conditions, results will be in an acceptable and in the realistic range or not. This makes these results useful to develop the software program which will control and manage the batteries in the field.

Chapter 8

Conclusion

8.1 Conclusion

This study sought to evaluate and compare battery thermal management techniques—air cooling, indirect liquid cooling and dielectric-fluid immersion cooling—employing an integrated experimental and simulation program, and to create a compact, real-time friendly modelling workflow for MIL/HIL usage. The work combined potentiometric cell characterization of an LF105 LiFePO₄ prismatic cell (OCV and entropic heat coefficient extraction), a discrete-time Thevenin equivalent-circuit model of electrical behaviour, and a lumped thermal model to forecast cell temperature under practical electrical loading and cooling boundary conditions. Modelling and simulation were directly related to realistic HIL/MIL practicability limits (real-time time-step, modular model structure and lookup tables), and the study used available measurements wherever possible to compare model performance and identify the main causes of modelling uncertainty. It also discussed the very important role BTMS is expected to play in ensuring safety and extending performance and durability for lithium-ion batteries. For performance, thermal management reduces thermal runaway risk, preventing potentially catastrophic failures like fires or explosions.

Among the different methods analysed in this work, the most promising was immersion cooling, which gave the best thermal regulation by directly submerging the battery in a dielectric liquid. This, in return, helps minimize the internal temperature gradient of the battery pack by reducing thermal hotspots for a homogeneous temperature distribution. The liquid cooling has also given quite promising results, though the design is highly complex and, with further dependencies on channel configuration, is quite challenging. Air cooling, due to its simplicity and lower cost, became less suitable for the high-energy-density battery because of its low thermal conductivity and lesser capability to cope with extreme heat loads. And this control over the temperature gradients is precisely what is needed for the experiments which require temperature control scenarios.

Experimental characterization revealed that reversible (entropic) heat contributions are substantial to the calculation of accurate heat generation in the sample LF105 cell and must be included in thermal calculations if it is desired to accurately predict transient temperature behaviour. This qualitative result is robust across the tested measurements and the used lumped thermal simulations.

It uses a new lumped thermal modelling method for simulating heat generation and dissipation inside the battery system. It balances computational efficiency with predictive accuracy and is thus suitable for real-time applications like MIL and HIL testing. Integration of these techniques provides a good platform that exercises thermal management systems under various conditions in a simulated environment and provides insight quite valuable in the reduction of time-consuming and expensive physical prototyping. The order-one, discrete Thevenin ECM and the lumped thermal model was pragmatic fidelity-HIL-readiness trade-off: low enough in overhead to run on sub-millisecond time-steps and yet qualitatively capable of reproducing the leading electrical and thermal coupling physics given good OCV, entropic coefficient, and resistance parameters. The study also establishes a replicable MIL/HIL procedure: instrumentation and experiment setups for OCV/EHC capture, a template for lookup-table implementation of electrothermal terms, and a Simulink-compatible real-time discretisation method that may be extended once measured electrical parameters are available.

But there were few limitations to the study, the Thevenin R/C voltage model was not fully parametrized from HPPC or equivalent resistive tests within the current scope of work. Voltage-prediction accuracy is thus limited by experimental data and simply ohmic resistance. This affects any conclusion based on terminal-voltage equivalence precision (such as voltage-based heat calculations heavily reliant on polarization losses correctly resolved).

The entropic heat coefficient extraction utilized a potentiometric relaxation procedure with realistic time constraints. In SOCs in which the reversible signal is very small, the relative uncertainty is great; therefore, certain EHC data points (particularly in those cases in which the coefficient magnitude is close to instrument resolution) must be regarded as low-confidence and treated with caution in fitted models. Also, the tests were conducted at laboratory and single-cell controlled scales; pack-level phenomena, cell-to-cell variation, and forced-convection scaling were not captured herein and therefore conclusions about immersion-cooling implementation on full packs or system-level gains inferred from here require further verification.

Lumped thermal model, by definition, does not solve internal spatial gradients of more than a single representative temperature node and therefore cannot pick up strong internal heterogeneity that can arise in large cells under severe current transients or non-uniform cooling conditions. Though this was the main intention as this demands low computational power but very reliable output.

8.2 Future Goals

- To get HPPC data and complete ECM resistances and run base-case HPPC (or step-pulse) tests across SOC and temperature ranges to obtain R_0 , R_1 and C_1 lookup tables. This is the single most important test to improve voltage-prediction accuracy and consequently reduce uncertainty in ohmic and irreversible heat estimates.
- Increase confidence in low-signal SOC EHC. For SOC locations where the entropic coefficient is near instrument resolution, perform individual longer relaxation on a representative sample of SOC points to reduce relative uncertainty and to confirm sign and shape of the EHC curve. Use weighted-fitting methods to avoid over-weighting the model by high-uncertainty points.

- Scale to a small multi-cell validation. Compare immersion cooling and the lumped model on a small multi-cell assembly of 2–4 cells to observe inter-cell thermal coupling and to validate realistic packaging and flow considerations; this will also illustrate whether the lumped node per cell is sufficient for pack-level thermal management schemes.
- Implement the per-cell lumped model in a global pack model using CFD-driven convective coefficients or empirically defined h -values for different cooling schemes, and explore trade-offs between cooling power, system mass/complexity and safety factors.
- Perform selective CFD or multi-node thermal computations for a typical duty cycle to check the assumptions of the lumped model and to quantify the impact of spatial gradients on peak-to-mean temperature differentials.
- Integrate present thermal predictions with accelerated ageing tests or abuse tests to better establish how immersion cooling affects lifetime and degradation routes compared to air/liquid cooling.

8.3 Final remarks

The study contributes a straightforward experimental process to obtain the most significant thermal forecasting quantities (OCV and entropic heat), an appropriate HIL-compatible electrothermal modelling process, and experimental evidence that immersion cooling dramatically increases temperature homogeneity and reduces thermal hazard in single-cell tests. Through the completion of the known gaps—chief among them the targeted HPPC testing and repairing high-relative-uncertainty EHC points—the modelling chain may be formulated into a robust HIL asset to authorize battery thermal management plans as well as to reduce the engineering cycle on pack-level thermal designs.

Overall, this study demonstrates that measured reversible heat and a close electrothermal model are essential components of realistic, HIL-capable battery thermal simulation, and that dielectric-immersion provides a promising route to improved cell-level thermal performance. The recommendations and MIL/HIL workflow presented here represent a clear, step-by-step guide to conveying the present single-cell results to certified pack-level design alternatives and to using these results in industry test labs.

The theoretical modelling has been taken to realistic application through the development of an advanced simulation tool that can be used for optimizing battery thermal performance. While placing electrochemical and thermal considerations at the design level, therefore setting ground rules for scalable, efficient, and safe battery systems, it indeed puts certain milestones that have been important or will support, in one way or another, the entire world while moving towards Sustainable Transportation and Renewable Energy Systems toward a Green and Sustainable future.

The insight and methodologies gained from it represent the leap in battery technology change toward meeting the demands for safer, more efficient, and long-lasting energy storage in the electro-physicized world.

Bibliography

- [1] F. Un-Noor, S. Padmanaban, L. Mihet-Popa, M. Mollah, and E. Hossain, "A comprehensive study of key electric vehicle (EV) components, technologies, challenges, impacts, and future direction of development," *Energies*, vol. 10, no. 8, p. 1217, 2017. doi: 10.3390/en10081217
- [2] S. I. Spencer, Z. Fu, E. Apostolaki-Iosifidou, and T. E. Lipman, "Evaluating smart charging strategies using real-world data from optimized plugin electric vehicles," *Transportation Research Part D: Transport and Environment*, vol. 100, p. 103023, 2021. doi: 10.1016/j.trd.2021.103023
- [3] R. Matthe, L. Turner, and H. Mettlach, "VOLTEC battery system for electric vehicle with extended range," *SAE International Journal of Engines*, vol. 4, no. 1, pp. 1944–1962, 2011. doi: 10.4271/2011-01-1373
- [4] T. M. Bandhauer, S. Garimella, and T. F. Fuller, "A critical review of thermal issues in lithium-ion batteries," *Journal of The Electrochemical Society*, vol. 158, no. 3, p. R1, 2011. doi: 10.1149/1.3515880
- [5] D. Shylla, A. Jain, P. Shah, and R. Sekhar, "Model in loop (MIL), software in loop (SIL) and hardware in loop (HIL) testing in MBD," in *2023 4th IEEE Global Conference for Advancement in Technology (GCAT)*, 2023. doi: 10.1109/GCAT59970.2023.10353323 pp. 1–6.
- [6] F. Mihalič, M. Truntič, and A. Hren, "Hardware-in-the-loop simulations: A historical overview of engineering challenges," *Electronics*, vol. 11, no. 15, p. 2462, 2022. doi: 10.3390/electronics11152462
- [7] B. R. Mudhivarthi, V. Saini, A. Dodia, P. Shah, and R. Sekhar, "Model based design in automotive open system architecture," in *2023 7th International Conference on Intelligent Computing and Control Systems (ICICCS)*. IEEE, 2023. doi: 10.1109/ICI-CCS56967.2023.10142603. ISBN 979-8-3503-9725-3 pp. 1211–1216.
- [8] C. Lin and L. Zhang, "Hardware-in-the-loop simulation and its application in electric vehicle development," in *2008 IEEE Vehicle Power and Propulsion Conference*. IEEE, 2008. doi: 10.1109/VPPC.2008.4677560. ISBN 978-1-4244-1848-0 pp. 1–6.
- [9] A guide to understanding battery specifications. [Online]. Available: https://web.mit.edu/evt/summary_battery_specifications.pdf
- [10] Battery cell, module or pack. what's the difference? [infographics] | automotive cells company. [Online]. Available: <https://www.acc-emotion.com/stories/battery-cell-module-or-pack-whats-difference-infographics>

- [11] C. Graf, "Cathode materials for lithium-ion batteries," in *Lithium-Ion Batteries: Basics and Applications*, R. Korthauer, Ed. Springer Berlin Heidelberg, 2018, pp. 29–41. ISBN 978-3-662-53069-6 978-3-662-53071-9
- [12] S. Leuthner, "Lithium-ion battery overview," in *Lithium-Ion Batteries: Basics and Applications*, R. Korthauer, Ed. Springer Berlin Heidelberg, 2018, pp. 13–19. ISBN 978-3-662-53069-6 978-3-662-53071-9
- [13] Q. Wang, B. Jiang, B. Li, and Y. Yan, "A critical review of thermal management models and solutions of lithium-ion batteries for the development of pure electric vehicles," *Renewable and Sustainable Energy Reviews*, vol. 64, pp. 106–128, 2016. doi: 10.1016/j.rser.2016.05.033
- [14] L. Saw, Y. Ye, and A. Tay, "Electrochemical–thermal analysis of 18650 lithium iron phosphate cell," *Energy Conversion and Management*, vol. 75, pp. 162–174, 2013. doi: 10.1016/j.enconman.2013.05.040
- [15] M.-K. Tran, A. DaCosta, A. Mevawalla, S. Panchal, and M. Fowler, "Comparative study of equivalent circuit models performance in four common lithium-ion batteries: LFP, NMC, LMO, NCA," *Batteries*, vol. 7, no. 3, p. 51, 2021. doi: 10.3390/batteries7030051
- [16] J. Chiew, C. Chin, W. Toh, Z. Gao, J. Jia, and C. Zhang, "A pseudo three-dimensional electrochemical-thermal model of a cylindrical LiFePO₄/graphite battery," *Applied Thermal Engineering*, vol. 147, pp. 450–463, 2019. doi: 10.1016/j.applthermaleng.2018.10.108
- [17] X. Zhang, "Thermal analysis of a cylindrical lithium-ion battery," *Electrochimica Acta*, vol. 56, no. 3, pp. 1246–1255, 2011. doi: 10.1016/j.electacta.2010.10.054
- [18] D. P. Finegan, E. Darcy, M. Keyser, B. Tjaden, T. M. M. Heenan, R. Jervis, J. J. Bailey, R. Malik, N. T. Vo, O. V. Magdysyuk, R. Atwood, M. Drakopoulos, M. DiMichiel, A. Rack, G. Hinds, D. J. L. Brett, and P. R. Shearing, "Characterising thermal runaway within lithium-ion cells by inducing and monitoring internal short circuits," *Energy & Environmental Science*, vol. 10, no. 6, pp. 1377–1388, 2017. doi: 10.1039/C7EE00385D
- [19] P. Nur Halimah, S. Rahardian, B. A. Budiman, Faculty of Mechanical and Aerospace Engineering, Institut Teknologi Bandung, Indonesia, National Center for Sustainable Transportation Technology, Indonesia, Faculty of Mechanical and Aerospace Engineering, Institut Teknologi Bandung, Indonesia, and National Center for Sustainable Transportation Technology, Indonesia, "Battery cells for electric vehicles," *International Journal of Sustainable Transportation Technology*, vol. 2, no. 2, pp. 54–57, 2019. doi: 10.31427/IJSTT.2019.2.2.3
- [20] F. J. Günter and N. Wassiliadis, "State of the art of lithium-ion pouch cells in automotive applications: Cell teardown and characterization," *Journal of The Electrochemical Society*, vol. 169, no. 3, p. 030515, 2022. doi: 10.1149/1945-7111/ac4e11
- [21] C. Borgnakke and R. E. Sonntag, *Fundamentals of thermodynamics*, 8th ed. Wiley, 2013. ISBN 978-1-118-13199-2
- [22] G. Liu, M. Ouyang, L. Lu, J. Li, and X. Han, "Analysis of the heat generation of lithium-ion battery during charging and discharging considering different influencing factors,"

- Journal of Thermal Analysis and Calorimetry*, vol. 116, no. 2, pp. 1001–1010, 2014. doi: 10.1007/s10973-013-3599-9 Publisher: Springer Science and Business Media LLC.
- [23] S. W. Baek, K. E. Wyckoff, D. M. Butts, J. Bienz, A. Likitchatchawankun, M. B. Preefer, M. Frajnkovič, B. S. Dunn, R. Seshadri, and L. Pilon, “Operando calorimetry informs the origin of rapid rate performance in microwave-prepared TiNb₂O₇ electrodes,” *Journal of Power Sources*, vol. 490, p. 229537, 2021. doi: 10.1016/j.jpowsour.2021.229537
- [24] D. Ren, X. Feng, L. Lu, M. Ouyang, S. Zheng, J. Li, and X. He, “An electrochemical-thermal coupled overcharge-to-thermal-runaway model for lithium ion battery,” *Journal of Power Sources*, vol. 364, pp. 328–340, 2017. doi: 10.1016/j.jpowsour.2017.08.035
- [25] L. Giammichele, V. D’Alessandro, M. Falone, and R. Ricci, “Thermal behaviour assessment and electrical characterisation of a cylindrical lithium-ion battery using infrared thermography,” *Applied Thermal Engineering*, vol. 205, p. 117974, 2022. doi: 10.1016/j.applthermaleng.2021.117974
- [26] C. Forgez, D. Vinh Do, G. Friedrich, M. Morcrette, and C. Delacourt, “Thermal modeling of a cylindrical LiFePO₄/graphite lithium-ion battery,” *Journal of Power Sources*, vol. 195, no. 9, pp. 2961–2968, 2010. doi: 10.1016/j.jpowsour.2009.10.105
- [27] K. E. Thomas and J. Newman, “Thermal modeling of porous insertion electrodes,” *Journal of The Electrochemical Society*, vol. 150, no. 2, p. A176, 2003. doi: 10.1149/1.1531194
- [28] H. Du, Y. Wang, Y. Kang, Y. Zhao, Y. Tian, X. Wang, Y. Tan, Z. Liang, J. Wozny, T. Li, D. Ren, L. Wang, X. He, P. Xiao, E. Mao, N. Tavajohi, F. Kang, and B. Li, “Side reactions/changes in lithium-ion batteries: Mechanisms and strategies for creating safer and better batteries,” *Advanced Materials*, vol. 36, no. 29, 2024. doi: 10.1002/adma.202401482 Publisher: Wiley.
- [29] D. Bernardi, E. Pawlikowski, and J. Newman, “A general energy balance for battery systems,” *Journal of The Electrochemical Society*, vol. 132, no. 1, p. 5, 1985. doi: 10.1149/1.2113792 Publisher: The Electrochemical Society, Inc.
- [30] L. Li, X. Ju, X. Zhou, Y. Peng, Z. Zhou, B. Cao, and L. Yang, “Experimental study on thermal runaway process of 18650 lithium-ion battery under different discharge currents,” *Materials*, vol. 14, no. 16, p. 4740, 2021. doi: 10.3390/ma14164740
- [31] C. Bibin, M. Vijayaram, V. Suriya, R. Sai Ganesh, and S. Soundarraj, “A review on thermal issues in li-ion battery and recent advancements in battery thermal management system,” *Materials Today: Proceedings*, vol. 33, pp. 116–128, 2020. doi: 10.1016/j.matpr.2020.03.317
- [32] X. Feng, M. Ouyang, X. Liu, L. Lu, Y. Xia, and X. He, “Thermal runaway mechanism of lithium ion battery for electric vehicles: A review,” *Energy Storage Materials*, vol. 10, pp. 246–267, 2018. doi: 10.1016/j.ensm.2017.05.013
- [33] I. Lalinde, A. Berrueta, J. José Valera, J. Arza, P. Sanchis, and A. Ursúa, “Perspective chapter: Thermal runaway in lithium-ion batteries,” in *Lithium Batteries - Recent Advances and Emerging Topics*, A. Berrueta and A. Ursúa, Eds. IntechOpen, 2024. ISBN 978-1-80355-474-7 978-1-80355-475-4

- [34] J. D. Patel and R. S. Patel, "Theoretical modelling of heat generation in batteries of electric vehicles for various operating environments," *IOP Conference Series: Materials Science and Engineering*, vol. 1146, no. 1, p. 012027, 2021. doi: 10.1088/1757-899x/1146/1/012027
- [35] P. R. Tete, M. M. Gupta, and S. S. Joshi, "Developments in battery thermal management systems for electric vehicles: A technical review," *Journal of Energy Storage*, vol. 35, p. 102255, 2021. doi: 10.1016/j.est.2021.102255
- [36] A. Olabi, H. M. Maghrabie, O. H. K. Adhari, E. T. Sayed, B. A. Yousef, T. Salameh, M. Kamil, and M. A. Abdelkareem, "Battery thermal management systems: Recent progress and challenges," *International Journal of Thermofluids*, vol. 15, p. 100171, 2022. doi: 10.1016/j.ijft.2022.100171
- [37] X. Xiaoming, J. Fu, H. Jiang, and R. He, "Research on the heat dissipation performance of lithium-ion cell with different operating conditions: Heat dissipation performance of lithium-ion cell," *International Journal of Energy Research*, vol. 41, no. 11, pp. 1642–1654, 2017. doi: 10.1002/er.3682
- [38] C. Roe, X. Feng, G. White, R. Li, H. Wang, X. Rui, C. Li, F. Zhang, V. Null, M. Parkes, Y. Patel, Y. Wang, H. Wang, M. Ouyang, G. Offer, and B. Wu, "Immersion cooling for lithium-ion batteries – a review," *Journal of Power Sources*, vol. 525, p. 231094, 2022. doi: 10.1016/j.jpowsour.2022.231094
- [39] W. Wu, S. Wang, W. Wu, K. Chen, S. Hong, and Y. Lai, "A critical review of battery thermal performance and liquid based battery thermal management," *Energy Conversion and Management*, vol. 182, pp. 262–281, 2019. doi: 10.1016/j.enconman.2018.12.051
- [40] X. Yu, Z. Lu, L. Zhang, L. Wei, X. Cui, and L. Jin, "Experimental study on transient thermal characteristics of stagger-arranged lithium-ion battery pack with air cooling strategy," *International Journal of Heat and Mass Transfer*, vol. 143, p. 118576, 2019. doi: 10.1016/j.ijheatmasstransfer.2019.118576
- [41] S. K. Mohammadian and Y. Zhang, "Cumulative effects of using pin fin heat sink and porous metal foam on thermal management of lithium-ion batteries," *Applied Thermal Engineering*, vol. 118, pp. 375–384, 2017. doi: 10.1016/j.applthermaleng.2017.02.121
- [42] S. Wang, K. Li, Y. Tian, J. Wang, Y. Wu, and S. Ji, "Improved thermal performance of a large laminated lithium-ion power battery by reciprocating air flow," *Applied Thermal Engineering*, vol. 152, pp. 445–454, 2019. doi: 10.1016/j.applthermaleng.2019.02.061
- [43] G. Xia, L. Cao, and G. Bi, "A review on battery thermal management in electric vehicle application," *Journal of Power Sources*, vol. 367, pp. 90–105, 2017. doi: 10.1016/j.jpowsour.2017.09.046
- [44] A. K. Thakur, R. Prabakaran, M. Elkadeem, S. W. Sharshir, M. Arıcı, C. Wang, W. Zhao, J.-Y. Hwang, and R. Saidur, "A state of art review and future viewpoint on advance cooling techniques for lithium-ion battery system of electric vehicles," *Journal of Energy Storage*, vol. 32, p. 101771, 2020. doi: 10.1016/j.est.2020.101771
- [45] J. Zhao, Z. Rao, and Y. Li, "Thermal performance of mini-channel liquid cooled cylinder based battery thermal management for cylindrical lithium-ion power bat-

- tery," *Energy Conversion and Management*, vol. 103, pp. 157–165, 2015. doi: 10.1016/j.enconman.2015.06.056
- [46] L. Sheng, L. Su, H. Zhang, K. Li, Y. Fang, W. Ye, and Y. Fang, "Numerical investigation on a lithium ion battery thermal management utilizing a serpentine-channel liquid cooling plate exchanger," *International Journal of Heat and Mass Transfer*, vol. 141, pp. 658–668, 2019. doi: 10.1016/j.ijheatmasstransfer.2019.07.033
- [47] M. Bernagozzi, A. Georgoulas, N. Miché, and M. Marengo, "Heat pipes in battery thermal management systems for electric vehicles: A critical review," *Applied Thermal Engineering*, vol. 219, p. 119495, 2023. doi: 10.1016/j.applthermaleng.2022.119495
- [48] D. M. Weragoda, G. Tian, A. Burkabayev, K.-H. Lo, and T. Zhang, "A comprehensive review on heat pipe based battery thermal management systems," *Applied Thermal Engineering*, vol. 224, p. 120070, 2023. doi: 10.1016/j.applthermaleng.2023.120070
- [49] N. Campagna, V. Castiglia, R. Miceli, R. A. Mastromauro, C. Spataro, M. Trapanese, and F. Viola, "Battery models for battery powered applications: A comparative study," *Energies*, vol. 13, no. 16, p. 4085, 2020. doi: 10.3390/en13164085
- [50] J. P. Horton, J. W. Chapman, and M. K. Leader, "Comparison and application of battery modeling methods for conceptual electric aircraft," in *AIAA Aviation Forum*, American Institute of Aeronautics and Astronautics. Las Vegas, NV: NASA Glenn Research Center, July 2024, nASA Technical Report ID: 20240007449. [Online]. Available: <https://ntrs.nasa.gov/citations/20240007449>
- [51] R. R. Thakkar, "Electrical equivalent circuit models of lithium-ion battery," in *Management and Applications of Energy Storage Devices*, K. E. Okedu, Ed. IntechOpen, 2022. ISBN 978-1-83969-644-2 978-1-83969-645-9
- [52] Equivalent-circuit cell models. [Online]. Available: <http://mocha-java.uccs.edu/ECE5710/ECE5710-Notes02.pdf>
- [53] W. Xu, J. Xu, J. Lang, and X. Yan, "A multi-timescale estimator for lithium-ion battery state of charge and state of energy estimation using dual h infinity filter," *IEEE Access*, vol. 7, pp. 181 229–181 241, 2019. doi: 10.1109/ACCESS.2019.2959396
- [54] Lijun Gao, Shengyi Liu, and R. Dougal, "Dynamic lithium-ion battery model for system simulation," *IEEE Transactions on Components and Packaging Technologies*, vol. 25, no. 3, pp. 495–505, 2002. doi: 10.1109/TCAPT.2002.803653
- [55] L. Chen, M. Zhang, Y. Ding, S. Wu, Y. Li, G. Liang, H. Li, and H. Pan, "Estimation the internal resistance of lithium-ion-battery using a multi-factor dynamic internal resistance model with an error compensation strategy," *Energy Reports*, vol. 7, pp. 3050–3059, 2021. doi: 10.1016/j.egyr.2021.05.027
- [56] B. R. Kim, T. N. Nguyen, and C. W. Park, "Cooling performance of thermal management system for lithium-ion batteries using two types of cold plate: Experiment and MATLAB/simulink-simscape simulation," *International Communications in Heat and Mass Transfer*, vol. 145, p. 106816, 2023. doi: 10.1016/j.icheatmasstransfer.2023.106816
- [57] Simscape. [Online]. Available: <https://www.mathworks.com/products/simscape.html>

- [58] Simulink - simulation and model-based design. [Online]. Available: <https://www.mathworks.com/products/simulink.html>
- [59] B. Shabani and M. Biju, "Theoretical modelling methods for thermal management of batteries," *Energies*, vol. 8, no. 9, pp. 10153–10177, 2015. doi: 10.3390/en80910153 Publisher: MDPI AG.
- [60] A. P. Ramallo-González, M. E. Eames, and D. A. Coley, "Lumped parameter models for building thermal modelling: An analytic approach to simplifying complex multi-layered constructions," *Energy and Buildings*, vol. 60, pp. 174–184, 2013. doi: 10.1016/j.enbuild.2013.01.014 Publisher: Elsevier BV.
- [61] M. Kaliaperumal and R. K. Chidambaram, "Thermal management of lithium-ion battery pack using equivalent circuit model," *Vehicles*, vol. 6, no. 3, pp. 1200–1215, 2024. doi: 10.3390/vehicles6030057
- [62] F. P. Incropera and F. P. Incropera, Eds., *Fundamentals of heat and mass transfer*, 6th ed. John Wiley, 2007. ISBN 978-0-471-45728-2
- [63] School of Aeronautics and Astronautics, University of Electronic Science and Technology of China, Chengdu 611731, China, Q. Zhong, B. Huang, J. Ma, and H. Li, "Experimental study on relationship between SOC and OCV of lithium-ion batteries," *International Journal of Smart Grid and Clean Energy*, 2014. doi: 10.12720/sgce.3.2.149-153
- [64] Q.-Q. Yu, R. Xiong, L.-Y. Wang, and C. Lin, "A comparative study on open circuit voltage models for lithium-ion batteries," *Chinese Journal of Mechanical Engineering*, vol. 31, no. 1, p. 65, 2018. doi: 10.1186/s10033-018-0268-8
- [65] SOC-OCV test for lithium batteries. [Online]. Available: https://www.everexceed.com/blog/soc-ocv-test-for-lithium-batteries_b55
- [66] Z. Geng, J. Groot, and T. Thiringer, "A time- and cost-effective method for entropic coefficient determination of a large commercial battery cell," *IEEE Transactions on Transportation Electrification*, vol. 6, no. 1, pp. 257–266, 2020. doi: 10.1109/TTE.2020.2971454
- [67] K. Jalkanen, T. Aho, and K. Vuorilehto, "Entropy change effects on the thermal behavior of a LiFePO₄ /graphite lithium-ion cell at different states of charge," *Journal of Power Sources*, vol. 243, pp. 354–360, 2013. doi: 10.1016/j.jpowsour.2013.05.199
- [68] Z. Lin, D. Wu, C. Du, and Z. Ren, "An improved potentiometric method for the measurement of entropy coefficient of lithium-ion battery based on positive adjustment," *Energy Reports*, vol. 8, pp. 54–63, 2022. doi: 10.1016/j.egyr.2022.10.109
- [69] N. Williams, B. Zelent, D. Trimble, and S. O'Shaughnessy, "Experimental determination of the entropic heat coefficient of a lithium-ion cell through immersion in a dielectric fluid," *Applied Thermal Engineering*, vol. 258, p. 124597, 2025. doi: 10.1016/j.applthermaleng.2024.124597
- [70] A. M. Ahmad, G. Thenaisie, and S.-G. Lee, "A calorimetric approach to fast entropy-variations extraction for lithium-ion batteries using optimized galvanostatic intermittent titration technique," *Journal of Power Sources Advances*, vol. 16, p. 100097, 2022. doi: 10.1016/j.powera.2022.100097

- [71] N. Damay, C. Forgez, M.-P. Bichat, and G. Friedrich, "A method for the fast estimation of a battery entropy-variation high-resolution curve – application on a commercial LiFePO₄/graphite cell," *Journal of Power Sources*, vol. 332, pp. 149–153, 2016. doi: 10.1016/j.jpowsour.2016.09.083
- [72] H. E. Perez, J. B. Siegel, X. Lin, A. G. Stefanopoulou, Y. Ding, and M. P. Castanier, "Parameterization and Validation of an Integrated Electro-Thermal Cylindrical LFP Battery Model," in *Volume 3: Renewable Energy Systems; Robotics; Robust Control; Single Track Vehicle Dynamics and Control; Stochastic Models, Control and Algorithms in Robotics; Structure Dynamics and Smart Structures;*. ASME, 2012. doi: 10.1115/DSCC2012-MOVIC2012-8782. ISBN 978-0-7918-4531-8 pp. 41–50.
- [73] R. Jackey, M. Saginaw, P. Sanghvi, J. Gazzari, T. Huria, and M. Ceraolo, "Battery Model Parameter Estimation Using a Layered Technique: An Example Using a Lithium Iron Phosphate Cell," in *SAE Technical Paper Series*, 2013. doi: 10.4271/2013-01-1547 pp. 2013–01–1547. [Online]. Available: <https://www.sae.org/content/2013-01-1547/>
- [74] What is HPPC Testing? NEWARE Technology LLC. [Online]. Available: <https://www.neware.net/news/high-power-pulse-characterization-hppc-testing/230/105.html>
- [75] British Standards Institution (BSI), *BS ISO 12405-4:2018 - Electrically propelled road vehicles – Test specification for lithium-ion battery packs and systems – Part 4: Performance testing*, British Standards Institution Std., July 2018, supersedes BS ISO 12405-1:2011 and BS ISO 12405-2:2012.
- [76] N. Ding, K. Prasad, T. T. Lie, and J. Cui, "State of Charge Estimation of a Composite Lithium-Based Battery Model Based on an Improved Extended Kalman Filter Algorithm," *Inventions*, vol. 4, no. 4, p. 66, 2019. doi: 10.3390/inventions4040066
- [77] H. Zhang, C. Deng, Y. Zong, Q. Zuo, H. Guo, S. Song, and L. Jiang, "Effect of Sample Interval on the Parameter Identification Results of RC Equivalent Circuit Models of Li-ion Battery: An Investigation Based on HPPC Test Data," *Batteries*, vol. 9, no. 1, p. 1, 2022. doi: 10.3390/batteries9010001
- [78] T. Białoń, R. Niestrój, W. Skarka, and W. Korski, "HPPC Test Methodology Using LFP Battery Cell Identification Tests as an Example," *Energies*, vol. 16, no. 17, p. 6239, 2023. doi: 10.3390/en16176239
- [79] Inventec Performance Chemicals, "PROMOSOLV™ DR3 Technical Data Sheet, Version EN-3," Inventec, a brand of Dehon Group, Tech. Rep., Dec. 2021, accessed: Aug. 5, 2025. [Online]. Available: <https://www.inventec.dehon.com/wp-content/uploads/2021/12/PDS-Promosolv-DR3-EN-3.pdf>
- [80] ——, "PROMOSOLV™ DR3 – Safety Data Sheet (15 kg Container)," Inventec Performance Chemicals (via ConRo Electronics), Tech. Rep., Dec. 2021, accessed: Aug. 5, 2025. [Online]. Available: <https://www.conro.com/downloads/Manuals/Inventec-Promosolv-DR3-15KG-Container-SDS.pdf>
- [81] Polar Series Accel 500 LC Cooling/Heating Recirculating Chillers Force/Suction Pump | Buy Online. [Online]. Available: <https://www.thermofisher.com/order/catalog/product/223422100>

- [82] E. S. I. Technologies. Mag-drive pumps? What are they? What are they used for? ESI Technologies Group. [Online]. Available: <https://esitechgroup.com/knowledge-centre/what-are-mag-drive-pumps/>
- [83] EA-PSB 11000-10 2U | EA Elektro-Automatik EA-PSB 10000 Series Bench Power Supply, 0 → 1000V, 0 → 1000A, 1-Output, 3kW | RS. [Online]. Available: <https://ie.rs-online.com/web/p/bench-power-supplies/2592976>
- [84] PROMOSOLV™ DR3. Chem Solutions. [Online]. Available: <https://www.chemsolutions.it/en/product/promosolv-dr3/>
- [85] RS Components, “A70000007335203 datasheet,” <https://docs.rs-online.com/56f2/A70000007335203.pdf>, accessed: 14-Aug-2025.
- [86] NI-9213 Specifications - NI. <https://www.ni.com>. [Online]. Available: <https://www.ni.com/docs>
- [87] L. Kirkup, *Experimental Methods for Science and Engineering Students: An Introduction to the Analysis and Presentation of Data*, 2nd ed. Cambridge University Press, 2019. ISBN 978-1-108-29010-4 978-1-108-41846-1
- [88] Standard Error of the Estimate. [Online]. Available: <https://onlinestatbook.com/2/regression/accuracy.html>
- [89] Calculating uncertainties in a thermocouple calibration system. [Online]. Available: <https://www.fluke.com/en-us/learn/blog/temperature-calibration/thermocouple-app-notes-series-part-3>
- [90] J. C. for Guides in Metrology, “Evaluation of Measurement Data – guide to the expression of uncertainty in measurement (gum),” https://www.bipm.org/documents/20126/2071204/JCGM_100_2008_E.pdf, Joint Committee for Guides in Metrology (JCGM), Tech. Rep., 2008, available via BIPM.
- [91] International Organization for Standardization, “ISO/TS 28037:2010 – Determination and use of straight-line calibration functions,” International Organization for Standardization, Geneva, Switzerland, Tech. Rep., 2010, weighted linear regression with known measurement uncertainties; definitions of weights, residuals, chi-squared and parameter uncertainty.
- [92] S. J. Bazinski and X. Wang, “The influence of cell temperature on the entropic coefficient of a lithium iron phosphate (LFP) pouch cell,” *Journal of The Electrochemical Society*, vol. 161, no. 1, pp. A168–A175, 2014. doi: 10.1149/2.082401jes
- [93] D. Aurbach, “A review on new solutions, new measurements procedures and new materials for rechargeable Li batteries,” *Journal of Power Sources*, vol. 146, no. 1–2, pp. 71–78, 2005. doi: 10.1016/j.jpowsour.2005.03.151
- [94] Use case: Testing engine ECUs. [Online]. Available: https://www.dspace.com/en/pub/home/products/systems/ecutest/configuration_examples/ecus_for_combustion_engines.cfm
- [95] H. Bai, C. Liu, E. Breaz, K. Al-Haddad, and F. Gao, “A Review on the Device-Level Real-Time Simulation of Power Electronic Converters: Motivations for Improving Per-

- formance," *IEEE Industrial Electronics Magazine*, vol. 15, no. 1, pp. 12–27, Mar. 2021. doi: 10.1109/mie.2020.2989834
- [96] F. Feng, R. Lu, G. Wei, and C. Zhu, "Online estimation of model parameters and state of charge of LiFePO₄ batteries using a novel open-circuit voltage at various ambient temperatures," *Energies*, vol. 8, no. 4, pp. 2950–2976, 2015. doi: 10.3390/en8042950
- [97] 2015 SolidWorks - Convection Heat Coefficient. [Online]. Available: https://help.solidworks.com/2015/english/SolidWorks/cworks/c_convection_heat_coefficient.htm?format=P&value=

Appendix A1

Experimental Results

A1.1 Complete Results

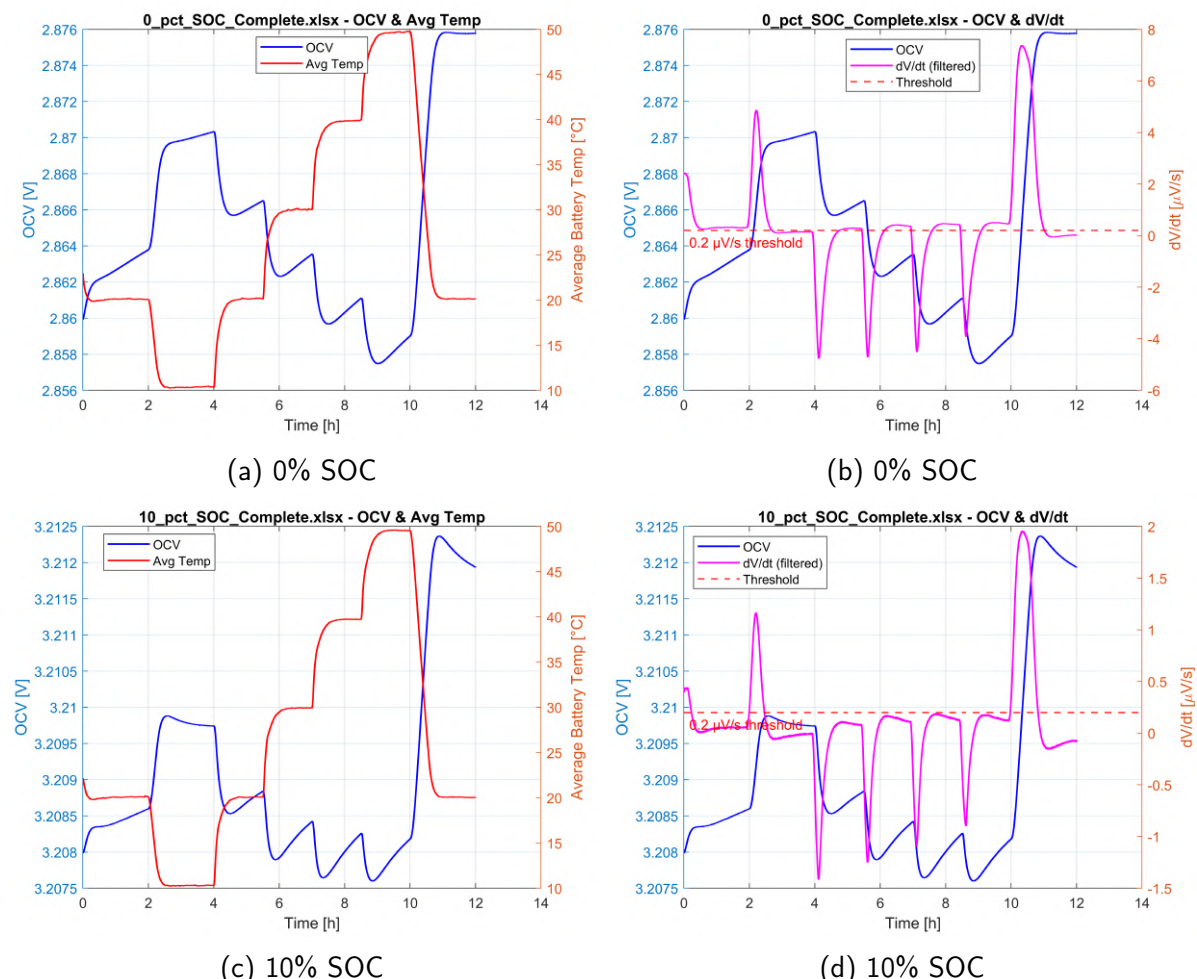


Figure A1.1: Raw Experimental Plots along with dV/dt (Part 1)

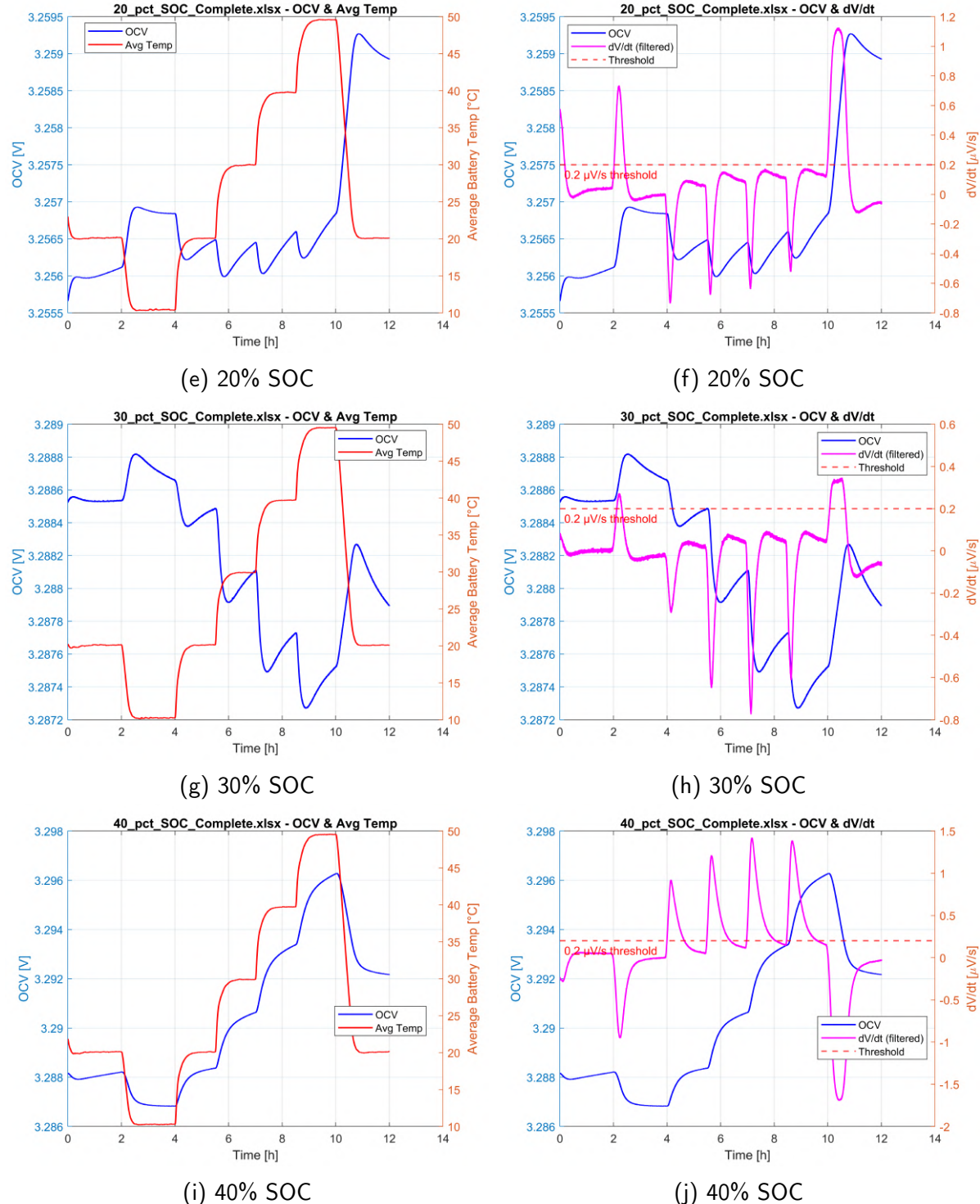


Figure A1.1: Raw Experimental Plots along with dV/dt (Part 2)

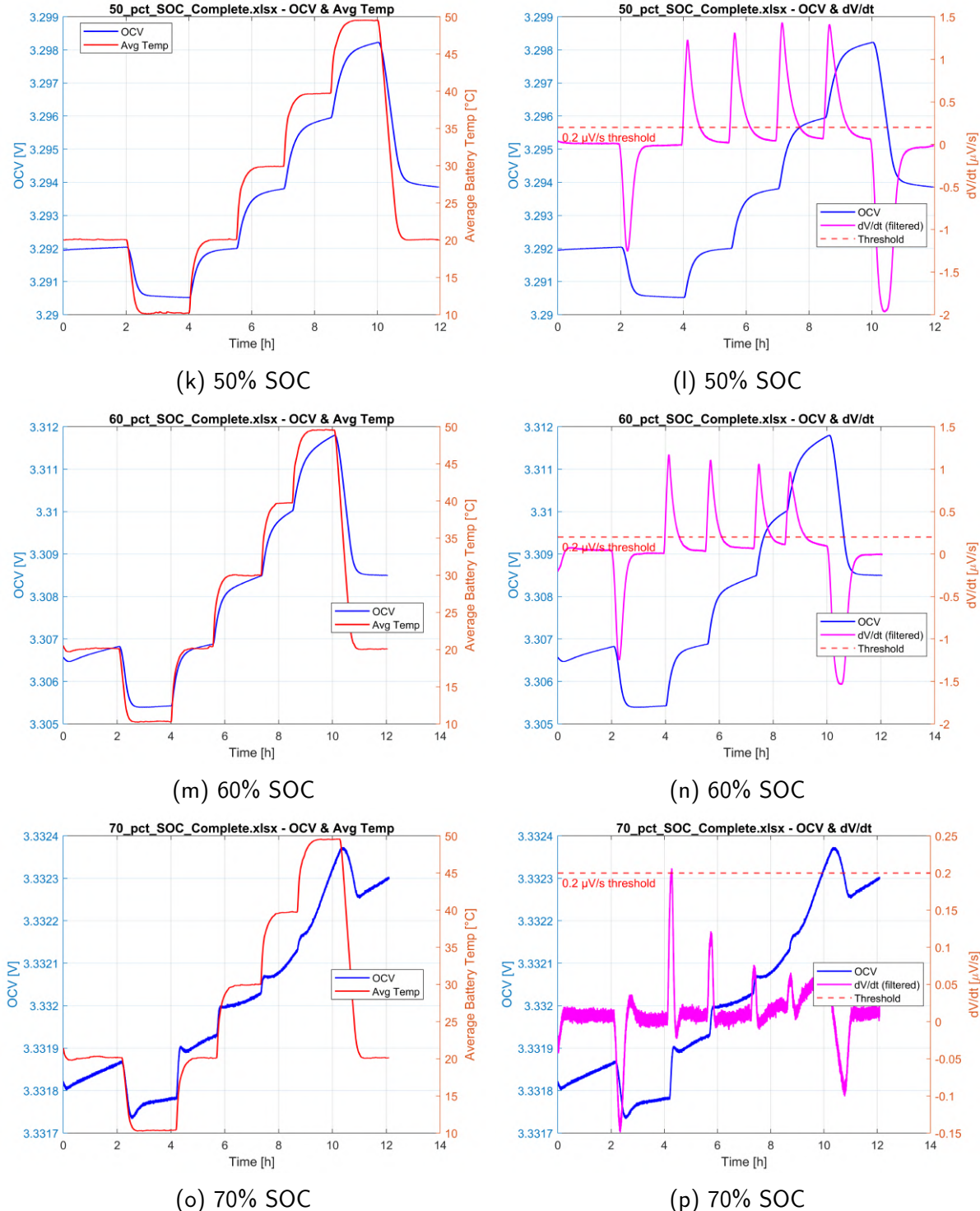


Figure A1.1: Raw Experimental Plots along with dV/dt (Part 3)

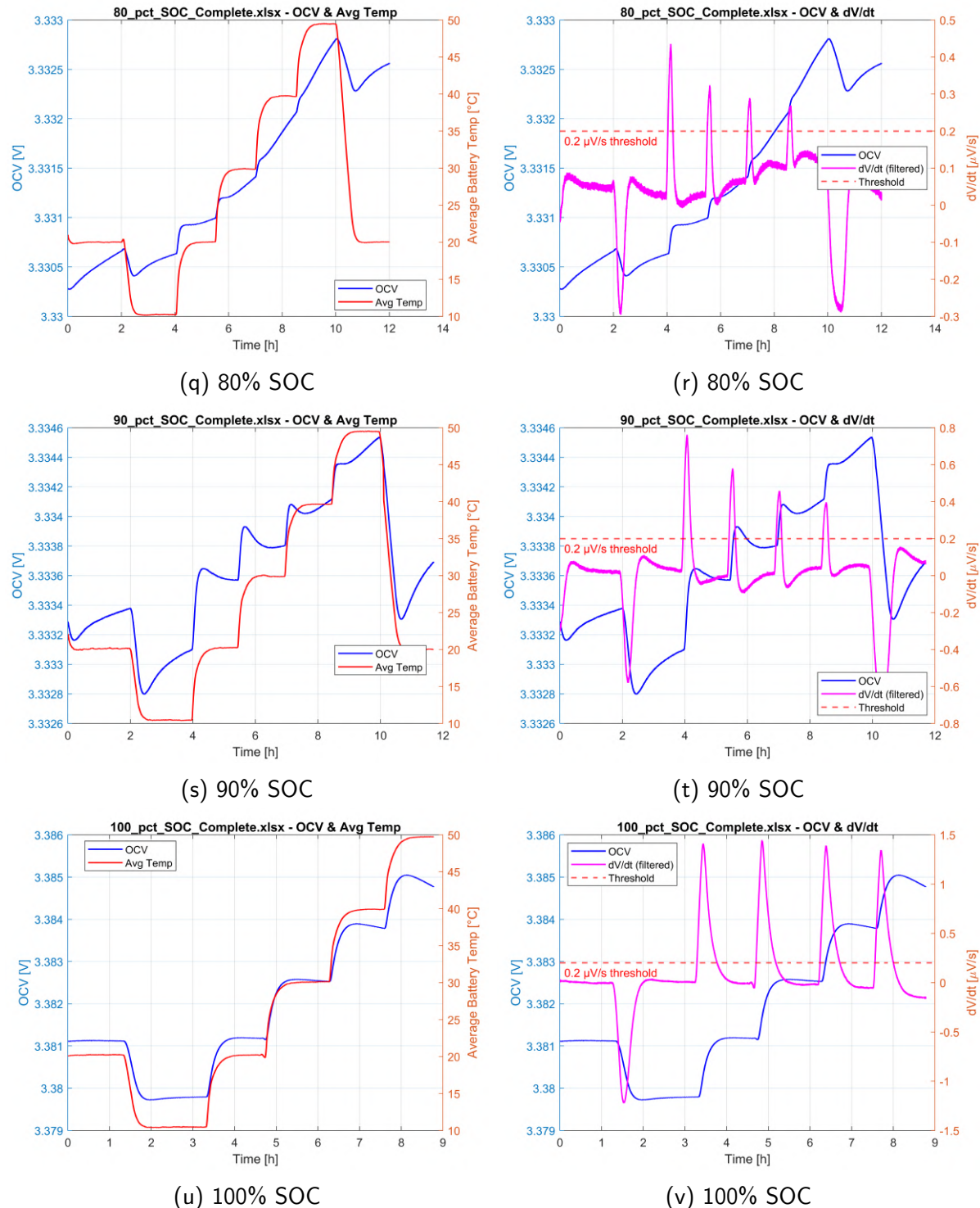


Figure A1.1: Raw Experimental Plots along with dV/dt (Final Part)

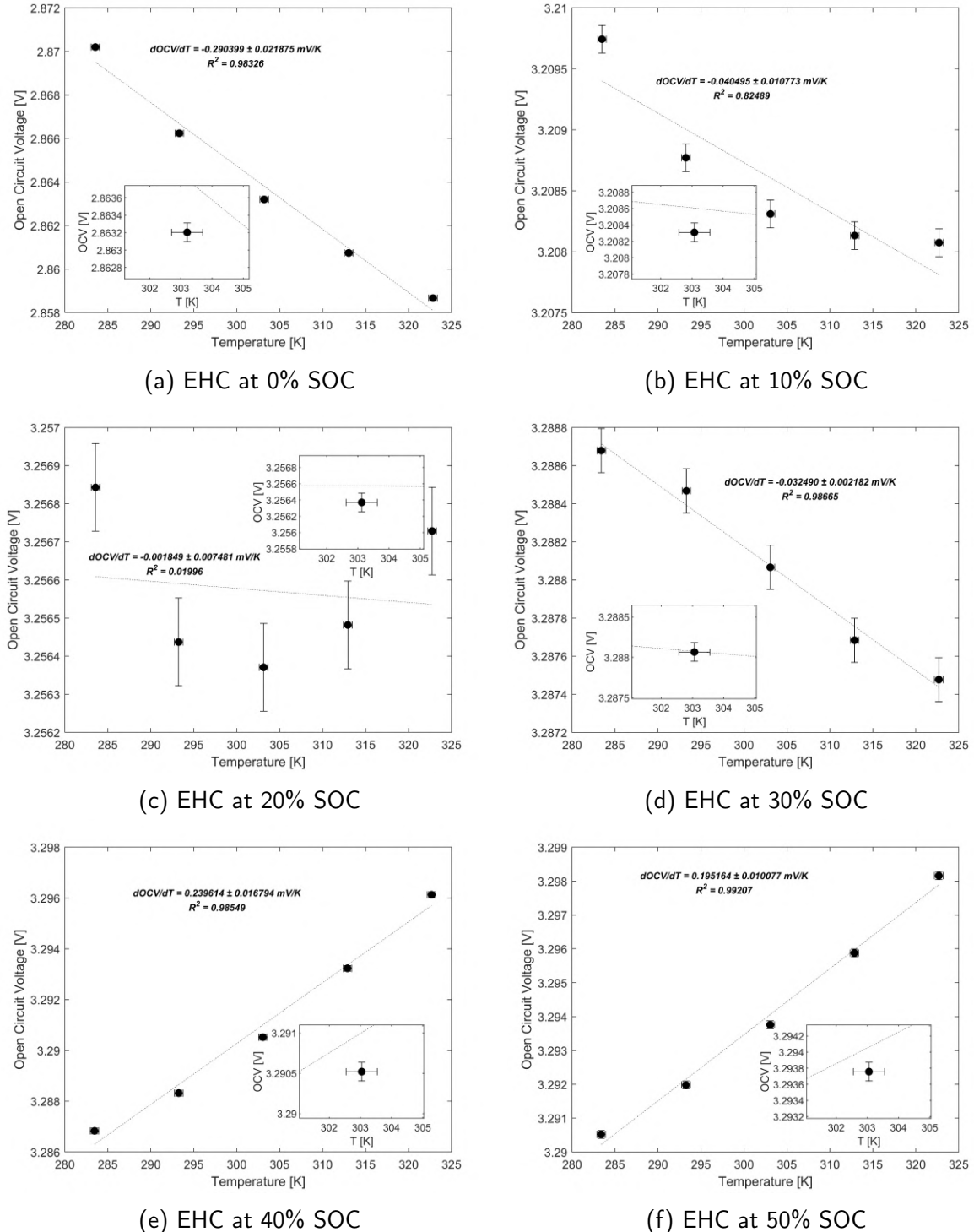


Figure A1.2: Entropic Heat Coefficient Prediction with Uncertainties (Part 1)

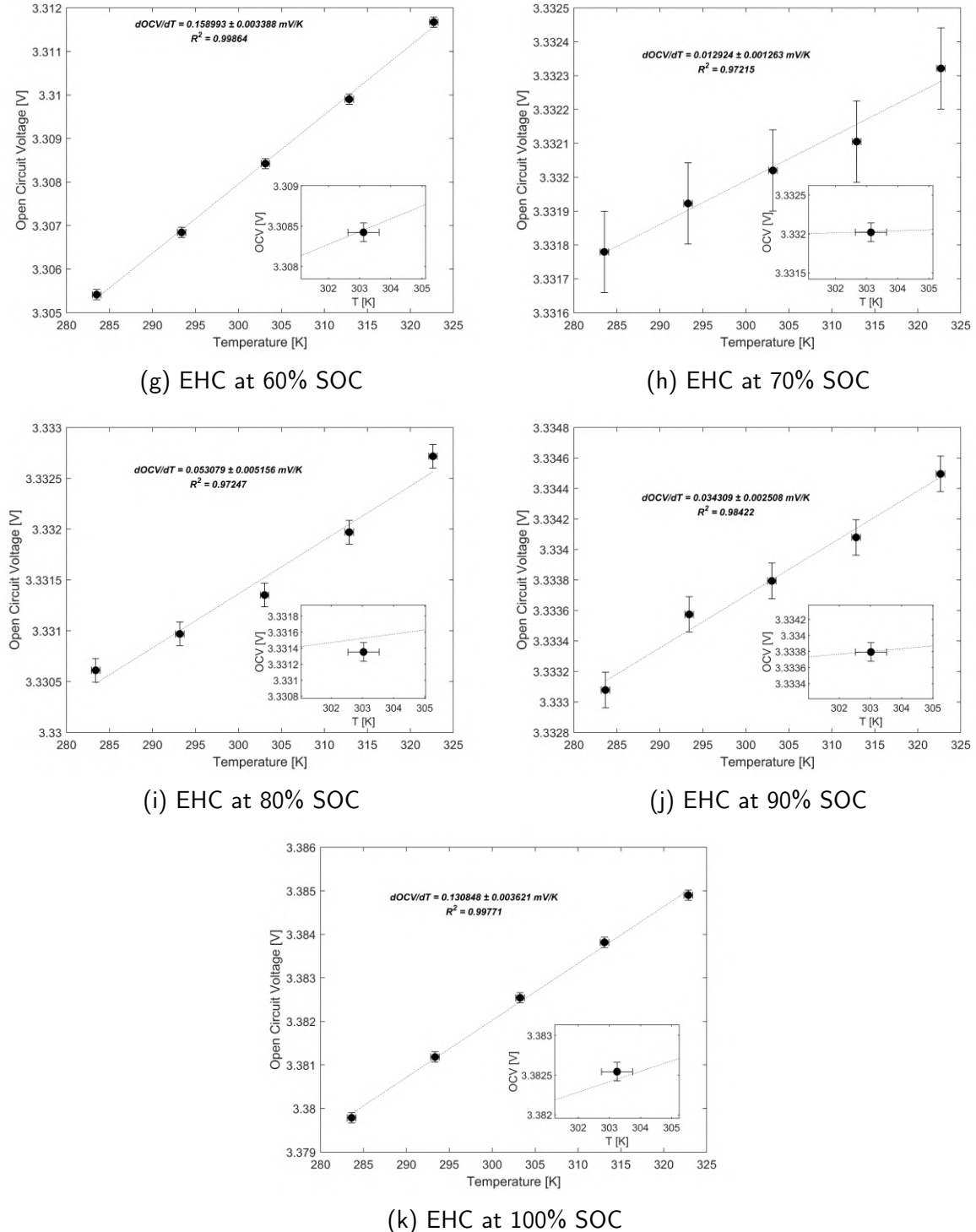


Figure A1.2: Entropic Heat Coefficient Prediction with Uncertainties (Final Part)

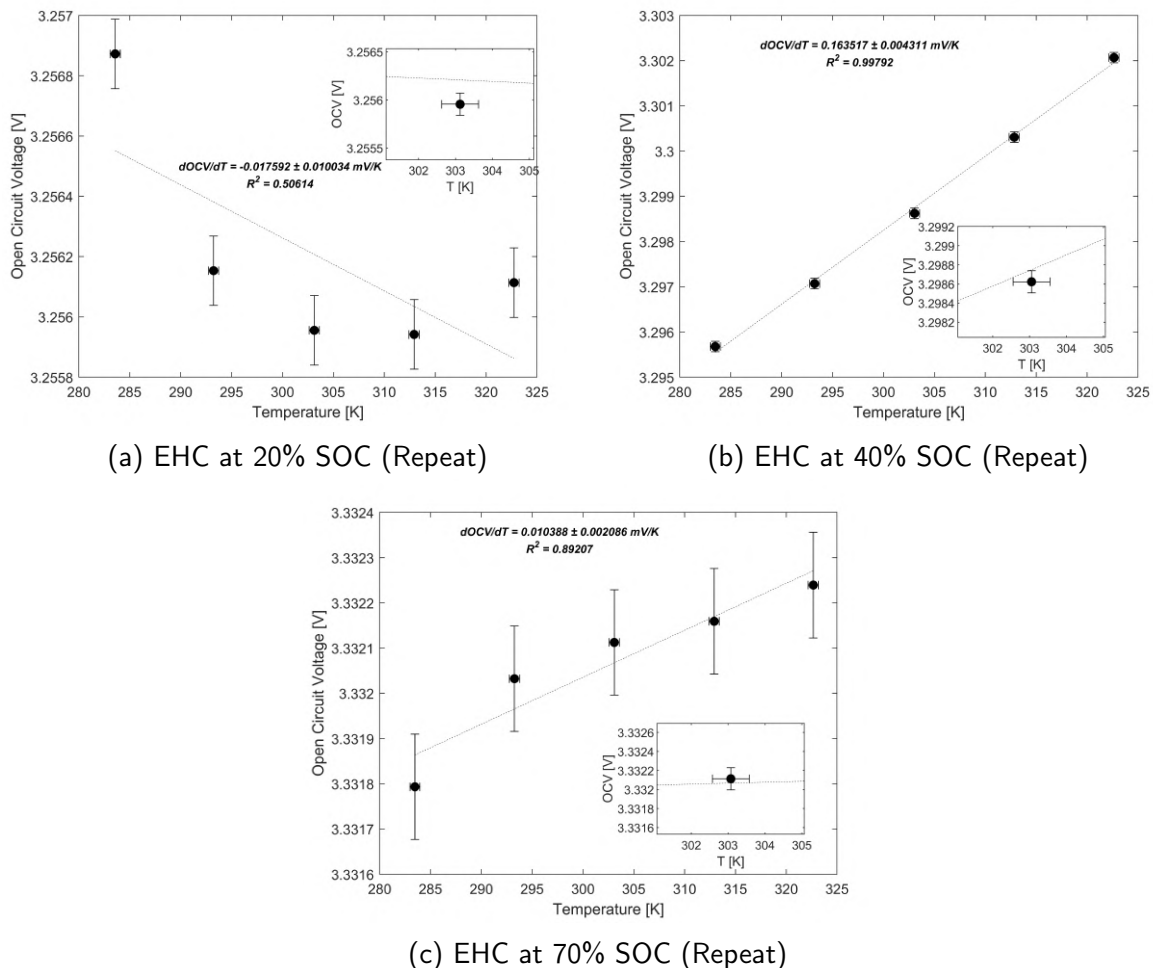


Figure A1.3: Entropic Heat Coefficient Prediction with Uncertainties for Repeated Studies

Appendix A2

Derivation for Terminal Voltage Equation

Equation 2.16 was used to develop logic to calculate the terminal voltage (V). Model utilizes lookup tables for R_0 , R_1 , and C_1 . But as equation 2.16 is expressed in terms of current, it needed to be expressed to achieve discretization. As the model has a term for current across R_1 (I_{R1}), it makes it more appropriate to utilize the value of C_1 . Thus, we can say $I_{R1} = \frac{V_{C1}}{R_1}$, making,

$$\frac{1}{R_1} \frac{dV_{C1}}{dt} = -\frac{1}{R_1 C_1} \left(\frac{V_{C1}}{R_1} - I(t) \right) \quad (\text{A2.1})$$

Solving above gives

$$\Rightarrow \frac{dV_{C1}}{dt} = \frac{I(t)}{C_1} - \frac{V_{C1}}{R_1 C_1} \quad (\text{A2.2})$$

To discretize,

$$V_{C1,new} - V_{C1,old} = -Ts \left(\frac{1}{R_1 C_1} + \frac{1}{C_1} \left(\frac{I_{new} + I_{old}}{2} \right) \right) \quad (\text{A2.3})$$

Further simplifying equation A2.3, V_{C1} can be calculated as

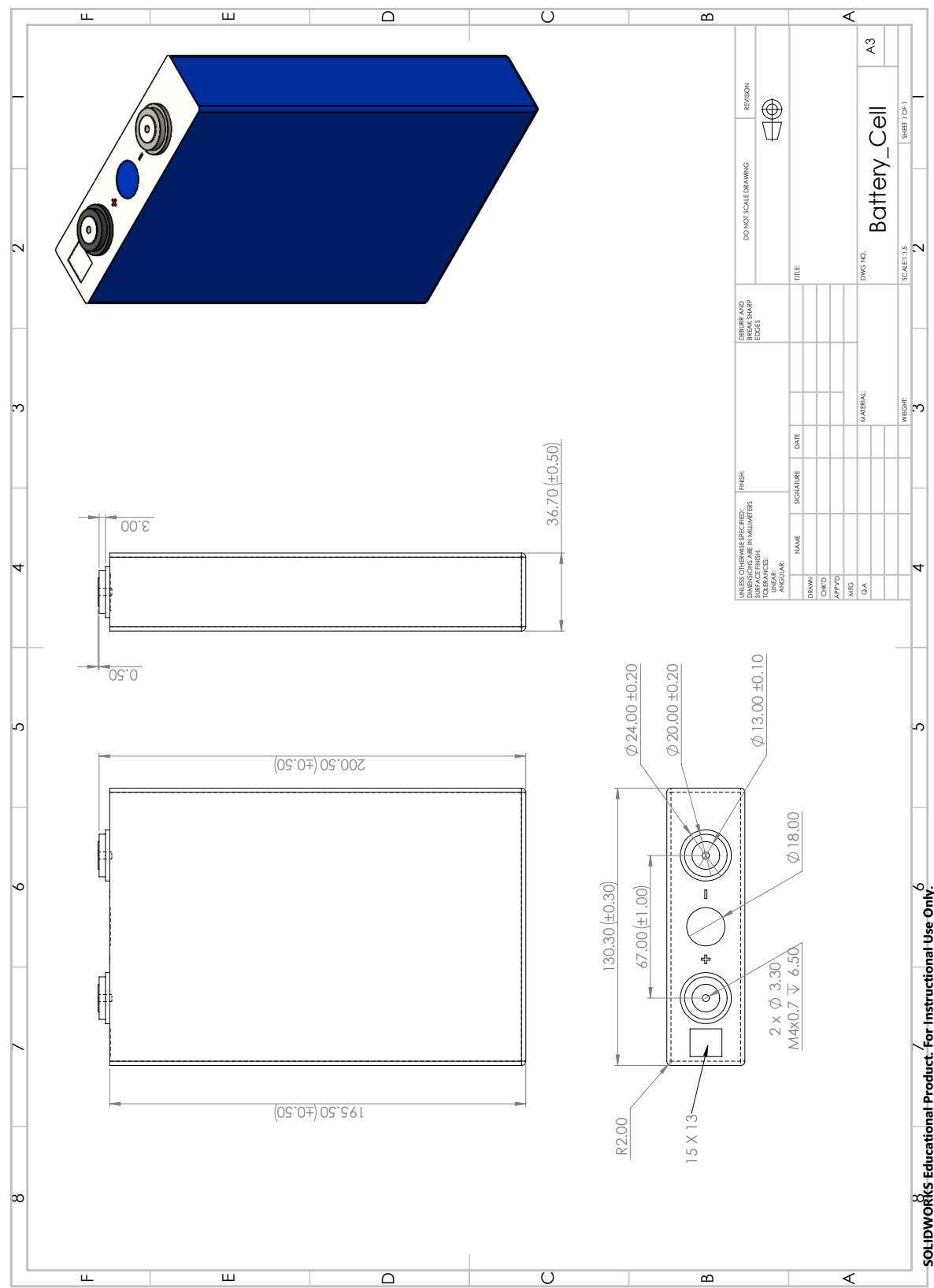
$$V_{C1,new} = V_{c,old} \left(1 - \frac{Ts}{R_1 C_1} \right) + \frac{Ts}{C_1} \cdot \frac{I_{new} + I_{old}}{2} \quad (\text{A2.4})$$

Equation 2.14 for terminal voltage becomes equation A2.5 and is used in the model (fig 6.2).

$$V = V_{OCV} - IR_0 - \left(V_{c,old} \left(1 - \frac{Ts}{R_1 C_1} \right) + \frac{Ts}{C_1} \cdot \frac{I_{new} + I_{old}}{2} \right) \quad (\text{A2.5})$$

Appendix A3

Technical Drawings

Figure A3.1: Drawing for LF105 (3.2 V 105 Ah) Prismatic LiFePO₄ Cell

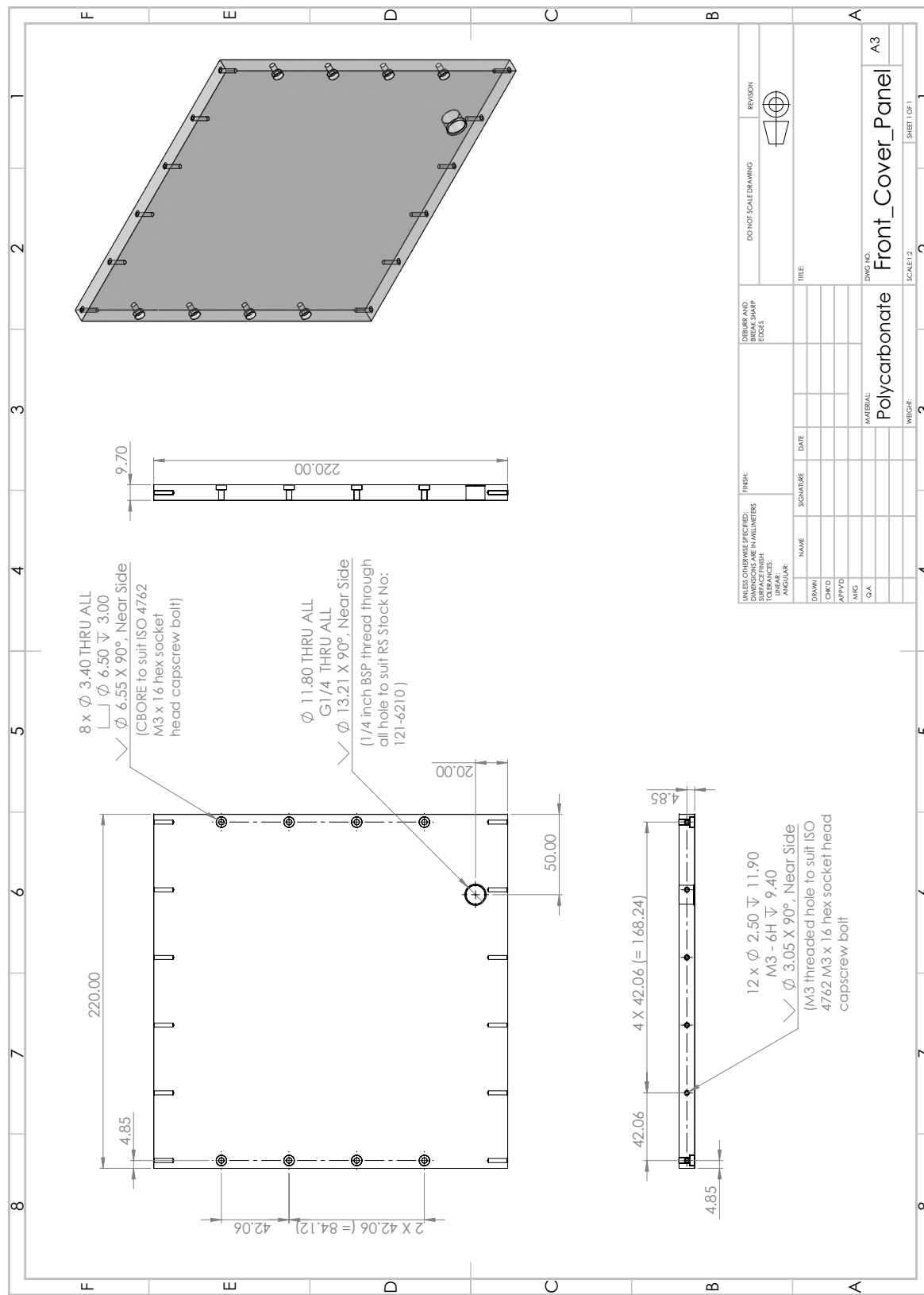


Figure A3.2: Drawing for Front Cover Panel

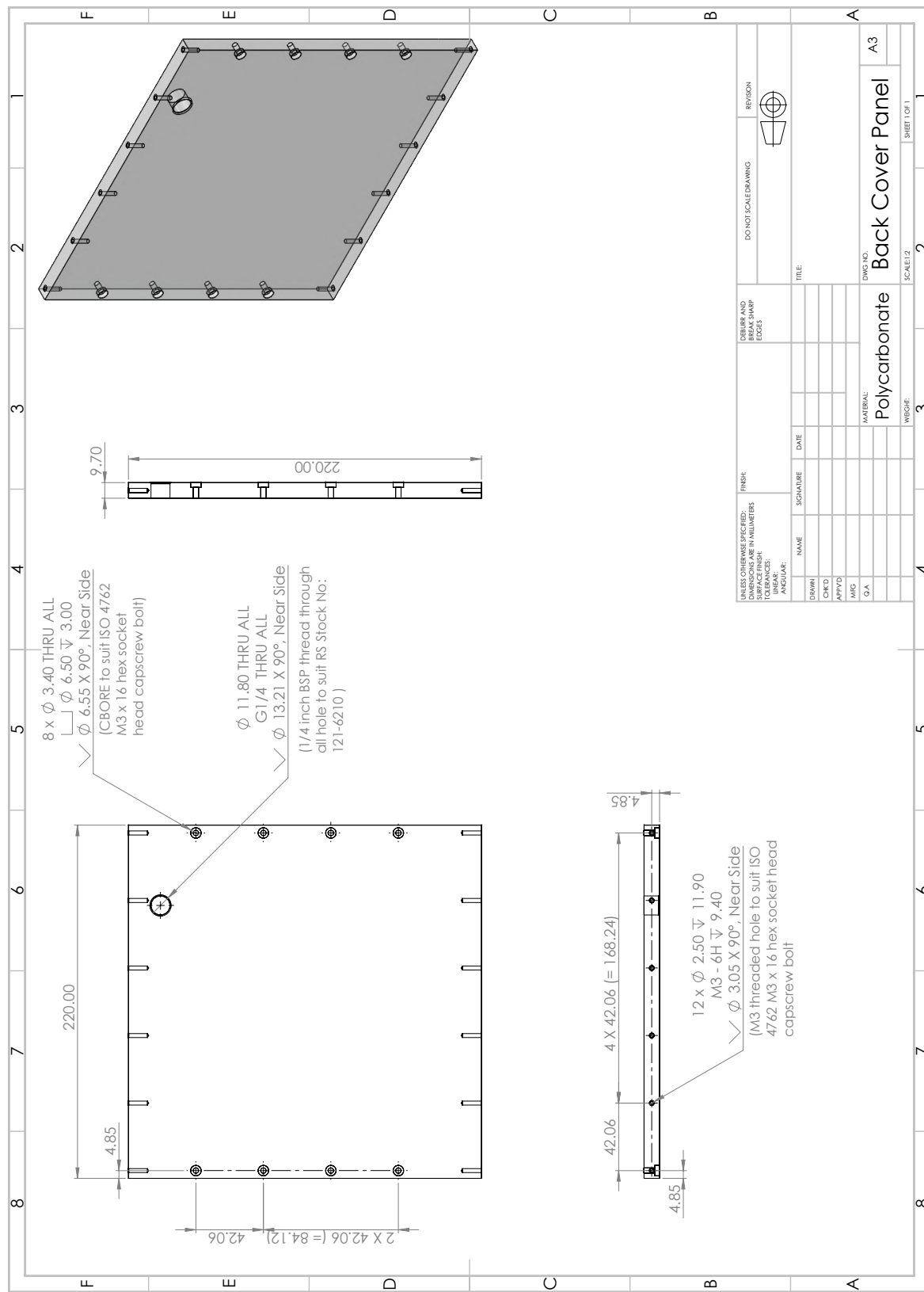


Figure A3.3: Drawing for Back Cover Panel

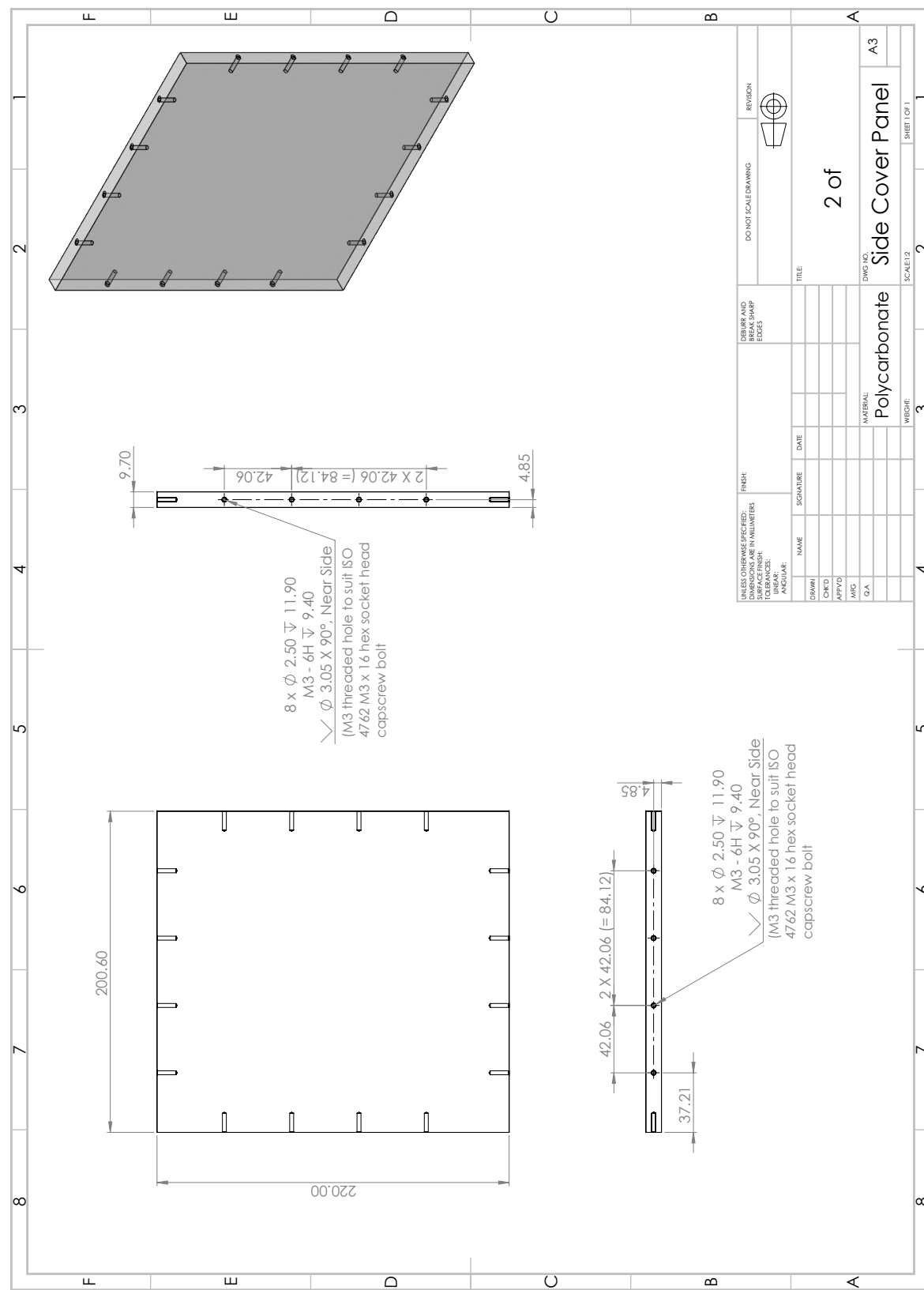


Figure A3.4: Drawing for Side Cover Panel

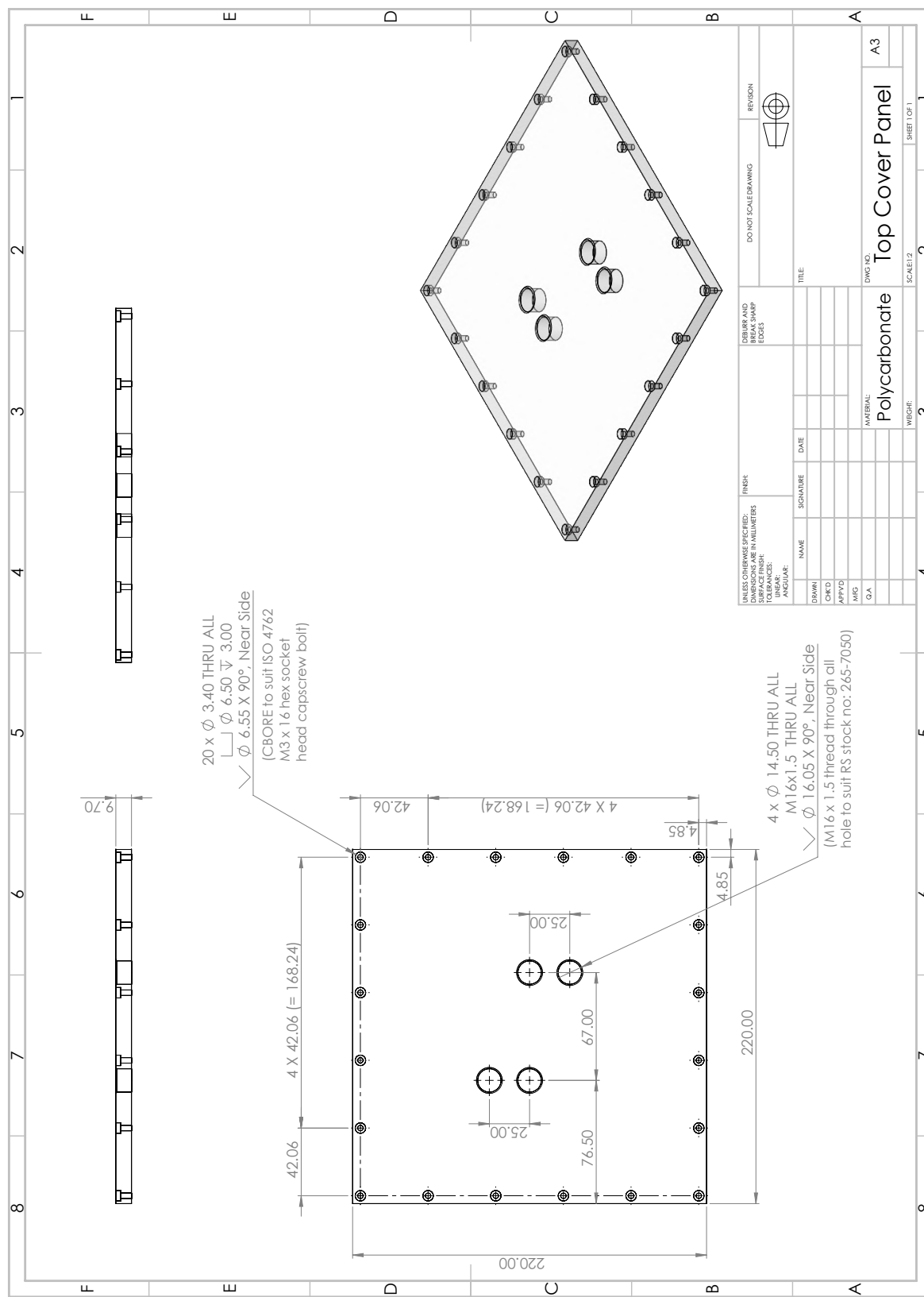


Figure A3.5: Drawing for Top Cover Panel

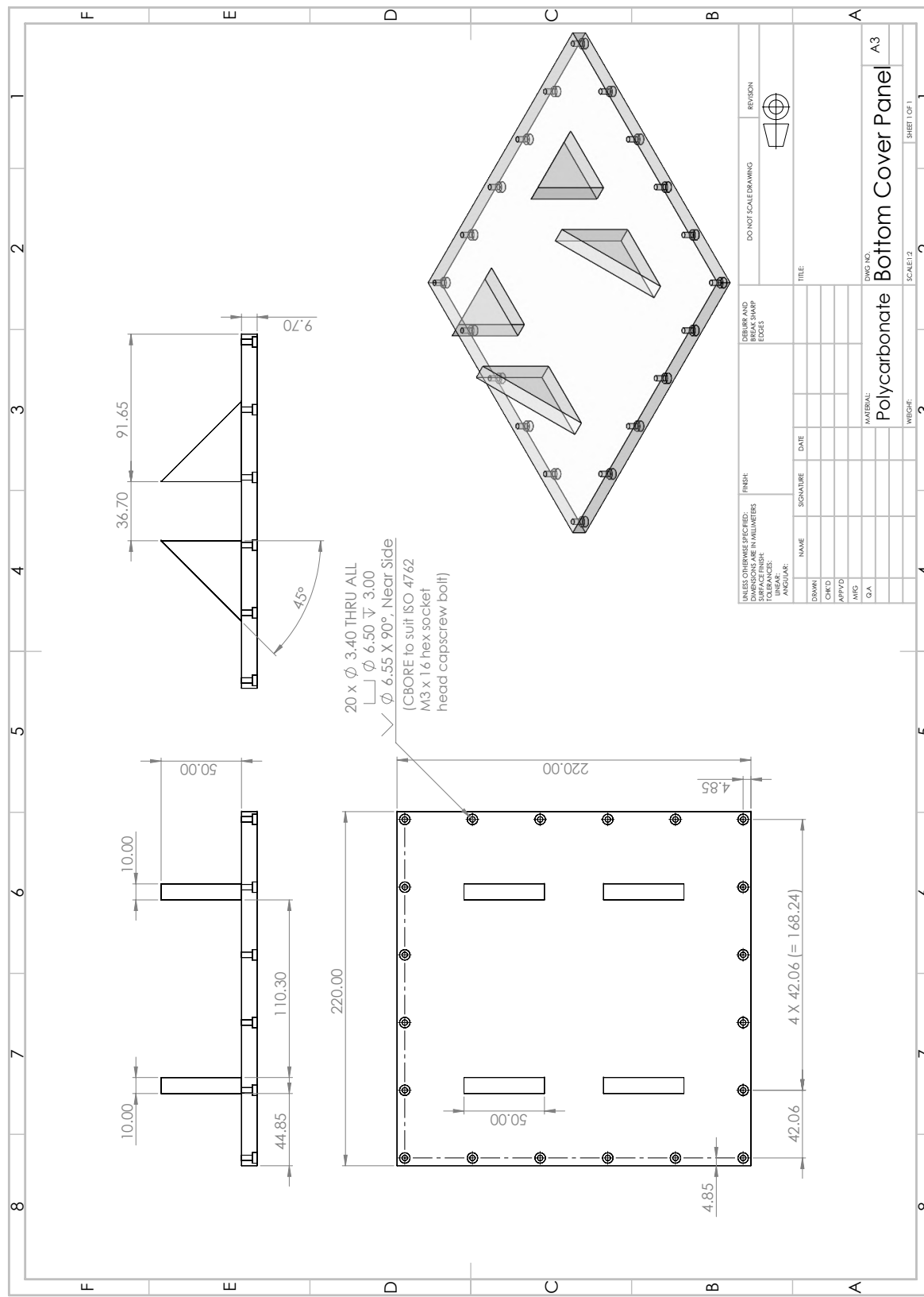


Figure A3.6: Drawing for Bottom Cover Panel

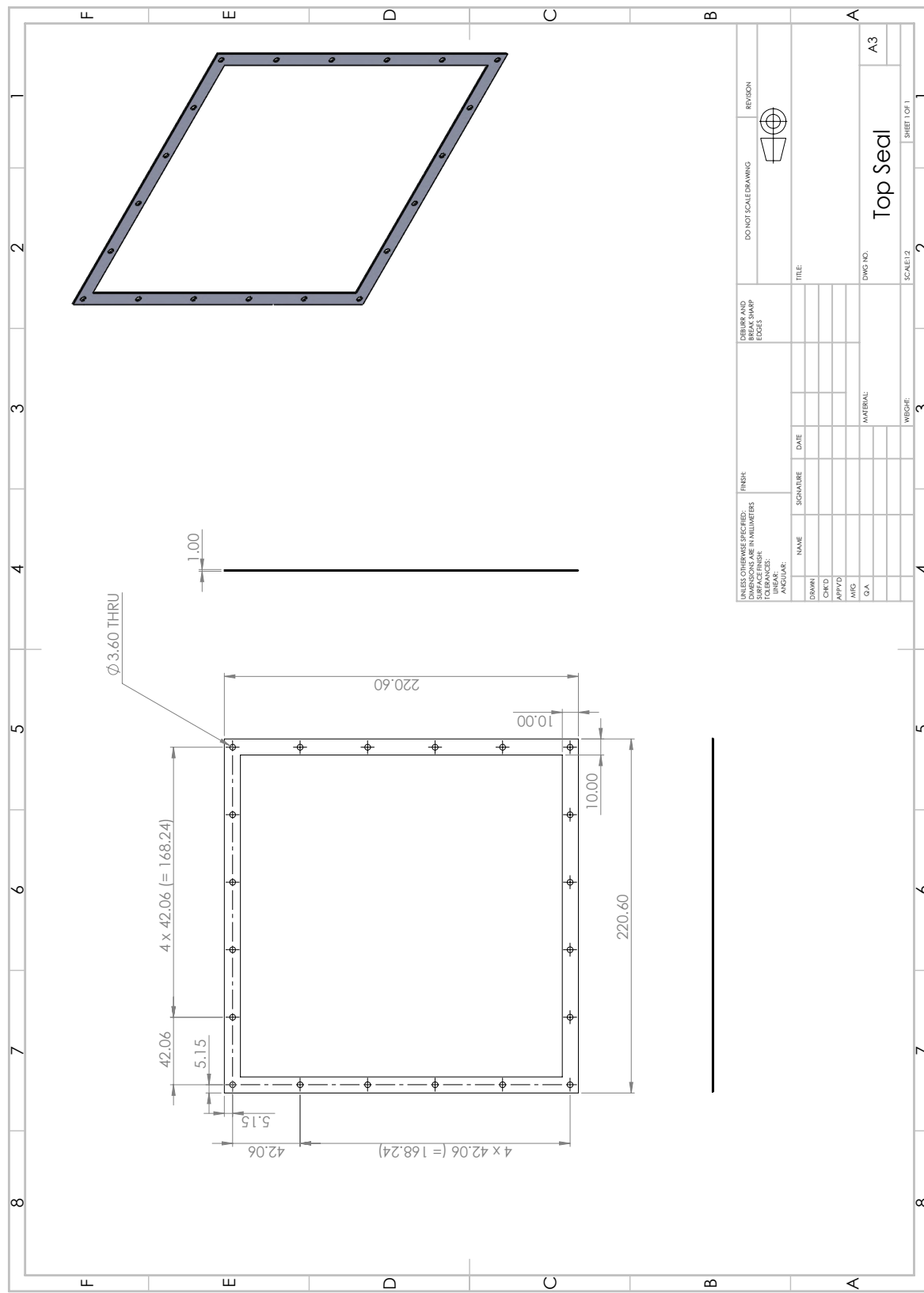


Figure A3.7: Drawing for Seal to be applied